THE UNIVERSITY OF MANITOBA

EXPERIMENTAL STUDY OF EFFECTS OF ROUGHNESS ON A SEPARATION BUBBLE

by

© BRIAN DOELL

A THESIS

SUBMITTED TO THE FACULTY OF

GRADUATE STUDIES IN PARTIAL FULFILLMENT

OF THE REQUIREMENTS FOR THE DEGREE OF

MASTER OF SCIENCE IN ENGINEERING

DEPARTMENT OF MECHANICAL ENGINEERING

WINNIPEG, MANITOBA

April, 1989

National Library of Canada
Bibliothèque nationale du Canada

Canadian Theses Service
Service des thèses canadiennes

Ottawa, Canada
K1A 0N4

The author has granted an irrevocable non-exclusive licence allowing the National Library of Canada to reproduce, loan, distribute or sell copies of his/her thesis by any means and in any form or format, making this thesis available to interested persons.

The author retains ownership of the copyright in his/her thesis. Neither the thesis nor substantial extracts from it may be printed or otherwise reproduced without his/her permission.

L'auteur a accordé une licence irrévocable et non exclusive permettant à la Bibliothèque nationale du Canada de reproduire, prêter, distribuer ou vendre des copies de sa thèse de quelque manière et sous quelque forme que ce soit pour mettre des exemplaires de cette thèse à la disposition des personnes intéressées.

L'auteur conserve la propriété du droit d'auteur qui protège sa thèse. Ni la thèse ni des extraits substantiels de celle-ci ne doivent être imprimés ou autrement reproduits sans son autorisation.

ISBN 0-315-51647-X

Canada

EXPERIMENTAL STUDY OF EFFECTS OF ROUGHNESS ON A SEPARATION BUBBLE

BY

BRIAN DOELL

A thesis submitted to the Faculty of Graduate Studies of the University of Manitoba in partial fulfillment of the requirements of the degree of

MASTER OF SCIENCE

© 1989

Permission has been granted to the LIBRARY OF THE UNIVERSITY OF MANITOBA to lend or sell copies of this thesis, to the NATIONAL LIBRARY OF CANADA to microfilm this thesis and to lend or sell copies of the film, and UNIVERSITY MICROFILMS to publish an abstract of this thesis.

The author reserves other publication rights, and neither the thesis nor extensive extracts from it may be printed or otherwise reproduced without the author's written permission.

ABSTRACT

It was desired to investigate the flow within and behind a two-dimensional laminar separation bubble and observe the effects of increasing the surface roughness ahead of the bubble. To this end, various grades of abrasive were attached to the leading edge of an airfoil with an elliptical nose. Measurements were made of surface pressure, streamwise mean velocity, and turbulence intensity. All tests were performed at a single Reynolds number, namely $Re = 2.4 \times 10^4$ based on the airfoil thickness and freestream velocity. The roughness was gradually made coarser until the separation bubble was eliminated. Increasing the roughness significantly beyond the grade which removed the bubble produced a flow that appeared to be much like that downstream of a backward-facing step. Data connected with the separation bubble was very similar to observations made by other researchers. Specifically, present findings exhibited several characteristics like those found by Bradshaw & Wong (1972) and Chandrsuda & Bradshaw (1981) regarding the reattachment and relaxation of a turbulent boundary layer.

ACKNOWLEDGEMENTS

The author wishes to thank Dr. R.S. Azad for all the guidance and assistance he generously provided in helping me to complete this thesis. The technical aid given by Mr. B. Barrett, Mr. K. Tarte, and Mr. L. Wilkins is also deeply appreciated. The assistance provided by the office staff of Amoco Canada in Fort St. John, B.C. in preparing this thesis is gratefully acknowledged.

Special thanks go to the late Dr. Jeffrey Tinkler who first put the author on the road to a Master's degree and persevered for so long in the construction of the low-speed wind tunnel.

Finally, I wish to thank my parents, Corny and Elma Doell, for all their sacrifice and support.

TABLE OF CONTENTS

Page

LIST OF FIGURES

LIST OF PLATES

LIST OF TABLES

NOMENCLATURE

C	arbitrary constant
C_f	skin friction coefficient $[\tau_w/(^1/_2\rho\overline{U}_r{}^2)]$
C_P	pressure coefficient $[(p - p_r)/(^1/_2\rho\overline{U}_r{}^2)]$
C_{Pmin}	minimum pressure coefficient in separation bubble
$\widetilde{C}_P$	reduced pressure coefficient $[(C_P - C_{Pmin})/(1 - C_{Pmin})]$
H	shape factor (δ^*/θ)
H_S	step height
l_B	length of separation bubble
p	static pressure
p_r	static pressure at reference position ahead airfoil in undisturbed flow
R	reattachment point
Re	Reynolds number based on thickness (tU_r/ν)
S	separation point
t	airfoil thickness
$\overline{U}$	mean velocity
$\overline{U}_r$	mean velocity at reference position ahead of airfoil in undisturbed flow
U_+	non-dimensional velocity $(\overline{U}/u_*)$
$(\overline{u^2})^{1/2}$	root-mean-square fluctuating velocity
$(\overline{u^2})^{1/2}_{max}$	maximum root-mean-square fluctuating velocity
u_*	friction velocity $(\tau_w/\rho)^{1/2}$
x	streamwise distance from nose of leading edge
x_S	streamwise distance from separation point
X^*	normalized distance from reattachment $[(x_S-l_B)/l_B)]$
y	distance from surface

y_+ non-dimensional distance from surface ($u_* y/\nu$)

Greek Symbols

δ^* displacement thickness

θ momentum thickness

ν kinematic viscosity

ρ density

τ_w wall shear stress

1.0 INTRODUCTION

1.1 General

The separation of flow from a surface is a large and complex area of fluid mechanics. The particular phenomenon of the separation bubble arises, as do all flow separations, from the fluid's viscosity and an adverse pressure gradient. When the laminar boundary layer adjacent to the surface meets an adverse pressure gradient, the layer uses up its already reduced momentum against the increasing pressure. The free stream cannot transfer enough momentum to the boundary layer for it to overcome the pressure. Thus, the layer comes to rest at the surface and separates. The adverse pressure gradient causes reverse flow at the surface downstream of the separation. Turbulence develops in the separated flow, which enables momentum transfer to the surface and makes it possible for the flow to reattach. A separation bubble is thus formed that encloses a region of recirculating flow, downstream of which develops a turbulent boundary layer.

Separation bubbles are of practical importance in many flows. One of the major reasons for investigating them is their formation near the leading edge of airfoils. As the airfoil incidence is increased, the bubble can either gradually extend over the airfoil surface or contract and suddenly burst, completely separating flow from the airfoil. This will obviously influence the airfoil's lift and drag characteristics. Separation bubbles also occur in turbomachines, forming on turbine and compressor blades. The energy they remove from the flow reduces efficiency, and the heating they cause is undesirable.

1.2 Review of Other Experiments

Much of the earlier work on leading edge separation bubbles on airfoils has dealt with establishing criteria for differentiating between long and short separation bubbles. The effect of airfoil incidence on bubble development, and the bursting of separation bubbles were also investigated. Excellent summaries of this work have been written by Chang (1970) and Tani (1964).

Tani reviewed a large number of airfoil experiments. Among his conclusions were some observations of the effects of surface roughness or disturbances in the flow. He noted that bubble formation is possible for only a particular range of Reynolds number based on freestream velocity and chord length. Flows with Re below this range can separate but do not reattach. Flows with Re above it undergo transition to turbulent flow ahead of the separation point, and the bubble does not form. This range depends not only on the pressure distribution and surface curvature, but also on the surface roughness and freestream turbulence.

More recent work by Nakamura & Ozono (1987) was done on a flat plate with rectangular leading-edge geometry. One of their main findings was that by increasing the freestream turbulence intensity, the leading edge's separation bubble was correspondingly shortened. The results of the present study indicated that increasing the leading edge surface roughness shortened and altered the separation bubble. A sufficient increase in roughness completely removed the bubble.

The basic structure of the flow in a two-dimensional separation bubble was put forward in a simplified model by Norbury & Crabtree (1955) and later by Crabtree (1957). This model, shown in Fig. 1, follows the fundamental description of a bubble given at the beginning of this section. The diagram shows the streamlines of the flow, and the physical relationship between the separated flow and the recirculation within the bubble.

The separation bubble can usually be found by examining the pressure distribution over the airfoil. The pressure generally remains relatively constant after separation until turbulent mixing commences and permits a rapid pressure recovery. This is illustrated in Fig. 2 in a diagram given by Tani. The sketch shows a constant surface pressure from the beginning of the bubble. This was assumed by Norbury & Crabtree and Tani to extend to the point of maximum bubble thickness. The bubble profile is shown at the bottom of the figure. A rapid pressure recovery takes place over the rest of the bubble. Tani approximated this with a linear recovery for theoretical calculations.

For more detailed pressure distributions, a paper by Castro & Haque (1987) was referred to. Their measurements were conducted within the separated shear layer behind a flat plate normal to an air flow and mounted symmetrically at the leading edge of a splitter plate. In addition to their own data, they gave pressure distributions found by Roshko & Lau (1965) behind a backward step. Pressure data from the present study revealed pressure recovery over the rear of the bubble but failed to show a constant pressure region. These results exhibited similar trends to those reported by Tani and Castro & Haque, but differed quantitatively.

In order to ascertain aspects of the separation bubble flow such as mean velocity and turbulence intensity profiles, two other studies were reviewed. One with a test geometry much like that used in the present study was by Gleyzes, Cousteix, & Bonnet (1984). They performed hot-wire measurements of mean velocity and streamwise turbulence intensity on a two-dimensional airfoil with a leading-edge separation bubble. Another extensive study was that done by Kiya & Sasaki (1983), which was later elaborated on by Kiya (1986). Some turbulence data measured by Kiya & Sasaki were also presented by Castro & Haque (1987). This research was done on a two-dimensional flat plate with a rectangular leading edge. Again, hot-wire measurements were made of the mean velocity and various turbulence quantities through the separation bubble which began at the leading edge. The findings of these two papers showed their flows to be very similar to that in the present experiment.

Concentrating on the reattaching flow at the rear of the bubble and the developing turbulent boundary layer downstream, two papers were referred to. Bradshaw & Wong (1972) re-examined some previous experiments on the flow downstream of steps and fences, and did some new measurements downstream of a backward-facing step. They concluded that the reattaching flow had a shear layer in which the larger eddies either alternated upstream and downstream or were torn in two and moved in both directions. As well, they found that the boundary layer subsequent to reattachment slowly relaxed back to a typical turbulent boundary layer. In a later paper, Chandrsuda & Bradshaw (1981) did further hot-wire measurements immediately behind a backward step. Their data showed rapid changes in turbulence quantities at reattachment, and the same gradual relaxation of the turbulent boundary layer. The present study's results displayed behaviour comparable to that found in these two studies.

Further details from each of the aforementioned papers will be discussed as they relate to present findings in Section 4.0.

1.3 Description of Present Experiment

In the present study interest was centered upon the effects of leading-edge roughness on the subsequent separation bubble development and on the flow structure within and downstream of the bubble. The flow examined was that just beyond the nose of a flat-plate airfoil aligned parallel to the undisturbed flow. This airfoil appeared to produce a leading-edge separation bubble despite the fact it was at zero incidence. Usually at least a small amount of incidence is required to create a bubble. It was speculated that perhaps the airfoil could not be set with sufficient precision to guarantee zero incidence.

Flow visualization was first used to establish the separation bubble's existence and approximate its length. The surface static pressure, and the mean and fluctuating components of the streamwise flow past the airfoil were then measured. Some Pitot tube measurements were also conducted at the surface.

Sets of data were gathered for each configuration of the airfoil. They began with the bare nose and continued through each successive increase in coarseness of the roughness strip attached to the nose. No variations were made in the freestream velocity or the airfoil incidence.

The upcoming sections relate the present experiment and its results. Section 2 describes the experimental equipment and the procedures followed to obtain the results. In Section 3 the raw data is reported and compared to similar research. These results are further analyzed in Section 4, and are discussed in relation to the work of others. Section 5 summarizes the present study and gives its conclusions and recommendations.

2.0 EXPERIMENTAL APPARATUS AND PROCEDURE

2.1 Wind Tunnel

The experiments were conducted in the University of Manitoba's low-speed wind tunnel, which is of the closed circuit return type, as shown in Fig. 3. The tunnel is constructed mainly of wood, with the first diffuser downstream of the lower test section being made of fibreglass. The air is driven through the tunnel by a Woods two-stage, counter-rotating tube-axial fan with a hydraulic drive. Fan speed and hence the air flow rate through the tunnel are controlled by throttling the hydraulic fluid driving the fan motors. The air velocity in the lower test section was previously calibrated against the static pressure drop across the contraction just upstream of the section. The results were given by Maynard & Starko (1982) and Dahl (1987). The more recent calibration was re-checked and found to be still correct. A T.E.M. Engineering Ltd. 513S Micro Projection manometer was used to measure this pressure and thereby monitor the air velocity in the test section. The velocity was maintained at 15 ms^{-1} for all tests.

All tests were performed in the lower test section. The section has a wooden frame with transparent Plexiglas windows along its top and sides. It has a rectangular cross-section, with a height of 53 cm, a width of 76 cm, and an overall length of 183 cm. The section is fitted with corner fillets which taper gradually along the section's length. These have the effect of increasing its cross-sectional area from 0.3742 m^2 at the inlet to 0.3858 m^2 at the outlet. This is to compensate for the growth of the boundary layer along the interior walls of the section.

Hot-wire measurements, which will be described further in upcoming sections, were complicated by the gradual increase in air temperature within the tunnel during its operation. Basically, the constant temperature anemometer circuit uses the probe as one of the arms of a Wheatstone bridge circuit. It tries to keep the hot-wire probe resistance and temperature constant. Heat transfer from the wire to the surrounding air flow will lower the wire's temperature and resistance. To bring the bridge back into balance, the circuit will increase the voltage across the wire and consequently its resistance. Changes in air flow velocity can be calibrated against the resulting voltage changes to provide a measure of the air velocity and its fluctuations. However, the anemometer responds to anything that alters the heat flux from the hot-wire probe, including changes in the ambient air temperature. It has been estimated that a 1°C increase in ambient temperature causes a 1 to 2.5 % decrease in the linearized output voltage [see Lawn (1969), p. 12].

This problem was overcome by keeping the air inside the tunnel at a particular temperature. As the tunnel was operating at a constant speed, the air temperature within it would have to eventually reach equilibrium with the surroundings. It would only be necessary to increase the interior air temperature to this equilibrium temperature. This was accomplished by operating the tunnel at its top speed and monitoring interior temperature with a mercury thermometer fastened to the diffuser at the downstream end of the section. When the interior temperature was 3 to 4°C above room temperature, the tunnel speed was reduced to the 15 ms^{-1} chosen for experimentation. Although the tunnel temperature would eventually begin to increase, it would stay within 1°C of the desired equilibrium temperature for several hours and made it possible to take a great number of reliable measurements.

2.2 Flat-Plate Airfoil

The Plexiglas airfoil on which the measurements were done is shown in Fig. 4. The plate-like airfoil had an overall length of 609 mm, and a thickness of 25 mm. The nose was elliptical, with a minor axis thickness of 25 mm and a semi-major axis length of 23 mm. The tail was tapered towards the airfoil's upper surface. The airfoil was positioned horizontally in the test section, midway between the upper and lower walls. It spanned the section and was fastened to the side windows.

Static pressure measurements along the length and span of the airfoil's upper surface were made possible by thirty static pressure taps that were built into the airfoil. These were used primarily to determine how uniform the flow over the airfoil was. For such measurements, a T.E.M. Engineering Ltd. inclinable multitube manometer was used.

2.3 Roughness Elements

The roughness of the airfoil's nose was varied by fixing a particular grade of abrasive strip to the nose. The grades used were 100-, 80-, 60-, 40-, and 4-grit. These abrasives are shown in Plate 1. The first four are manufactured by 3-M under the brand name "Three-M-ite" and consist of abrasive aluminum oxide particles glued to a fabric backing. The 4-grit consists of silicon carbide particles glued to a paper backing.

These roughness strips were attached to the nose by first placing two strips of 18-mm wide Scotch brand transparent tape side-by-side along the very front of the nose. This created a surface onto which a roughness strip could be glued and which could also be removed later to allow a different grade to be attached. Contact cement was then applied to the tape and the backing of the abrasive which was in the form of a 25-mm wide strip. After centering it on the nose, the abrasive strip was pressed firmly against the tape and the cement allowed to set. In this way, the airfoil roughness was varied.

Quantifying the different grades of roughness proved difficult. Direct measurement of the surface roughness using conventional methods, such as passing a stylus with an electronic pick-up, was not attempted. This was because the abrasive particles might have damaged the stylus. Abrasive manufacturers were also unwilling to provide precise data regarding their product's root-mean-square surface roughness and backing thickness. They consider such information crucial in remaining competitive in their industry. However, they indicated that the grit number used in grading the abrasive refers to the screen mesh size used in separating abrasive materials into their various sizes.

The size of mesh openings and hence the grain size for each grade used in the experiment were found in Machinery's Handbook [see Oberg and Jones (1943), p. 997]. The average protrusion height was taken to be half of this grain size. A number of measurements of the total thickness of each strip were done with a vernier caliper and a mean value taken. These readings are defined in Fig. 5. The difference between this total thickness and half of the grain size was taken as an estimate of the average backing thickness of each roughness.

The exception to this estimation method was the 4-grit roughness. This grade had distinct but apparently random spaces between individual roughness elements. In this case, the mean thickness of the backing and adhesive holding the grains in place was measured along with the total thickness. The difference between these two values was taken as the protrusion height estimate. The grain size indicated by Machinery's Handbook for the 4-grit abrasive seemed incorrect as it significantly exceeded the total thickness actually measured. Thus it was disregarded.

These measurements and estimates are given in Table 1, and the protrusion heights and backing thicknesses are compared in Fig. 6. There appeared to be some variation in the backing thickness, even when experimental scatter and measurement error were taken into account. The 40-grit strip in particular seemed slightly thicker than the other four strips. Ideally, the mean height of the roughness elements should have been flush with the airfoil surface. This thickness should at least have been kept constant to make certain that any variations in the air flow arose from changes in roughness alone.

Aside from this problem, the positioning of the roughness strip was very consistent.

2.4 Flow Visualization Technique

Before beginning the series of tests, it was desired to check whether the flow over the whole airfoil was parallel to the side walls and attached to the airfoil. To help visualize the flow, oil drops were placed on the airfoil surface. The oil used was a mixture of SAE 10W-30 and kerosene with dye added to make it more visible. The mixture had to be balanced to be viscous enough not to spread out in a thin layer that would be hard to observe, and yet not so viscous that it would not respond to the air flow.

After applying the drops, the tunnel was brought up to speed as rapidly as possible. This caused the drops to move in the air flow direction near the surface, leaving streaks behind them. Once it was verified that the flow over the airfoil was attached and parallel, the drops were concentrated near the nose to see whether there was a separation bubble. This process of determining the existence and extent of the leading-edge separation bubble was performed prior to all measurements for a particular roughness.

2.5 Traversing Mechanism

In order to take measurements of the air flow at successive positions along the airfoil's upper surface, a traverse mechanism is built into one of the Plexiglas windows in the top of the section. This traverse made it possible to position various probes both in the streamwise direction and normal to the airfoil surface. It had a positioning precision of ± 0.5 mm in the streamwise direction and ± 0.05 mm in the vertical direction. A static pressure probe, a Pitot tube, and a hot-wire probe were mounted in this traverse for the different measurements required.

2.5.1 Pressure Probes

Since it was found that the static taps were too widely spaced and not near enough to the airfoil nose to provide useful information, a United Sensor static pressure probe was used for all static pressure measurements. Total pressure measurements at the surface were also required to determine shear stress. Therefore, a United Sensor circular Pitot tube was used. Both of these probes are shown in Fig. 7. The pressures found by these probes were measured with a Combist micromanometer, manufactured by Combustion Instruments Ltd., which read to a precision of ± 0.005 mm. The probes' readings compared extremely well with those of a reliable Pitot-static tube. The static probe's readings at the surface were identical to those of the static taps the same distance behind the nose.

For static pressure measurements, the pressure found by the static probe was measured relative to the static pressure at a reference position. This reference point was chosen to be near the test section's centerline and upstream of the airfoil so as not to be disturbed by its presence. To read this pressure difference, the probe was placed at the reference position. A reading was then taken relative to the static tap on the airfoil's centerline and 543 mm behind the nose. All subsequent static and Pitot probe measurements at the airfoil surface were made relative to this same pressure tap.

Positioning of the static and Pitot probes in the streamwise direction was aided by making a light scratch in the airfoil surface 200 mm downstream from the nose. This served as a datum mark which the static probe's taps and the front of the Pitot tube could be aligned. Alignment was accomplished with the help of a vernier microscope set up outside one of the side windows and nearly level with the airfoil surface. The microscope gave a magnified side view of the probe, making more precise positioning of the probe possible. From this mark, the probe was set at successive positions upstream. For setting the probe against the surface, a light source was placed outside the opposite side window. The probe was then lowered until no light was visible between it and its reflection in the airfoil surface. Probe placement was done with the tunnel in operation. This compensated for the slight deflection of the probe caused by the drag force on the probe support normal to the air flow. There was also a small deflection of the top window upon which the traverse rests due to the lower pressure within the tunnel while it was running.

The static and Pitot pressures were used as Preston tube measurements to determine the friction velocity, u_*. Calibrations done by Kassab (1986) on a Pitot tube of the same diameter used in the present study were utilized. It should be noted that the conditions under which the Preston tube may be used accurately demand that the inner region of the boundary layer obey the law of the wall,

$$\overline{U}/u_* = f(u_* y/\nu). \tag{1}$$

It was assumed that the Pitot tube diameter, 1.1 mm, was small enough not to be severely affected by deviations of the inner wall from typical turbulent boundary layer behaviour. To avoid any erroneous readings due to reverse flow, Pitot tube measurements were only taken downstream of reattachment.

Pressure measurements began downstream and proceeded towards the nose. No readings were taken upstream of 22 mm behind the nose. This was because further upstream from this point the elliptical nose begins to measurably slope away from the horizontal. Surface measurements tangent to the surface would have required pitching the probe downward, and the reliability of the static tube in such a disturbed flow is uncertain.

2.5.2 Hot-Wire Probe

Measurements were made of $\overline{U}$ and $(\overline{u^2})^{1/2}$ using hot-wire anemometry. A 55P05 DANTEC boundary layer probe was used with a DANTEC constant temperature anemometer system consisting of a Type 55M01 main unit and a Type 55M10 standard bridge. The linearizer was a DISA Type 55D10 and root-mean-square readings were taken with a DISA Type 55D35 RMS voltmeter which passed its readings on to a Darcy Model no. 440 digital readout. Mean values were initially measured with a DISA Type 55D31 digital voltmeter. When this device began malfunctioning, mean voltages were found by passing the signal through a Linear Systems Ltd. Model no. LS7517 integrator and then reading it with a Fluke

Model no. 8000A digital multimeter. A Hewlett-Packard Model no. 1220A oscilloscope was used to help adjust the bridge's frequency response prior to taking measurements.

The setting of the wire's operating resistance, frequency response, calibration, and linearization was done within the tunnel at the chosen operating temperature described in Section 2.1. The procedure followed can be found in DANTEC manuals [see "Instruction Manual DISA 55M System...", pp. 10-14; and "Instruction...Manual for Type 55D10 Linearizer", pp. 12-19]. It should be noted that an overheat ratio of 0.8 was used to make the hot-wire as sensitive as possible without damaging it [see Lawn (1969), p. 11]. To set the frequency response, the square wave test was conducted at 30 kHz. The resulting anemometer output signal was tuned to give an undershoot of 13 % of its maximum amplitude on the oscilloscope.

The hot-wire could be calibrated in situ for the 10 to 20 ms^{-1} range of velocities. It was put in the same reference position used by the static probe in Section 2.5.1, upstream of the airfoil. Some difficulty was encountered in maintaining test section speeds below 10 ms^{-1}. To calibrate in the 5 to 10 ms^{-1} range, a DISA Type 55A60 calibration unit was used. This apparatus was basically a miniature wind tunnel with a variable speed fan drawing air through a nozzle. The hot-wire was mounted at the nozzle throat and calibrated. Even with this set-up there were fluctuations in the air velocity, and the calibration had to be performed carefully.

On completing the previous steps, the hot-wire was ready for use. The integration time constants for both the RMS voltmeter and the mean voltage reading were set at 30 s. The probe was then positioned in a similar fashion to the static pressure probe. A light source was placed on the opposite side of the tunnel and the probe observed through the microscope. It was lined up horizontally with the 200-mm mark on the airfoil. The probe tip was lowered until it was 0.6 mm from its reflected image in the airfoil. This measurement was achieved using microscope's graticule which had been calibrated against the probe traverse. This meant that the tip was actually 0.3 mm from the surface. This vertical positioning procedure was repeated at every measurement station along the airfoil to ensure correct readings of boundary layer profiles. It was also a precaution against contact between the fragile hot-wire and the surface. All positioning was done with the tunnel operating to compensate for deflections as in the case of the static pressure probe. Measurements ahead of the 22-mm position behind the nose were not used for the same reason given for pressure measurements. Hot-wire readings were taken near the surface with no flow in the tunnel. This was to verify that there was no significant heat transfer to the airfoil in addition to the air flow.

3.0 EXPERIMENTAL MEASUREMENTS

To help clarify the following results and discussion, a sketch of the airfoil's leading edge is given in Fig. 4. It shows the relative positions of the abrasive strip and the separation bubble on the airfoil. It also defines the streamwise dimensions that appear in subsequent sections.

3.1 Static Pressure Distribution

Rough measurements with the static taps in the airfoil indicated that there was a very slight pressure gradient along its length. The static pressure was constant across the span of the airfoil.

Static pressure probe measurements transformed into the pressure coefficient, C_P, are shown in Fig. 8. Measurements showed the pressure recovery over the downstream end of the separation bubble for each of the cases having separation. The existence of the bubble in the bare, 100-, 80-, and 60-grit cases is discussed further in Section 4.0. The curves for the 40- and 4-grit cases show the increase in pressure of the attached flow, which seemed to commence a little further upstream and proceeded slightly more gradually than in the separation bubble.

A phenomenon observed by many researchers but not found in the present study is a constant pressure region over the forward part of the separation bubble. This sort of occurrence is illustrated in Fig. 2. However, it has been noted by Tani (1964) that the presence of a bubble is not necessarily accompanied by a region of relatively constant pressure [see Tani (1964), p. 80]. He concluded this after reviewing a large body of bubble separation material. Furthermore, Gleyzes et al (1984) also had difficulty in some cases locating a constant pressure plateau where one should have existed. They partly attributed this to a deficiency of pressure taps in this region.

The pressure coefficient data is further analyzed in Section 4.1.2.

3.2 Mean Velocity Profiles

The mean velocity profiles found by the hot-wire anemometer are shown in Fig. 9(a-f). They are normalized by the reference velocity, $\overline{U}_r$ = 15 ms^{-1}. Fig. 9(a) compares readings made with the 10 to 20 ms^{-1} calibration and those made with the 5 to 10 ms^{-1} calibration. As can be seen in the figure, the slight difference in resulting profiles were within the anemometer's limits of precision. For this reason, other readings taken with the low-speed calibration have not been included in the presentation of results.

The profiles for the bare, 100-, 80-, and 60-grit leading edges all showed the expected shape and trend. Namely, the upstream profiles in the separation bubble had low velocity regions next to the surface. In fact, for the bare and 100-grit leading edges, some of the measurements closest to the airfoil showed the velocity increasing towards the surface. Measurements taken with no flow in the tunnel indicated negligible heat transfer from the hot-wire to the Plexiglas airfoil. Therefore, this apparent velocity increase was likely the hot-wire's response to the backflow adjacent to the surface in the bubble. That is, this type of probe cannot differentiate between forward and reverse flows and consequently registered an increasing reverse flow as a forward one. As this probe type cannot be accurately calibrated to measure reverse flows, these experimental points have been omitted from all figures and calculations.

The velocity profiles further downstream progressively filled out until they took on the appearance of typical turbulent boundary layers. This pattern of profile development through and downstream of separation bubbles was like those found by Kiya & Sasaki (1983) and Gleyzes et al (1984).

The reattachment point for the flow in each set-up was determined from these profiles. At reattachment the mean velocity profile at the surface should be normal to the surface. However, no measurements were taken closer than 0.3 mm from the airfoil, as explained in Section 2.5.2. Instead, the reattachment point was approximated for the bare and 100-grit cases by choosing it to be the first station downstream of the last one displaying the reverse flow effect. The 80-grit and 60-grit cases had separation bubbles but no apparent reverse flow readings in their profile data. This was likely due to shallowness of the bubble. For these two cases it was decided to approximate reattachment with the first station that definitely showed attached flow. Thus, the first station which had no inflection point in the profile between the free stream and the surface was considered the reattachment point. These positions are recorded in Table 2, and are the values used in all other calculations.

The profile sequence found for the 40-grit leading edge, given in Fig. 9(e), showed what appeared to be turbulent profiles all along the surface with no separation region. This result agreed with other evidence which is reported in Section 4.0.

The arrangement with the 4-grit abrasive gave mean velocity results that differed from the trends observed in the other cases. The data given in Fig. 9(f) showed a boundary layer with a lower velocity region next to the surface. This region filled out over successive stations until it was unnoticable at the station furthest downstream.

Further analysis and interpretation of all mean velocity data and is given in Section 4.1.3.

3.3 Mean Wall Shear Stress

To help verify that the boundary layers were becoming fully developed and turbulent, it was decided to plot the mean velocity profiles in the U_+ versus y_+ form. The friction velocity, u_*, is needed to normalize the data in this way. This quantity can be obtained in several ways.

3.3.1 Cross-Plot Method

One method is to cross-plot the mean velocity profiles. This is described by Azad & Burhanuddin (1983). For the present study, y_+ was chosen to be 90 and used in the logarithmic law,

$$U_+ = (1/0.41)\ln y_+ + C. \tag{2}$$

Three values of U_+ were then calculated using three values of C, namely 5.0, 5.5, and 6.0. The definitions of U_+ and y_+ provided the following equation,

$$U_+ y_+ = \overline{U}y/\nu. \quad (3)$$

Substituting each of the three pairs of values for U_+ and y_+ into this equation gave three plots of $\overline{U}$ versus y. By superimposing these three plots on a velocity profile found with the hot-wire, three intersection points were produced. The velocity components of these points all gave roughly the same value, this being u_*. In this way, u_* was found for the measuring stations downstream of reattachment.

3.3.2 <u>Preston Tube Method</u>

Another method of finding u_* is to use a Preston tube. This approach, first mentioned in Section 2.5.1, determines u_* at a position by measuring the total pressure at that point with a circular Pitot tube resting parallel to and against the surface. The position's static pressure is also measured, usually with a pressure tap in the wall, and the difference between the two pressures calculated. Provided the Pitot tube lies within the flow layer defined by the law of the wall, equation (1), a relationship exists between this pressure difference and u_*. This relationship can be deduced by calibrating the Pitot tube in a circular pipe with fully developed turbulent flow.

Such calibrations were done by Kassab (1986) on a Pitot tube of the same manufacture and dimensions as the one used in the present study. These calibrations were taken to be valid for this experiment.

As previously explained in Section 2.5.1, the assumption was made that the tube was small enough not to be affected significantly by deviations in the inner wall layer from the law of the wall.

3.3.3 Comparison of Results

Before comparing results, it should be emphasized that cross-plotting only works for equilibrium turbulent boundary layers. Such layers follow the logarithmic law. However, several papers on boundary layer relaxation and plots of U_+ versus y_+ using u_* estimates indicated that the boundary layer did not reach equilibrium until farther downstream. This meant that cross-plotted values of u_* immediately behind the reattachment point were likely incorrect.

To determine where this method became valid, the Preston tube approach was used downstream of reattachment. Due to time limitations, measurements were only taken in the bare leading edge set-up. In order to get an estimate of u_* for the other cases and to make comparisons of the two methods, the plot shown in Fig. 10 was made. This figure plots the u_*-values found by the two approaches against the distance downstream from reattachment normalized by that case's bubble length.

Fig. 10 shows the Preston tube values of u_* rapidly increasing after reattachment, reaching a maximum, and then very gradually declining. The Preston tube and cross-plotted u_*-values for the bare case seemed to agree at nearly one bubble-length. The cross-plotted curves for the other cases also appeared to collapse onto the Preston tube measurement at about this point. This comparison can be extended to the plots of U_+ versus y_+ described in Section 4.2.1 and presented in Fig. 11(a-f). Namely, the bare, 100-, 80-, and 60-grit set-ups all obeyed the logarithmic law over a region beyond the bubble. This area overlapped onto the region where the cross-plotted and Preston tube friction velocities agreed. Such agreement would be expected if the flow was in fact fully developed and turbulent.

It was finally decided to use the Preston tube readings of u_* as estimates for the cases having separation bubbles up to one bubble-length past reattachment. For stations further downstream, the cross-plotted u_*-values found for each velocity profile were used. For the 40-grit case, the cross-plotted u_* was used exclusively as the flow was attached over all stations. Since the U_+ versus y_+ profiles for this case all followed the logarithmic law, the use of cross-plotting seemed justified. The 40-grit results are discussed further in Section 4.1.2. The cross-plotted u_* was also used for the entire 4-grit case. While the U_+ versus y_+ plots later showed that there were some deviations from the logarithmic law, these variations fell partly within experimental error.

The values of u_* obtained by the Preston tube were transformed into the skin friction coefficient, C_f. This data is compared to other researchers' results in Section 4.2.4.

3.4 Turbulence Intensity Profiles

The profiles of turbulence intensity normalized by the reference velocity are given in Fig. 12(a-f). In the cases of the bare, 100-, 80-, and 60-grit leading edges, the profile development was similar. Beginning upstream, the profiles showed a maximum about half the boundary layer thickness from the surface. This maximum increased downstream along the separation bubble. In the bare and 100-grit cases it shifted slightly away from the wall. The maximum reached its greatest magnitude near reattachment. Downstream from this point, the intensity next to the surface increased until the profile took on the shape of a typical turbulent boundary layer. Namely, this intensity was low in the free stream, increased through the boundary layer, and approached a maximum near the surface. This profile development was very similar to that shown by Gleyzes et al (1984).

The turbulence profiles for the 40-grit and 4-grit cases, given in Fig. 12(e & f), displayed developmental trends different from those in the other four cases. The 40-grit case appeared to have intensity profiles typical of equilibrium turbulent boundary layers over all the stations. This supported other results that are discussed in Section 4.0.

The intensity profiles for the 4-grit set-up began at the station furthest upstream with a region of high intensity separated from the surface by a lower intensity that increased again towards the surface. At the stations further downstream the high intensity region decreased in magnitude and the turbulence spread slightly away from the surface. However, the profiles did not assume the typical turbulent boundary layer shape until the last downstream station. A possible explanation of the 4-grit case's behaviour is given in Section 4.0.

4.0 ANALYSIS AND DISCUSSION OF RESULTS

In Section 3.0 there has already been some discussion of the basic flow measurements. This section analyzes the data further to reveal more about the separation bubble and the flow downstream of it.

4.1 Existence of Separation Bubble

4.1.1 Flow Visualization

The oil drop patterns at the nose of the airfoil are shown in Plates 2(a-e) for the bare nose and the 100- through 40-grit configurations. As can be seen, the bare nose, 100-, 80-, and 60-grit arrangements each indicated a separated flow region. That is, drops placed near the leading edge moved downstream until they seemed to reach a barrier and form into a ridge normal to the flow direction. This was caused by the separation of the flow from the surface. Drops immediately downstream of this separation either remained stationary or moved upstream. It was surmised that the backward motion was induced by backflow next to the surface, commonly found in separation bubbles. Further downstream, drops again moved downstream, and in some cases a single drop flowed both upstream and downstream. This position was interpretted as being in the vicinity of reattachment. The oil drops behind the 40-grit strip all moved downstream without interuption, showing that the flow was no longer separating.

Measurements were made from the photographs taken of the drop patterns. The positions of separation and reattachment relative to the leading edge were measured and are given in Table 3. As can be observed, the oil drop method of flow visualization did not seem very precise in pinpointing where the surface flow changed, especially in the case of reattachment. The results would probably have been more conclusive had a larger number of visualization trials been performed to provide a more representative sampling. The presence of the drop itself might also have influenced the flow past it, and there could have been interference between adjacent drops. This, along with inconsistencies in drop composition and surface conditions, probably led to the variations reported in Table 3. For this reason, greater credence was given to the mean velocity profiles when it came to fixing the reattachment position. This was described in Section 3.2. Unfortunately the separation region near the leading edge could not be traversed for the velocity profile owing to the elliptical nose, as previously discussed in the experimental procedures. This, and the fact that the oil drops gave fairly consistent results for the separation position, made it possible to fix separation at 18 mm from the leading edge. All four configurations having separation bubbles had this same separation position. Aside from this instance, this flow visualization technique was mainly useful in demonstrating that the separation bubble existed and in roughly estimating its extent.

4.1.2 Reduced Pressure Coefficient Distribution

It was desired to collapse the pressure data given in Fig. 8 and make comparisons with other researchers' work easier. So, the pressure coefficient was renormalized in the manner used by Castro & Haque (1987), namely the reduced pressure coefficient,

$$\tilde{C}_P = (C_P - C_{Pmin})/(1 - C_{Pmin}). \quad (4)$$

C_{Pmin} is the minimum C_P in the separation bubble.

As is shown in Fig. 8, the pressure distributions for the cases having bubble separation did not show constant pressure regions. Therefore the C_{Pmin} used to calculate $\tilde{C}_P$ was the pressure measured at the station furthest upstream. However Roshko & Lau (1965) and Castro & Haque were able to use the minimum pressure in an area of relatively constant pressure. This difference between the raw data of the present study and that of the other two papers might have contributed to later differences in calculated results.

Reduced pressure coefficient curves are shown in Fig. 13. The experimental curves seemed to collapse onto each other fairly well, but also differed from those found by Roshko & Lau (1965) and Castro & Haque (1987). That is, the slopes of the curves leading up to the reattachment of the flow were different, as were the values of C_P they approached. This could have been due to the different experimental geometries used by these researchers. Castro & Haque used a plate normal to the flow fastened to the front of a splitter plate, while Roshko & Lau examined the flow over the backward-facing step formed by various forebodies attached to the front of a plate.

In summarizing the pressure data, it should be emphasized that the presence of the static pressure probe may have had an effect on the flow, and consequently affected the measured pressure. Such interference would have been more detrimental in the region of the separation bubble. The curvature of the leading edge likely also affected the static probe readings. Suggestions are made to improve pressure measurement in Section 5.3.

4.1.3 Effect of Roughness

Using the flow visualization method described in Section 4.1.1 and the mean velocity measurements in Section 3.2, the separation bubble lengths were determined. These lengths are summarized in Table 2. From the table it can be seen that the bubbles produced by the bare leading edge and the 100-grit set-up had lengths slightly longer than those produced by the 80- and 60-grit cases. This agreed with the results of Nakamura & Ozono (1987), who found that increasing the freestream turbulence intensity decreased the separation bubble length on a blunt plate.

The flow in the present study was disturbed by surface roughness rather than an upstream grid across the tunnel as used by Nakamura & Ozono. It was surmised that the disturbances drew energy from the turbulence in the recirculating flow of the bubble. They continued increasing in strength and size until they were able to transfer enough momentum to the airfoil surface to permit reattachment. When the protrusion height of the roughness was increased, correspondingly greater disturbances were introduced to the flow near the surface. This meant there were larger eddies which were moving along the separating and recirculating flow, and rolling up into still larger ones. However, since they were beginning at a larger scale, they required less distance to develop sufficient energy and size to take momentum from the free stream to the surface. So, it was expected that the bubble length would decrease with coarser abrasive strips on the leading edge. Finally, with the 40-grit strip, the transition to turbulent flow further upstream precluded separation altogether.

4.2 Characteristics of Flow Development

4.2.1 Normalized Mean Velocity

The purpose of putting the basic mean velocity data into the normalized profiles of U_+ versus y_+ was to ascertain that the boundary layers were becoming fully developed and turbulent. The values of u_* necessary for this transformation were determined by the process discussed in Section 3.4. The resulting semi-logarithmic plots are shown in Fig. 11(a-f).

The universal law against which all the plots were compared was that proposed by Kader & Yaglom (1978), namely,

$$U_+ = \begin{cases} 14.5\tanh(y_+/14.5), & \text{for } 0 < y_+ < 27.5 \\ 2.44\ln y_+ + 5, & \text{for } y_+ > 27.5 \end{cases} \qquad (5)$$

This law was chosen for its simple mathematical form. Clearly from the plots, the velocity profiles downstream collapsed gradually toward and finally fitted the universal law for the bare, 100-, 80-, and 60-grit cases. For the 40-grit case, the profiles over all the stations fitted the logarithmic law. This verified previous evidence indicating that the flow was attached and that there was an ordinary turbulent boundary layer over the whole region.

4.2.2 Displacement and Momentum Thicknesses

To get more information from the mean velocity data, the displacement thickness, δ^*, momentum thickness, θ, and shape factor, H, were calculated. For the cases having a separation bubble, the calculations were done in two parts. Trapezoidal integration was performed up to the reattachment point, with linear interpolation from the measurement point nearest the surface to the surface. Starting at reattachment, Kader & Yaglom's (1978) universal law was used to extend the mean velocity profile to the experimental points. Thus, the universal law portion of the profile was integrated up to where it intersected the measured points. From there on trapezoidal integration was used as before. The 40-grit case used the universal law and measured data exclusively, while the 4-grit case relied entirely on experimental points with linear interpolation at the surface. Plots of δ^*, θ, and H are shown in Fig. 14(a-c).

Fig. 14(a) shows that in the bare, 100-, 80-, and 60-grit cases, δ^* rose and fell as the measurements moved downstream through the separation bubble. About 10 mm downstream of reattachment, δ^* reached a minimum and then gradually increased. The values of δ^* all seemed to be increasing asymptotically towards a constant, although more measurements taken further downstream to would have made this certain.

The values of O for the bare, 100-, 80-, and 60-grit set-ups increased through the separation bubble, as shown in Fig. 14(b). Following reattachment, θ increased more gradually. It appeared that it was asymptotically approaching a constant value. Again, more readings taken further downstream would have made interpretations more definite.

The plots of H, given in Fig. 14(c), began high in each of the four cases having a separation bubble. It then dropped quickly near reattachment and settled to a constant value of 1.6.

In the case of the 40-grit abrasive on the leading edge, which eliminated the bubble, δ^* and θ both increased over the upstream stations. They gradually approached constant values at x = 60 mm. H maintained a roughly steady value of 1.6 throughout all measurements. An interesting feature of the results for the separation bubble cases and the attached flow of the 40-grit case is that they all appeared to be approaching the same constants for δ^*, θ, and H downstream.

4.2.3 Maximum Turbulence Intensity

The trend displayed by the turbulence intensity profiles, discussed in Section 3.3, had to be made clearer. A plot was made of the maximum turbulence intensity versus the distance from the separation point for the four cases having separation. As can be seen in Fig. 15, this plot shows the magnitude of the maximum intensity increasing along the length of the separation bubble. Interestingly, the bare, 100-, and 80-grit cases reached a maximum magnitude at reattachment. They then declined to a relatively constant level of $(\overline{u^2})^{1/2} = 1.5$ m/s. Furthermore, the bare case attained a reattachment peak which was larger than those for the 100-grit and 80-grit cases. The 60-grit intensity also increased to a maximum near reattachment. However, its maximum magnitude was was close to the final intensity level reached by the other set-ups. After reaching it, the maximum intensity stayed at this level.

This data was re-normalized by $\overline{U}_r^2$ to make comparisons with other researchers' work possible. These plots of $\overline{u^2}/\overline{U}_r^2$ versus distance from separation normalized by the bubble length are given in Fig. 16. Results from Castro & Haque (1987) are also shown. All results exhibited the same trend, namely an increase in the non-dimensionalized normal Reynolds stress from separation to reattachment. Quantitatively, the data from the present study was much lower than that found by Castro & Haque. The peaks of normalized intensity at reattachment were lower for the 100-grit and 80-grit cases, as was noted previously in describing the maximum intensity distribution. The peak was again greatest for the bare leading edge and did not exist at all for the 60-grit case. The normalized intensities in the present study seemed to all move towards a value of $\overline{u^2}_{max}/\overline{U}_r^2 = 0.011$.

4.2.4 <u>Discussion of Results for Flow Development</u>

Some similarities were noticed between the present mean velocity results and the work done by Bradshaw & Wong (1972) and Chandrsuda & Bradshaw (1981) on the reattachment and relaxation of turbulent shear layers.

In the present experiment, the rapid increase in surface shear stress following reattachment that was commented on in Section 3.4.3 was also noted in the two aforementioned papers. Plots of skin friction coefficient, C_f, versus the distance downstream from reattachment normalized by bubble length, X^*, are shown in Fig. 17. The C_f-values for the present study were calculated from the Preston tube readings taken downstream from the bare case's separation bubble. The other two sets of data were measured behind backward-facing steps. Clearly the results differ quantitatively as the backward-step measurements fell fairly close together at a lower value of C_f, while the present results were about twice the magnitude. However, all the studies showed the same rapid rise in C_f immediately following reattachment.

Another point of comparison is that the two papers emphasized that the boundary layer beyond reattachment did not follow the universal logarithmic law. Instead they showed a slight deviation from it between the surface and the freestream which persisted some distance downstream. The present findings, which had reattaching flow and are shown in Fig. 11(a-d), did not have such variations in them. Rather, they began at reattachment by not following the logarithmic law and collapsed toward it gradually over successive stations. In addition, the portion of the profile following the logarithmic law lengthened in a direction away from the surface. This is typical for developing turbulent boundary layers.

Before proceeding with the explanation of relaxation put forward in the aforementioned papers, the displacement and momentum thickness data that complemented the velocity profiles should be discussed. These thicknesses and the shape factor for the reattaching flow are given in Fig. 14(a-c). The apparent tendency of δ^* and Θ toward a constant value after reattachment seemed to correlate well with the velocity profiles if the assumption was made that the boundary layer was developing towards equilibrium. That is, the presence of a fully developed turbulent boundary layer implies that its velocity profile obeys the logarithmic law and that its δ^* and θ are constant. Since both these conditions seemed to be gradually met in the bare, 100-, 80-, and 60-grit cases after reattachment, it appeared that each flow might be approaching equilibrium.

Yet another point to consider is that H was observed to have dropped quickly at reattachment and settled to a constant value of 1.6. Schlichting referred to a paper by J. Persh which gave a value of $H = 1.4$ for the turbulent boundary layer of a flat plate following transition from a laminar layer [see Schlichting (1979), p. 454]. However, Gleyzes et al (1984) also found that after transition to turbulence, H was near 1.6, and they considered it typical for a turbulent boundary layer. They also found the high values of H in the bubble which decreased rapidly at reattachment, as in the present study. Additionally, it was notable that all the cases in the present experiment reached the same final value of $H = 1.6$. This showed that all the set-ups had flows which eventually developed into ordinary boundary layers.

The two papers which Bradshaw collaborated on explained the deviation from the logarithmic law as follows. Bradshaw & Wong (1972) surmised that at reattachment, the shear layer split in two, part of it moving upstream and part continuing downstream. They supposed this bifurcation came about either by the lateral splitting of the flow's larger eddies or by the larger eddies being alternately deflected up and downstream. The region that was previously central in the mixing layer in the bubble was brought into close proximity to the surface. For this reason, the length scale increased swiftly above the equilibrium value moving away from the surface. As the turbulence was not in local equilibrium over the entire inner wall layer, the mean velocity did not completely agree with the logarithmic law. However, as the flow continued downstream this local-equilibrium layer spread slowly outwards from the surface until it assumed the usual thickness in an equilibrium turbulent boundary layer.

The measurements made in the present study were not extensive enough to independently draw as complete a picture of the reattaching flow. Nevertheless, the mean velocity data that was gathered showed a developing turbulent boundary layer. Its equilibrium layer spread from the surface, and the displacement and momentum thicknesses grew asymptotically beyond reattachment. These results certainly fitted the same phenomena described by these authors.

The maximum turbulence intensity data for the bare, 100-, 80-, and 60-grit cases, described in Section 4.2.3 and shown in Fig. 15, could have the following explanation. In the case of the bare leading edge, the eddies in the flow extracted energy from the mean flow, which was shown by the increasing intensity. When the eddies transferred enough energy to the wall layer for reattachment and the shear layer bifurcated, they broke down and the intensity dropped rapidly. The turbulence intensity then moved toward a constant value as equilibrium was established in the relaxing boundary layer. As successively coarser abrasives were placed on the leading edge in the other cases, their roughness elements shed larger eddies. These eddies became closer in size to the freestream eddies and also were in phase with them. This meant the eddies originating from the roughness were better able to extract energy from the freestream eddies and the mean flow. Energy was lost in this interaction due to increased dissipation and the transfer of energy to the other components of turbulence. Hence, the intensity did not reach as high a level as in the bare case. The 60-grit abrasive produced eddies of a large enough size to be most efficient of the four cases in breaking up the larger eddies in the flow and distributing the energy. This was apparent in the absence of a peak in maximum intensity at reattachment. Instead, the maximum turbulence intensity rose gradually to the final level found downstream in the relaxing boundary layer. However, the disturbances added by the 60-grit abrasive were still not sufficient to cause transition to a turbulent boundary layer and completely preclude separation.

A comparison of the present maximum turbulence intensity normalized by $\overline{U}_r^2$ and results found by Castro & Haque (1987) is shown in Fig. 16 and was described in Section 4.2.3. Although the present data and that given in the paper agreed in the overall trend, the data from the present experiment was quantitatively much lower. This could be attributed to the differing geometry of the two experiments used in creating separation bubbles. It was understandable that the much more severe edge of Castro & Haque's backward step arrangement might have induced higher turbulence intensities.

Bradshaw & Wong (1972) and Chandrsuda & Bradshaw (1981) have made thorough measurements of the turbulence of a reattaching flow. They observed a sudden drop in the turbulence intensity and turbulent shear stress at reattaching. Their explanation of this intensity reduction was that near reattachment the flow's large eddies began transferring turbulent energy and shear stress into the inner layer where it was dissipated. The readings taken of the streamwise turbulence intensity in this experiment did not constitute a complete picture of the turbulence structure. Nevertheless, they did show a reduction in its maximum value for $\overline{u^2}$, at least for the bare, 100-, and 80-grit cases. Thus, it could be speculated that the reattachment was proceeding in a manner similar to that described in the two papers mentioned.

It was suspected from the flow visualization stage of testing that the 40-grit case had attached flow over all its stations. The mean velocity and turbulence intensity profiles in Fig. 9(e) and Fig. 12(e) respectively also appeared to be typical of equilibrium turbulent boundary layers. The normalized mean velocity profiles of U_+ versus y_+ in Fig. 11(e) all fitted the logarithmic law. δ^* and θ, shown in Fig. 14(a & b), both increased over the upstream measurement stations and gradually approached constant values at x = 60 mm. H maintained a roughly steady value of 1.6 throughout all readings. All these observations indicated that the 40-grit abrasive was sufficiently coarse to cause transition, make the boundary layer turbulent, and eliminate separation.

4.3 Flow Downstream of 4-Grit Strip

The profiles of mean velocity and turbulence intensity for the 4-grit arrangement are given in Fig. 9(f) and Fig. 12(f), respectively. They were previously described in Section 3.0. Semi-logarithmic plots of U_+ versus y_+ for this set-up using cross-plotted u_*, shown in Fig. 11(f), indicated that only for the last four profiles downstream did the profiles have linear portions that followed the logarithmic law.

It was anticipated that the velocity profiles following the relatively high protrusions of the 4-grit abrasive might exhibit development like that behind a backward-facing step. Measurements done by Etheridge & Kemp (1978) behind a backward step were chosen for comparison. One difficulty in making such a comparison was the range of profiles displayed in Etheridge & Kemp's paper. Their mean velocity profiles ended 4.0 step-heights behind the step. The 4-grit case readings only began at 7.29 step-heights, taking the step height to be 2.21 mm from Table 1. Nevertheless, Etheridge & Kemp's profile at 4.0 step-heights showed little if any inflection in the boundary layer, and no layer of near-uniform velocity, while the 4-grit case profiles did. However, it could not be predicted how their flow would develop further downstream. It was also speculated that the extreme size of the abrasive's protrusions were severely disturbing the flow, which might also have made comparison difficult.

Continuing the comparison, Etheridge & Kemp's turbulence intensity measurements were examined. Unlike their mean velocity data, they presented all of their turbulence intensity profiles. These extended as far as 8.26 step-heights from their step. This resulted in some overlap of their data on the present readings. The streamwise turbulence intensities compared well. The intensity is a finer quantity than the mean velocity just discussed. So, it appeared that the flow in the 4-grit case was somewhat like that behind a backward-facing step. This may have been because the 4-grit case was making a step 2.21 mm high near the airfoil nose.

5.0 CONCLUSIONS AND RECOMMENDATIONS

5.1 Summary

Reviewing the study's results, it was found that by increasing the coarseness of abrasive strips on the leading edge of an airfoil with a leading-edge separation bubble, the bubble could be slightly shortened and ultimately eliminated. By increasing the roughness significantly beyond this point, a flow like that downstream of a backward-facing step appeared. This may have occurred due to the step-like characteristics of the roughness strip rather than the scale of roughness.

The separation bubble produced by the present plate-like airfoil was discovered to have a structure resembling those generated by a range of geometries. These set-ups included an ONERA LC 100 D airfoil, uased by Gleyzes et al (1984); a flat plate with a rectangular leading edge, used by Kiya & Sasaki (1983) and Nakamura & Ozono (1987); a flat plate with a forebody followed by a backward-facing step, used by Roshko & Lau (1965); and a splitter plate with a flat plate normal to the flow attached to its leading edge, used by Castro & Haque (1987). Further, the flow produced by the 4-grit case bore a resemblance to the reattaching flow behind a backward-facing step, the set-up used by Etheridge & Kemp (1978).

Finally, the reattachment and relaxation of the boundary layer were investigated and gave results that were similar to the findings of Bradshaw & Wong (1972) and Chandrsuda & Bradshaw (1981).

5.2 Conclusions

This experiment showed that:

1) The introduction of disturbances to the flow by increasing surface roughness was able to alter the leading edge separation bubble and finally remove it altogether.

2) The structure of the separation bubble was similar to bubbles found on other types of leading edges, and to bubbles formed behind backward-facing steps.

3) The flow behind reattachment displayed some of the aspects of a flow relaxing to a turbulent boundary layer in equilibrium as described by Bradshaw & Wong (1972) and Chandrsuda & Bradshaw (1981).

5.3 Recommendations

To continue the research begun in this study, several recommendations are made.

1) Some provision should be made for flush-mounting abrasive strips to preclude possible interference from the backing, and more precise measurements made of the abrasive's surface roughness.

2) Static pressure taps should be incorporated in the airfoil leading edge at close intervals to determine pressure distributions more accurately.

3) Accurate measurements in the backflow region of the separation bubble are required for a more complete understanding of the flow structure.

4) Measurements of the friction velocity should be made for each

test configuration.

5) More extensive turbulence data would make the turbulence structure clearer. The shallowness of the separation bubble might make this difficult.

6) Data taken further downstream and, if possible, nearer the airfoil surface would also give a more complete picture of the flow.

6.0 REFERENCES

Azad, R.S. 1983. Corrections to measurements by hot-wire anemometer in proximity of a wall. University of Manitoba, Dept. of Mechanical Engineering, Rept. MET-7.

Azad, R.S., and S. Burhanuddin. 1983. Measurements of some features of turbulence in wall-proximity. Exper. in Fluids 1: 149-160.

Bradshaw, P., and F.Y.F. Wong. 1972. The reattachment and relaxation of a turbulent shear layer. Jour. of Fluid Mech. 52: 113-135.

Castro, I.P., and A. Haque. 1987. The structure of a turbulent shear layer bounding a separation region. Jour. of Fluid Mech. 179: 439-468.

Cebeci, T., A.K. Khattab, and K. Stewartson. 1980. On nose separation. Jour. of Fluid Mech. 97: 435-454.

Chandrsuda, C., and P. Bradshaw. 1981. Turbulence of a reattaching mixing layer. Jour. of Fluid Mech. 110: 171-194.

Chang, P.K. 1970. Separation of flow. International series of monographs in interdisciplinary and advanced topics in science and engineering. Vol. 3. Oxford: Pergamon Press.

Crabtree, L.F. 1957. Effects of leading-edge separation on thin wings in two-dimensional incompressible flow. Jour. of Aero. Sci. 24: 597-604.

Dahl, H. 1987. Calibration of a wind tunnel test section for a boundary layer/wake mixing experiment. B.Sc. thesis, University of Manitoba.

Etheridge, D.W., and P.H. Kemp. 1978. Measurements of turbulent flow downstream of a rearward-facing step. Jour. of Fluid Mech. 86: 545-566.

Gleyzes, C., J. Cousteix, and J.L. Bonnet. 1984. Laminar separation bubble with transition-prediction test with local interaction. Rolls-Royce Ltd. Rept. No. PNR-90231. Translated in: N.A.S.A. N85-18008.

Hinze, J.O. 1959. Turbulence. New York: McGraw-Hill.

Instruction manual DISA 55M system with 55M10 CTA standard bridge. DISA Elektronik A/S.

Instruction and service manual for type 55D10 linearizer. DISA Elektronik A/S.

Kader, B.A., and A.M. Yaglom. 1978. Similarity treatment of moving-equilibrium turbulent boundary layers in adverse pressure gradients. Jour. of Fluid Mech. 89: 305-342.

Kassab, S.Z. 1986. Turbulence structure in axisymmetric wall-bounded shear flow. Ph.D. thesis, University of Manitoba.

Kiya, M. 1987. Structure of flow in leading-edge separation bubbles. In: Boundary-layer separation: Proc. of I.U.T.A.M. symposium, London, Aug. 26-28, 1986. New York: Springer-Verlag.

Kiya, M., and K. Sasaki. 1983. Structure of a turbulent separation bubble. Jour. of Fluid Mech. 137: 83-113.

Lawn, C.J. 1969. Turbulence measurements with hot wires at B.N.L. Central Electricity Generating Board, Berkeley Nuclear Laboratories, Rept. RD/B/M 1277.

Maskell, E.C. 1965. A theory of the blockage effects on bluff bodies and stalled wings in a closed wind tunnel. A.R.C. Reports and Memoranda No. 3400.

Maynard, I., and K. Starko. 1982. Calibration of the University of Manitoba's low speed wind tunnel. B.Sc. thesis, University of Manitoba.

Meyer, R.F. 1966. A note on a technique of surface flow visualization. N.R.C. Rept. LR-457.

Nakamura, Y., and S. Ozono. 1987. The effects of turbulence on a separated and reattaching flow. Jour. of Fluid Mech. 178: 477-490.

Norbury, J.F., and L.F. Crabtree. 1955. A simplified model of the incompressible flow past two-dimensional aerofoils. R.A.E. Tech. Note No. AERO.2352.

Oberg, E., and F.D. Jones. 1943. Machinery's handbook. 12th ed. New York: Industrial Press.

Patel, V.C. 1965. Calibration of the Preston tube and limitations on its use in pressure gradients. Jour. of Fluid Mech. 23: 185-208.

Persh, J. 1956. A study of boundary-layer transition from laminar to turbulent flow. U.S. Naval Ordnance Lab. Rept. 4339.

Raudkivi, A.J., and R.A. Callander. 1975. Advanced fluid mechanics. London: Edward Arnold.

Roshko, A., and J.C. Lau. 1965. Some observations on transition and reattachment of a free shear layer in incompressible flow. In: Proc. of the 1965 Heat Trans. and Fluid Mech. Inst.

Schlichting, H. 1979. Boundary-layer theory. 7th ed. New York: McGraw-Hill.

Tani, I. 1964. Low-speed flows involving bubble separations. In: Progress in aeronautical sciences. Vol. 5 (ed. by D. Kuchemann and L.H.G. Sterne). Oxford: Pergamon Press.

Van Driest, E.R. 1956. On turbulent flow near a wall. Jour. of the Aero. Sci.: 1007-1011, 1036.

Werle, M.J. 1983. Compressor and turbine blade boundary layer separation. In: Viscous effects in turbomachines. AGARD Conf. Proc. No. 351.

7.0 TABLES

Table 1: Roughness Dimensions

(all dimensions in mm)

Grade	Grain Size	Protrusion Height	Backing Thickness	Total Height
100-Grit	0.149	0.075	0.58	0.65
80-Grit	0.177	0.089	0.88	0.97
60-Grit	0.250	0.125	0.71	0.83
40-Grit	0.420	0.210	1.17	1.38
4-Grit	4.76*	1.46	0.75	2.21

* Not used in calculations.

Table 2: Separation Bubble Dimensions Derived from Velocity Profiles

(all dimensions in mm)

Configuration	Separation Point	Reattachment Point	Bubble Length
Bare	18	42	24
100-Grit	18	44	26
80-Grit	18	36	18
60-Grit	18	38	20

Table 3: Separation Bubble Dimensions

Derived from Flow Visualization

(all dimensions in mm)

Configuration	Separation Point	Reattachment Point
Bare	16	27 - 37
100-Grit	18	37 - 43
80-Grit	17 - 18	37 - 38
60-Grit	18	37

8.0 PLATES

Plate 1:

Comparison of Grades of Abrasive

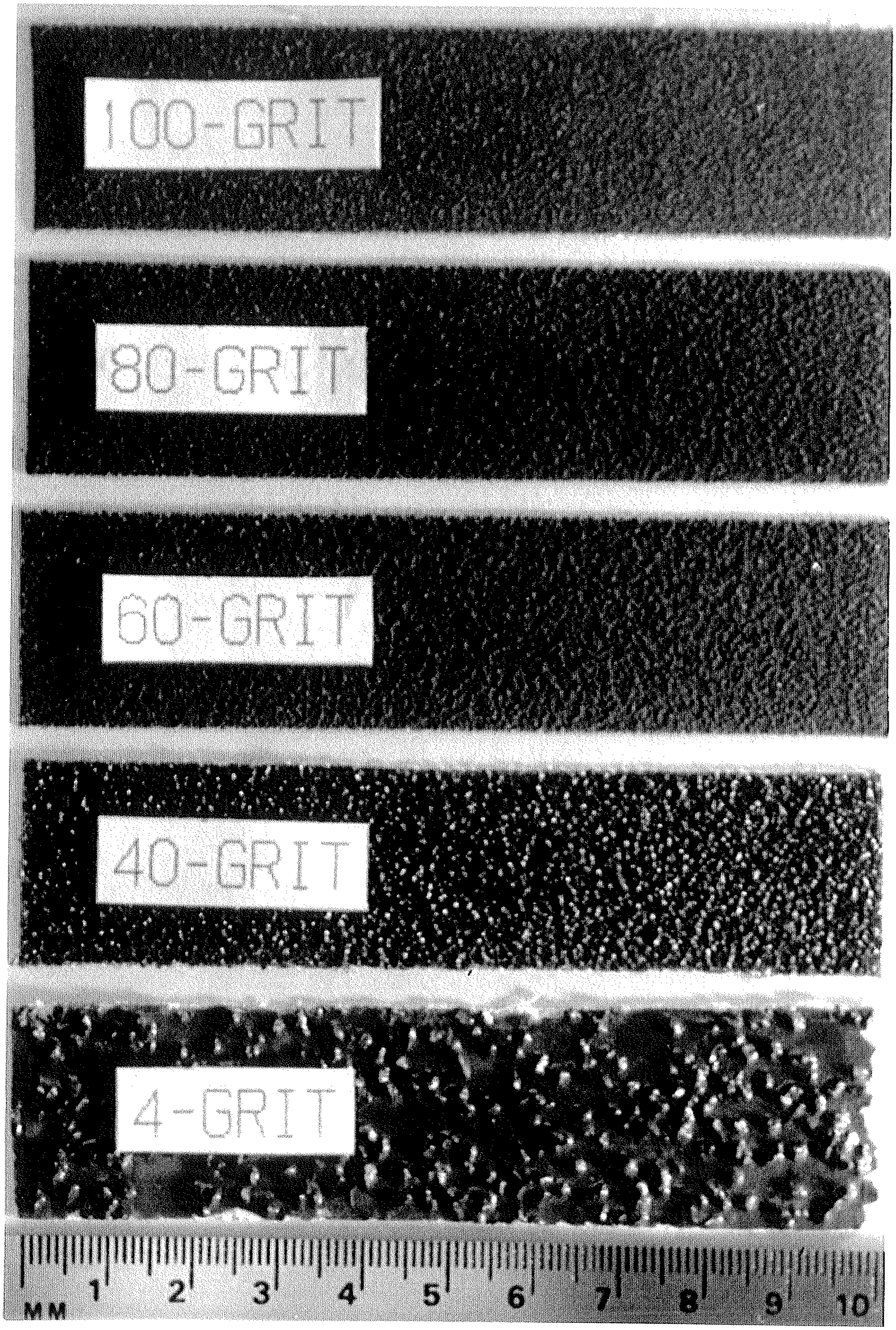
100-GRIT
80-GRIT
60-GRIT
40-GRIT
4-GRIT
MM 1 2 3 4 5 6 7 8 9 10

Plate 2:

Flow Visualization Results

(a) Bare

(b) 100-Grit Separation

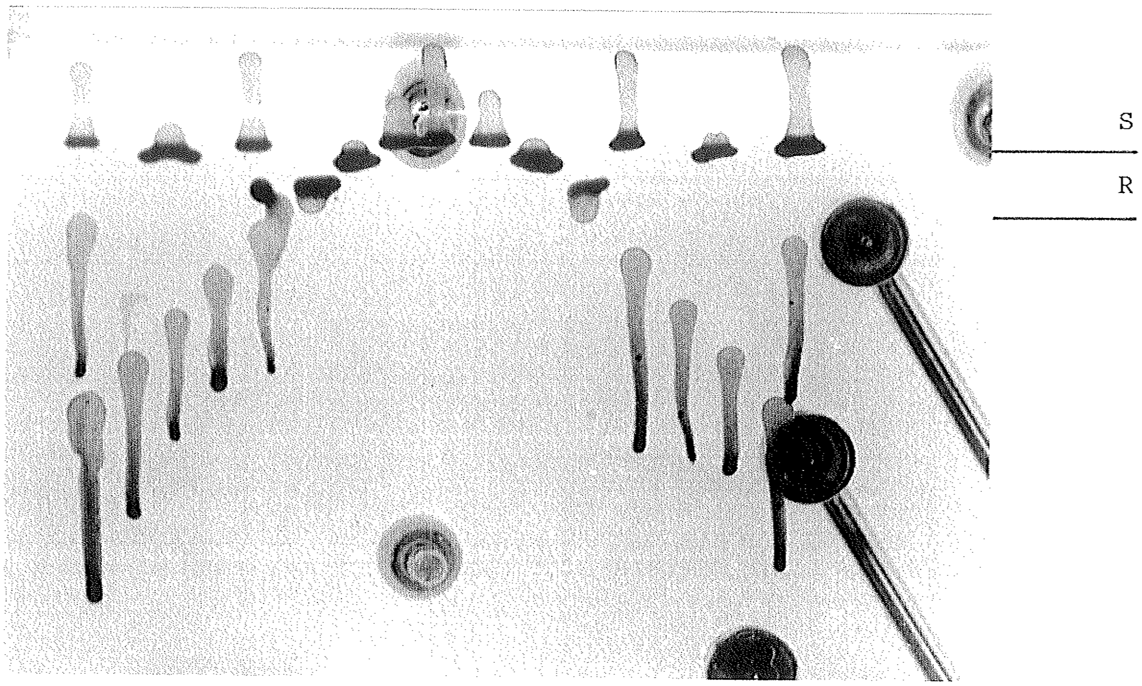
S
R

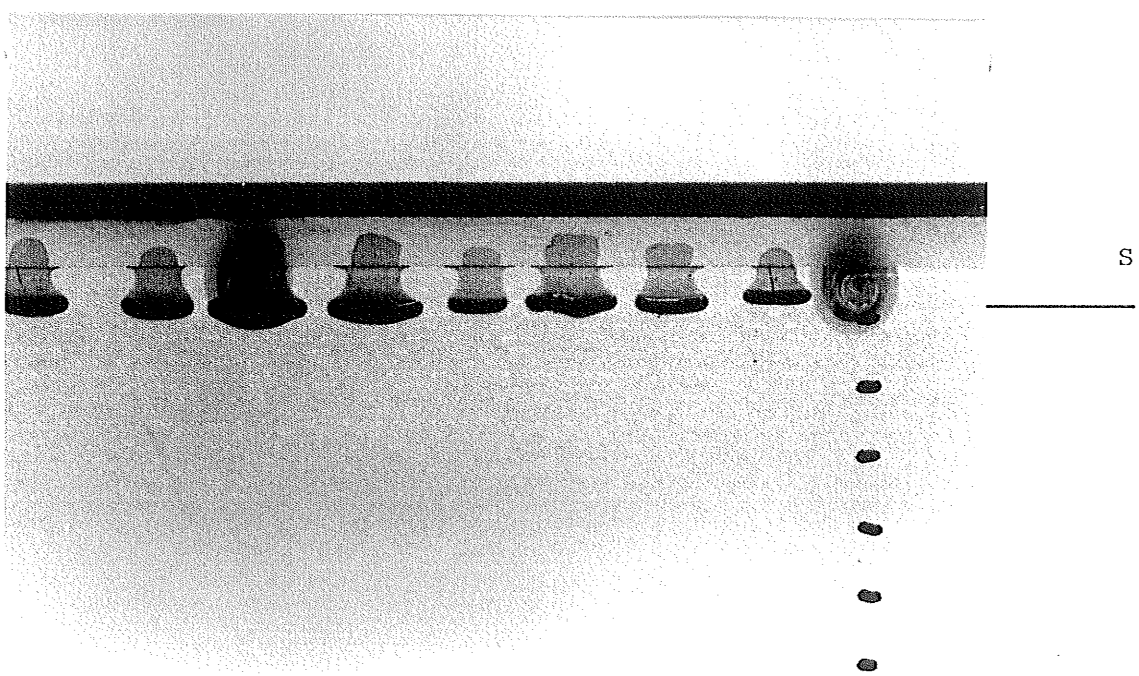
S

(c) 100-Grit Reattachment

(d) 80-Grit

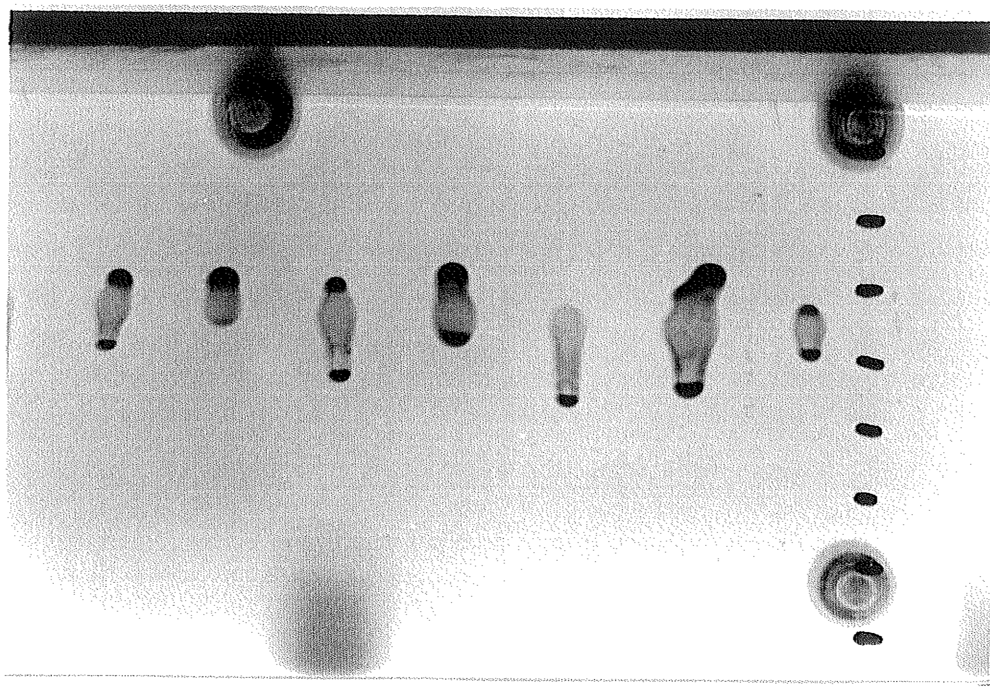

R

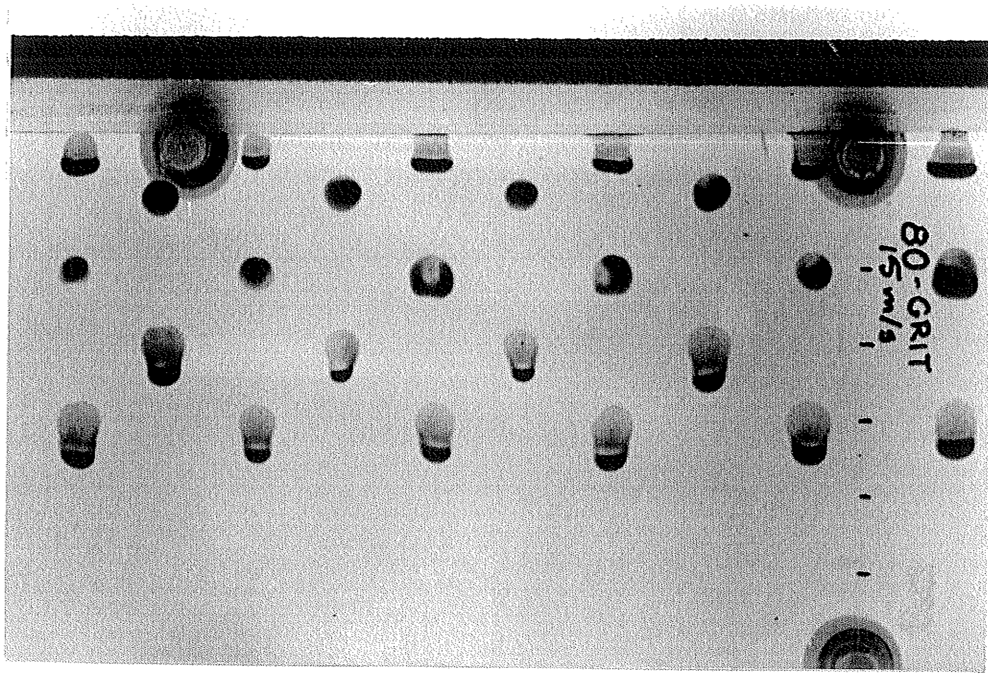

S

R

(e) 60-Grit

(f) 40-Grit

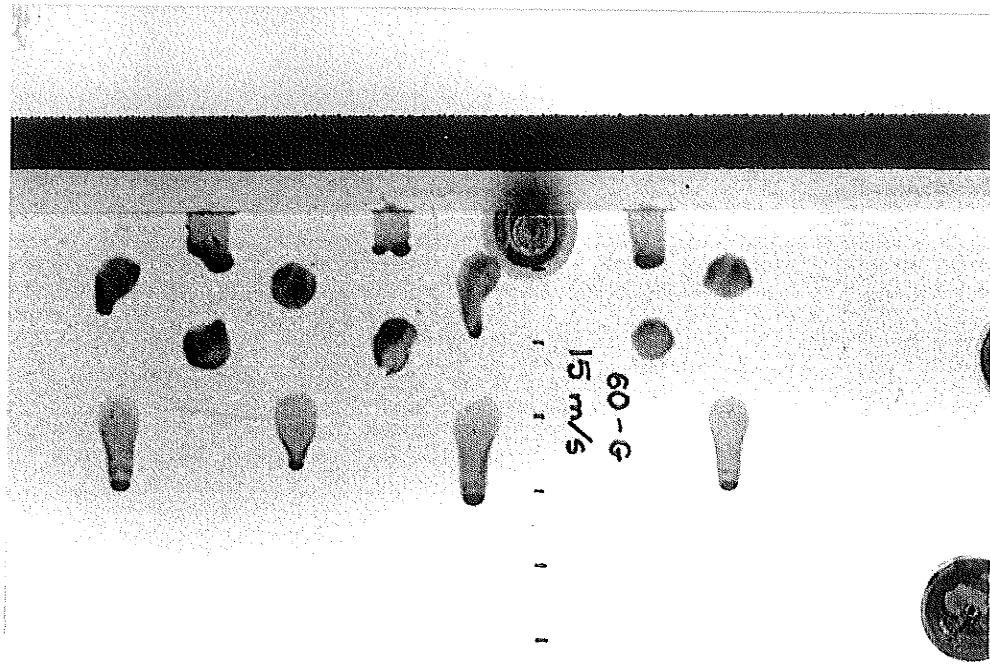

S

R

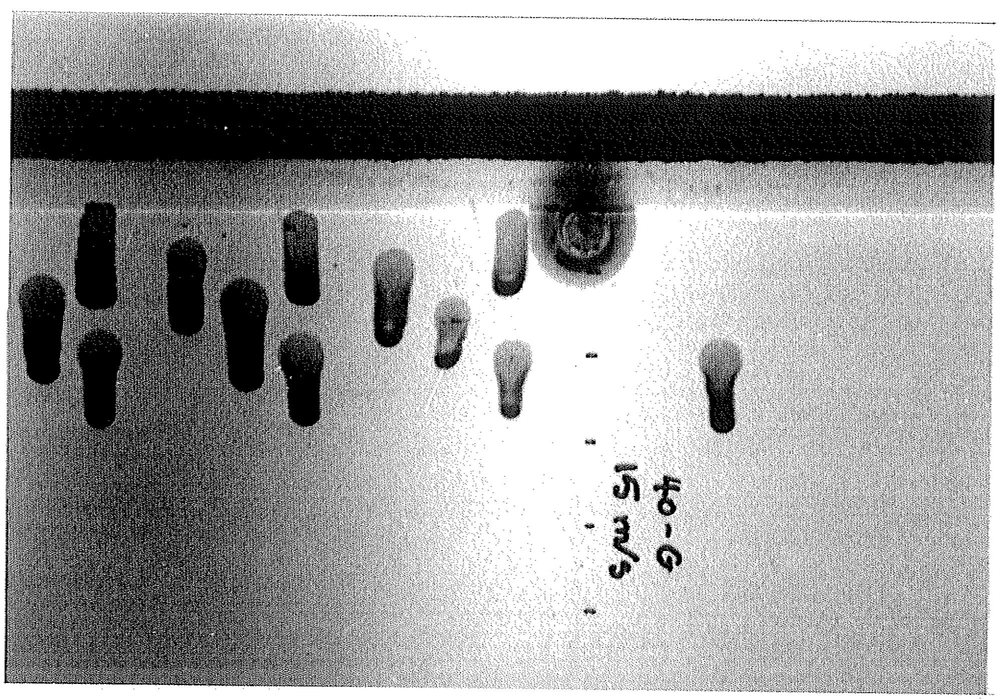

9.0 FIGURES

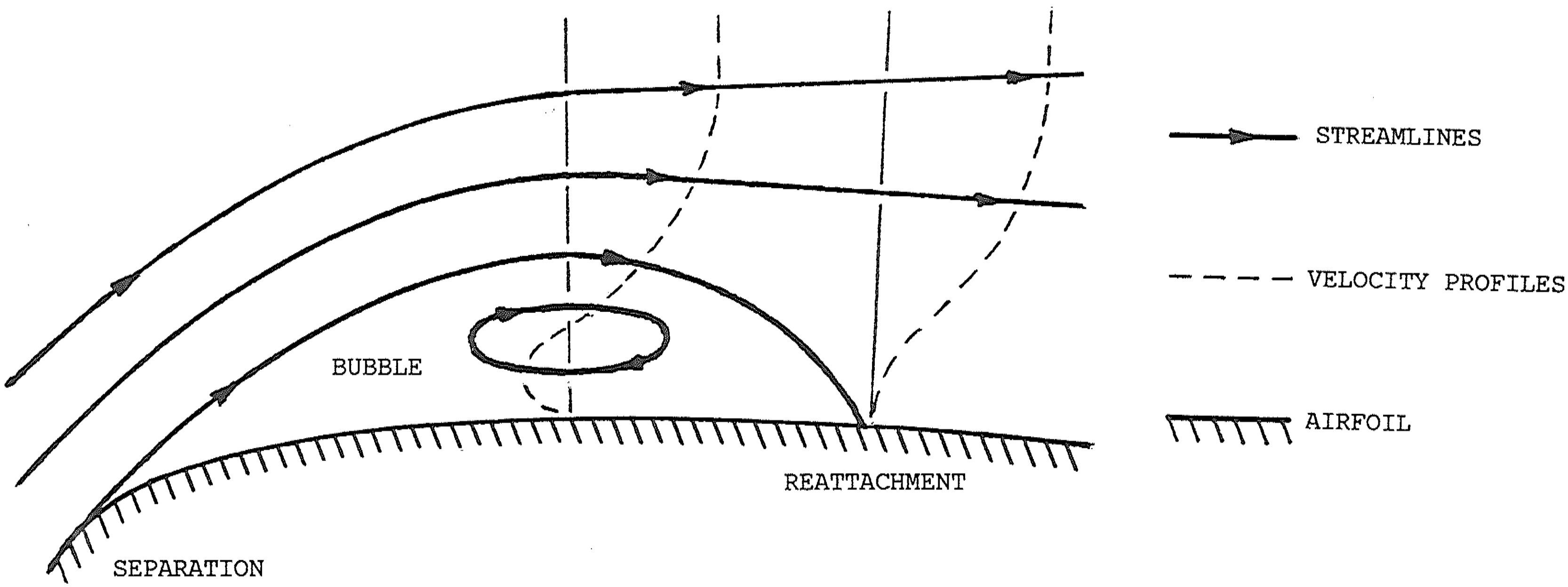

Figure 1: Norbury & Crabtree's Separation Bubble Model.

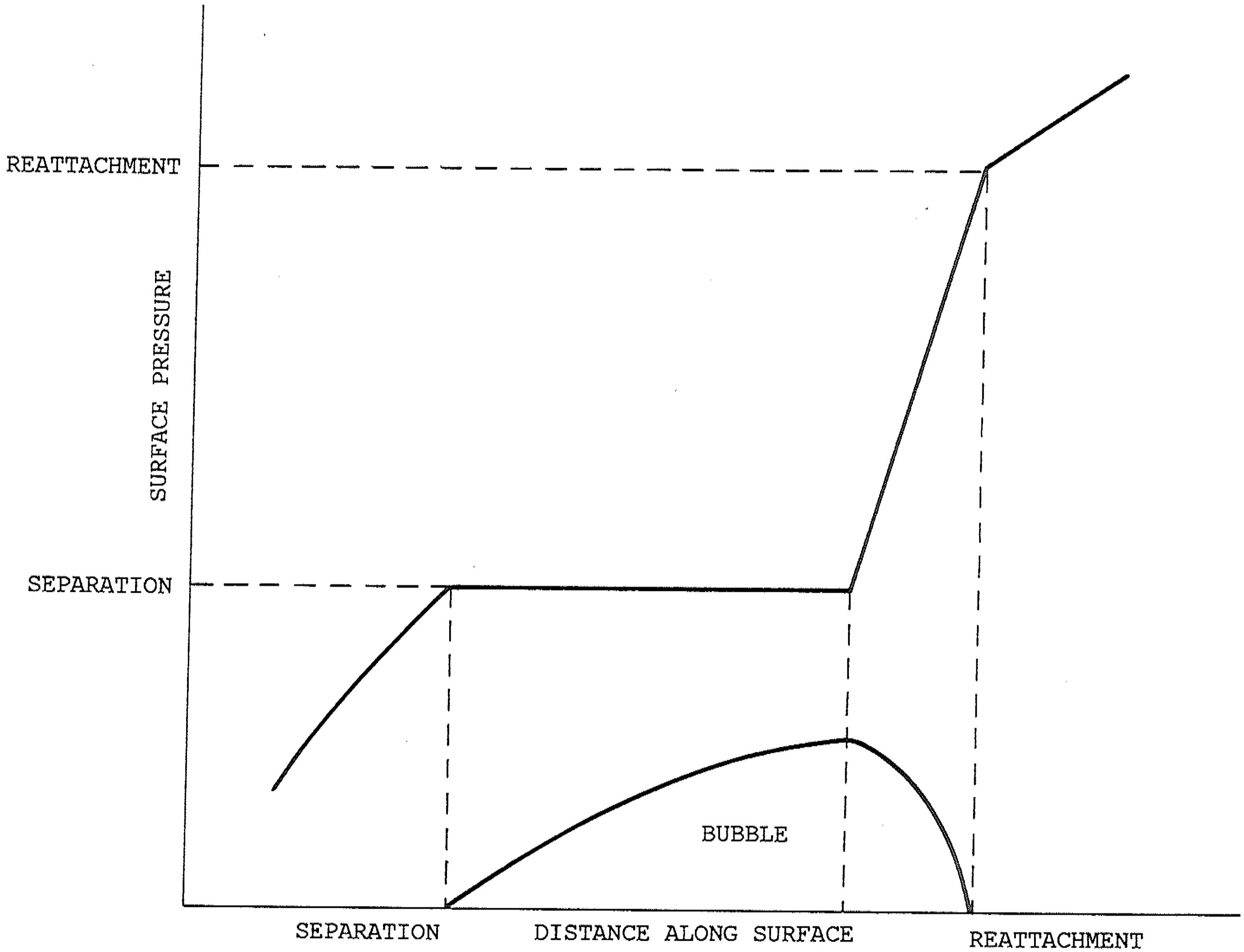

Figure 2: Pressure Recovery over Separation Bubble

[see Tani (1964)].

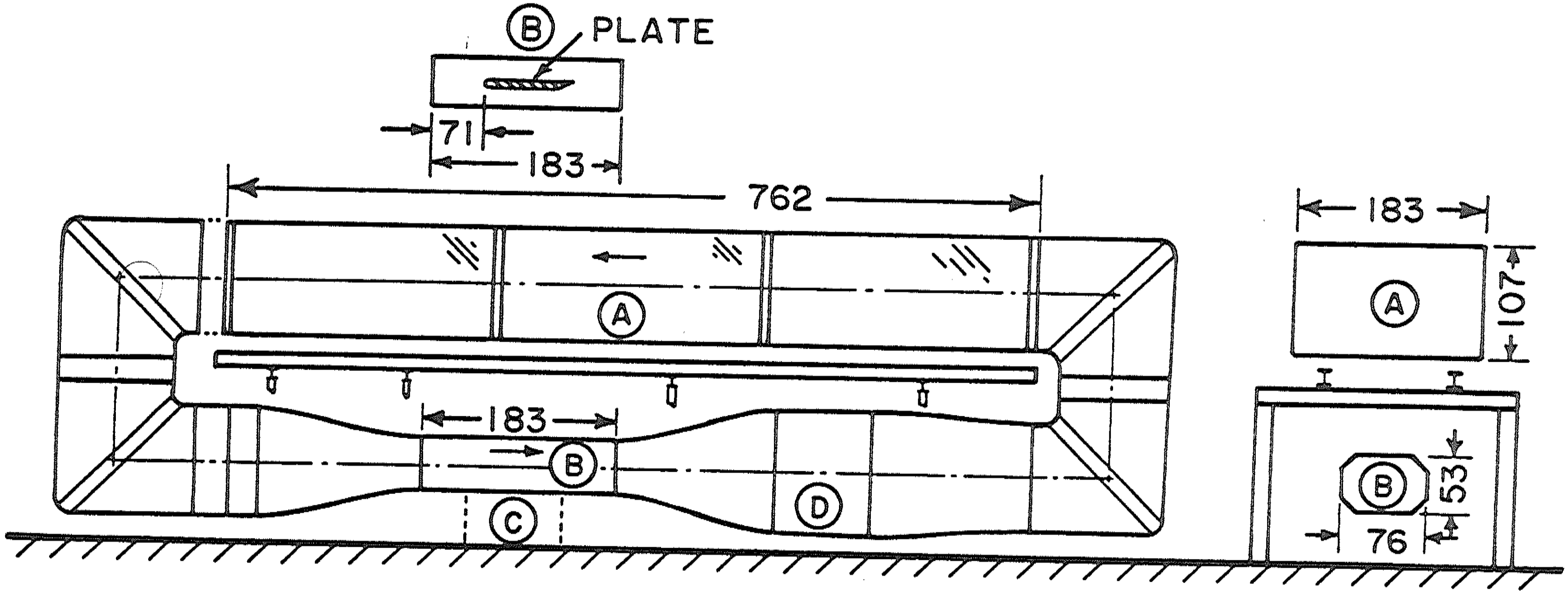

(A) UPPER TEST SECTION

(B) LOWER TEST SECTION

(C) BALANCE

(D) CONTRA-ROTATING FANS

(all dimensions are in Cm)

Figure 3: Low Speed Wind Tunnel.

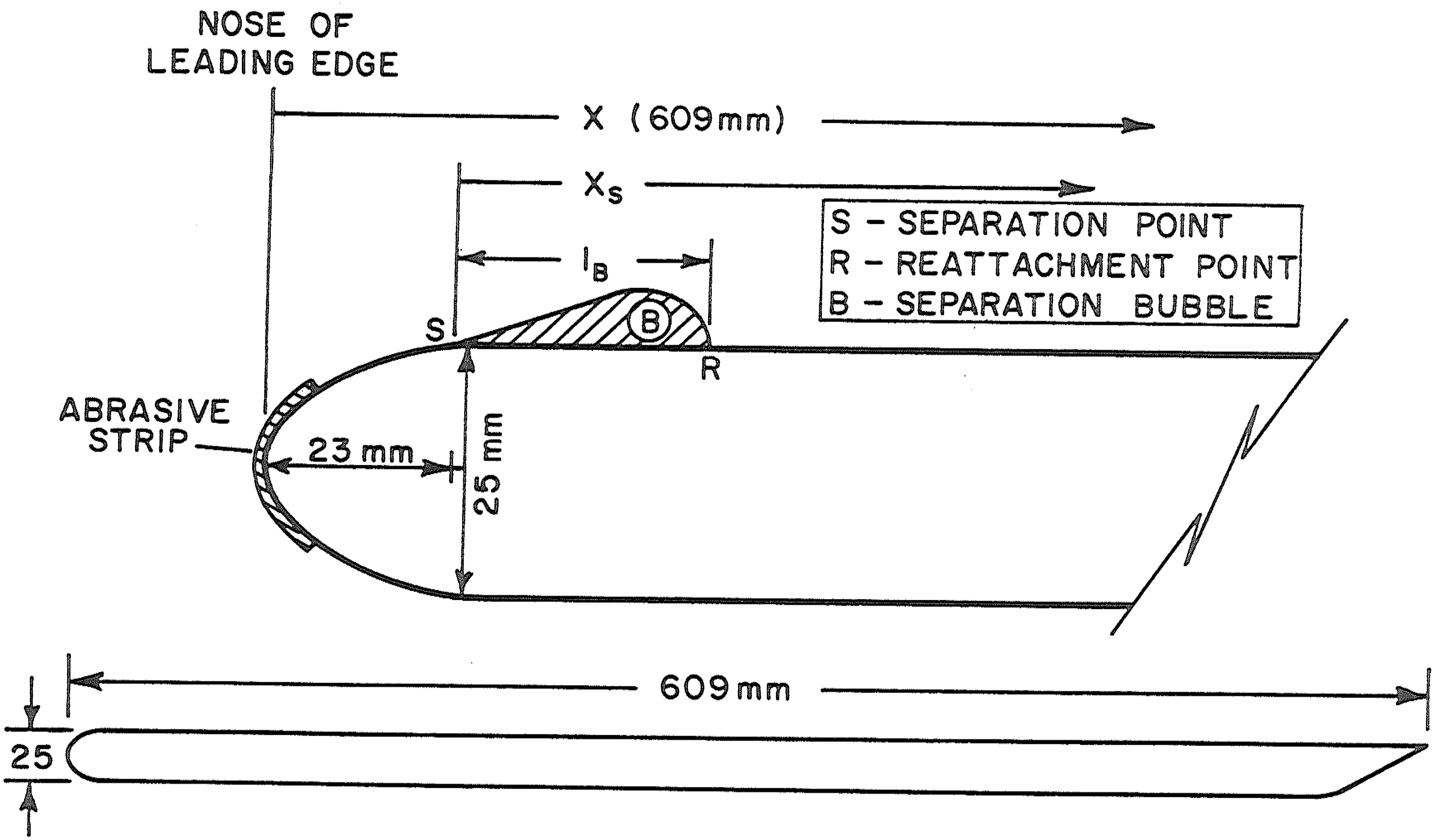

Figure 4: Experimental Plate.

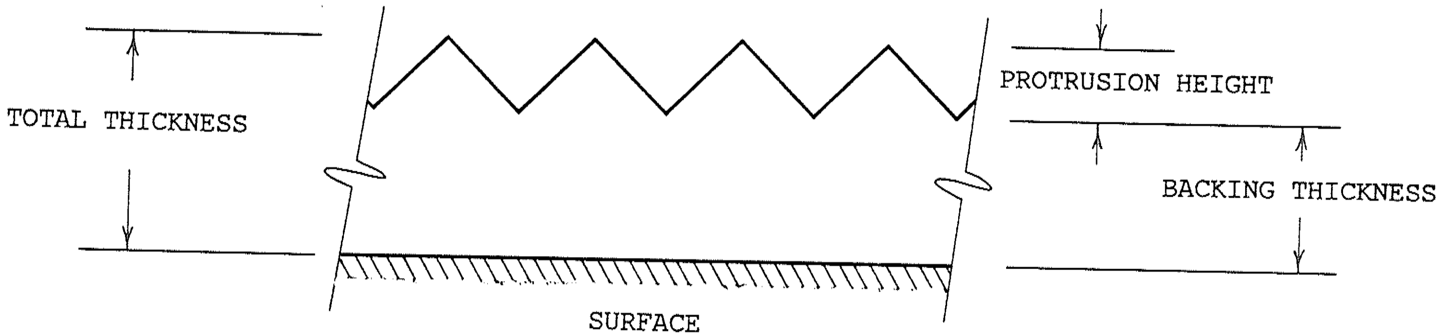

Figure 5: Sketch of Roughness Dimensions.

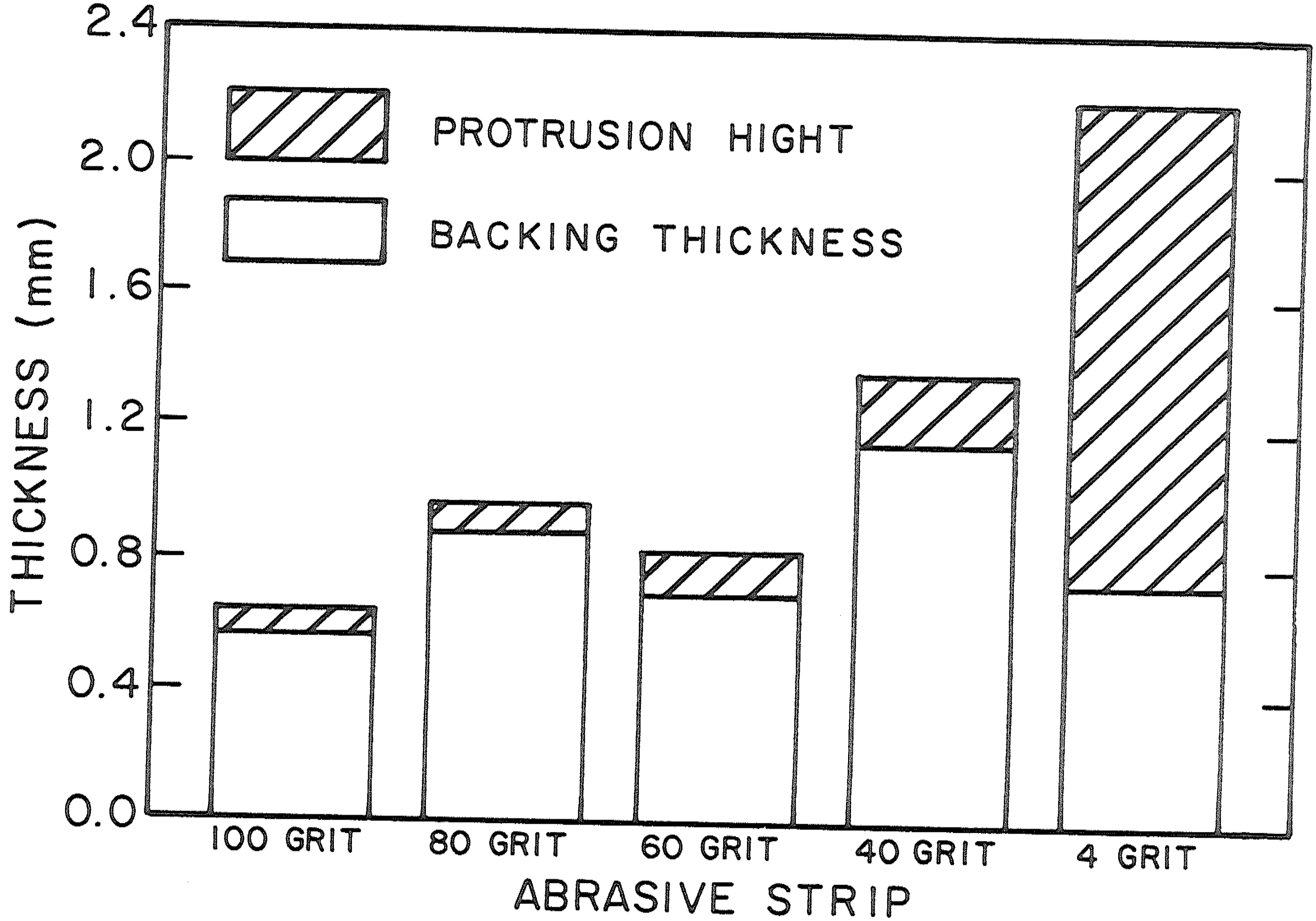

Figure 6: Comparison of Roughness Dimensions.

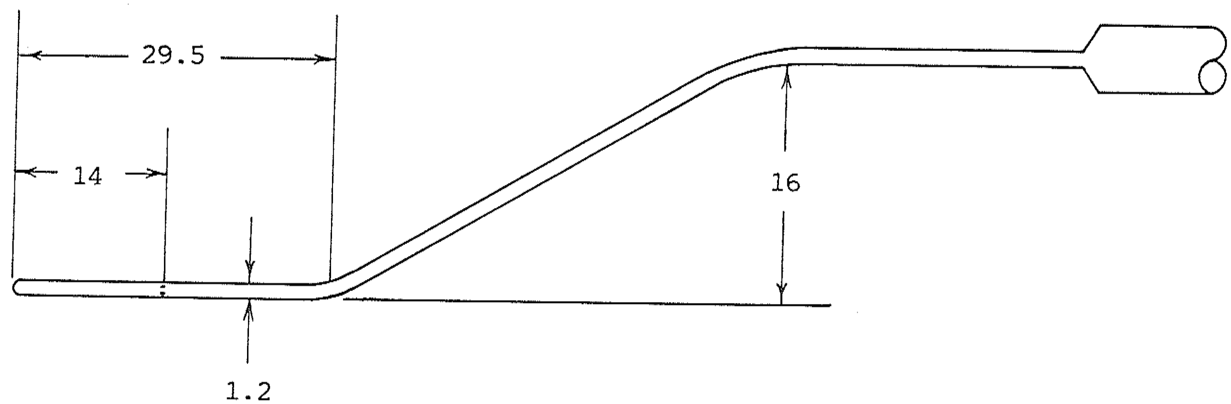

Figure 7: Pressure Probes (all dimensions in mm)

(a) Static Probe.

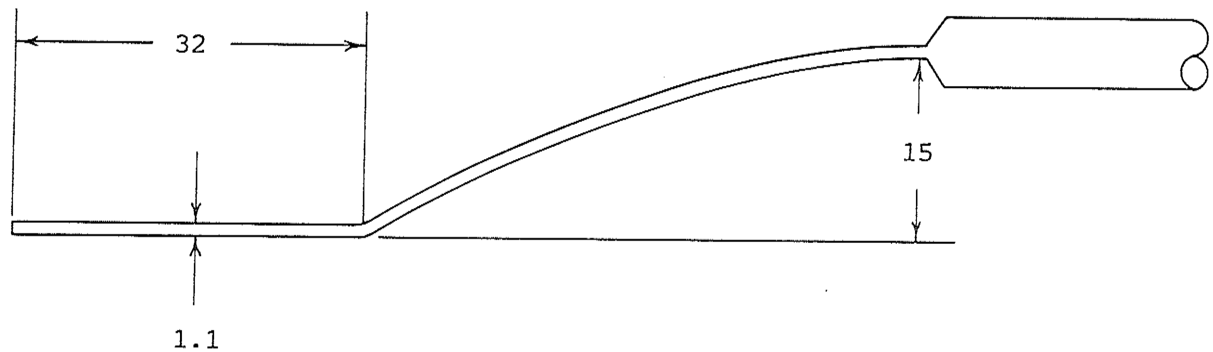

(b) Pitot Probe.

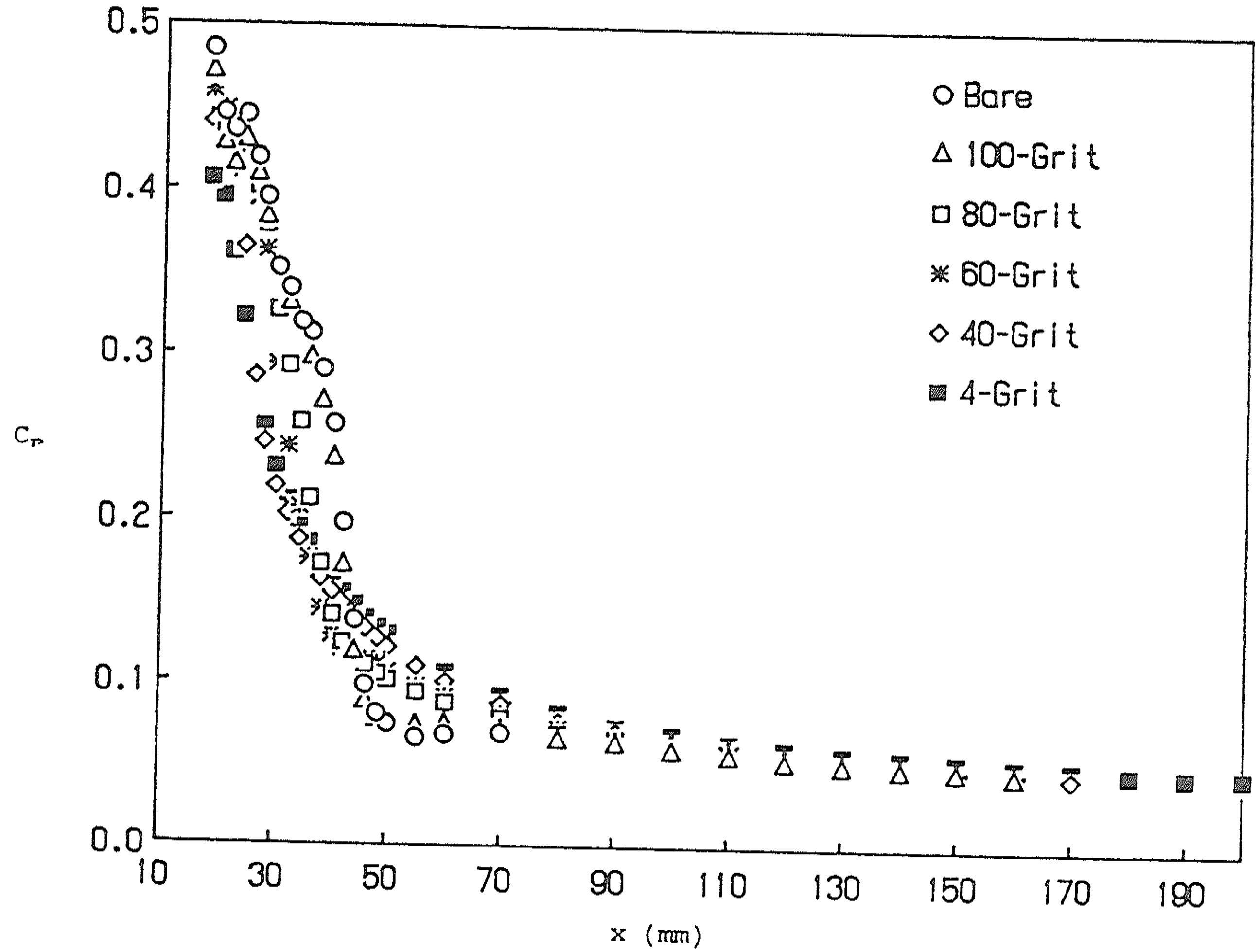

Figure 8: Pressure Coefficient Distribution.

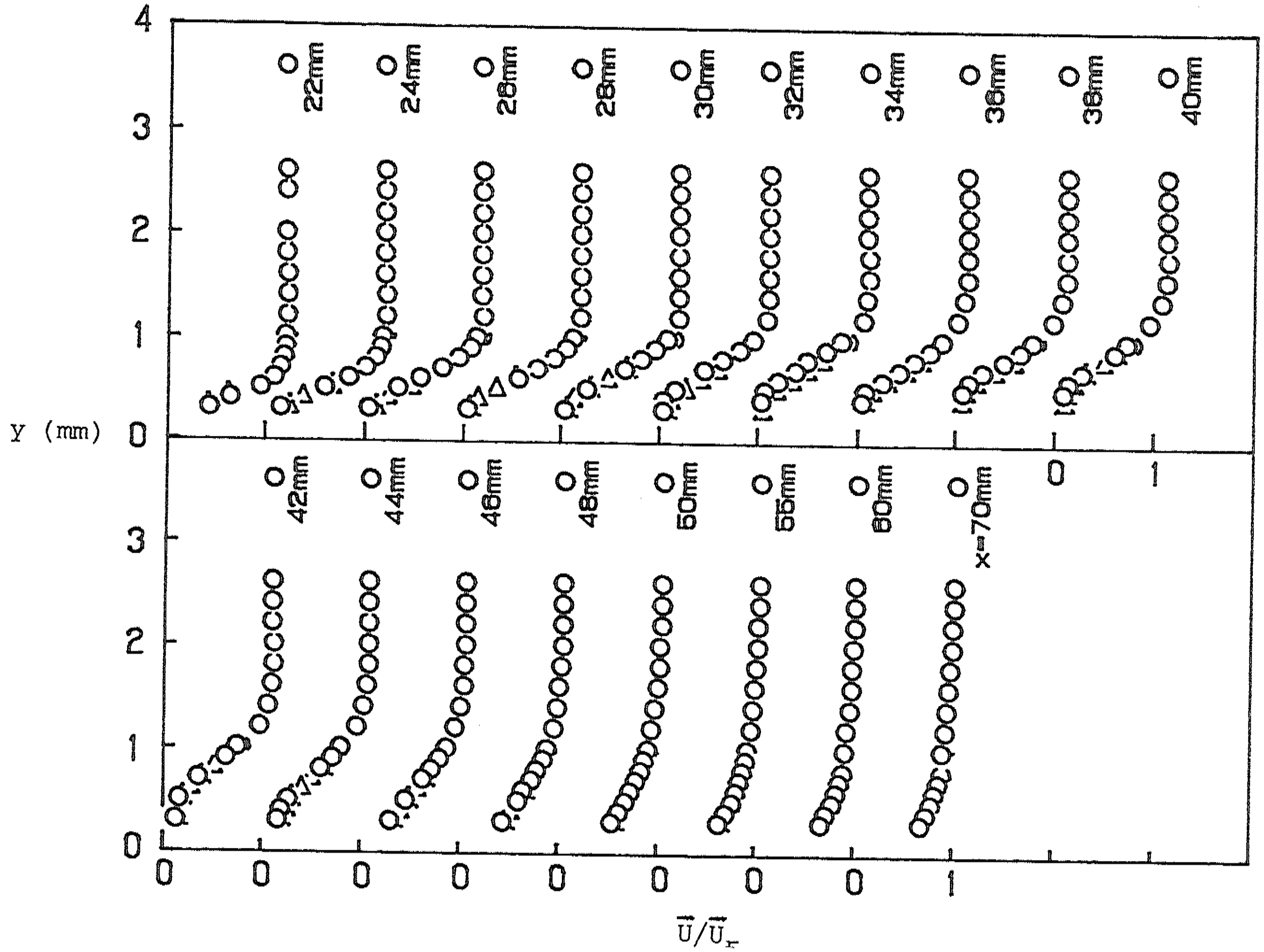

Figure 9: Mean Velocity Profiles

(a) Bare.

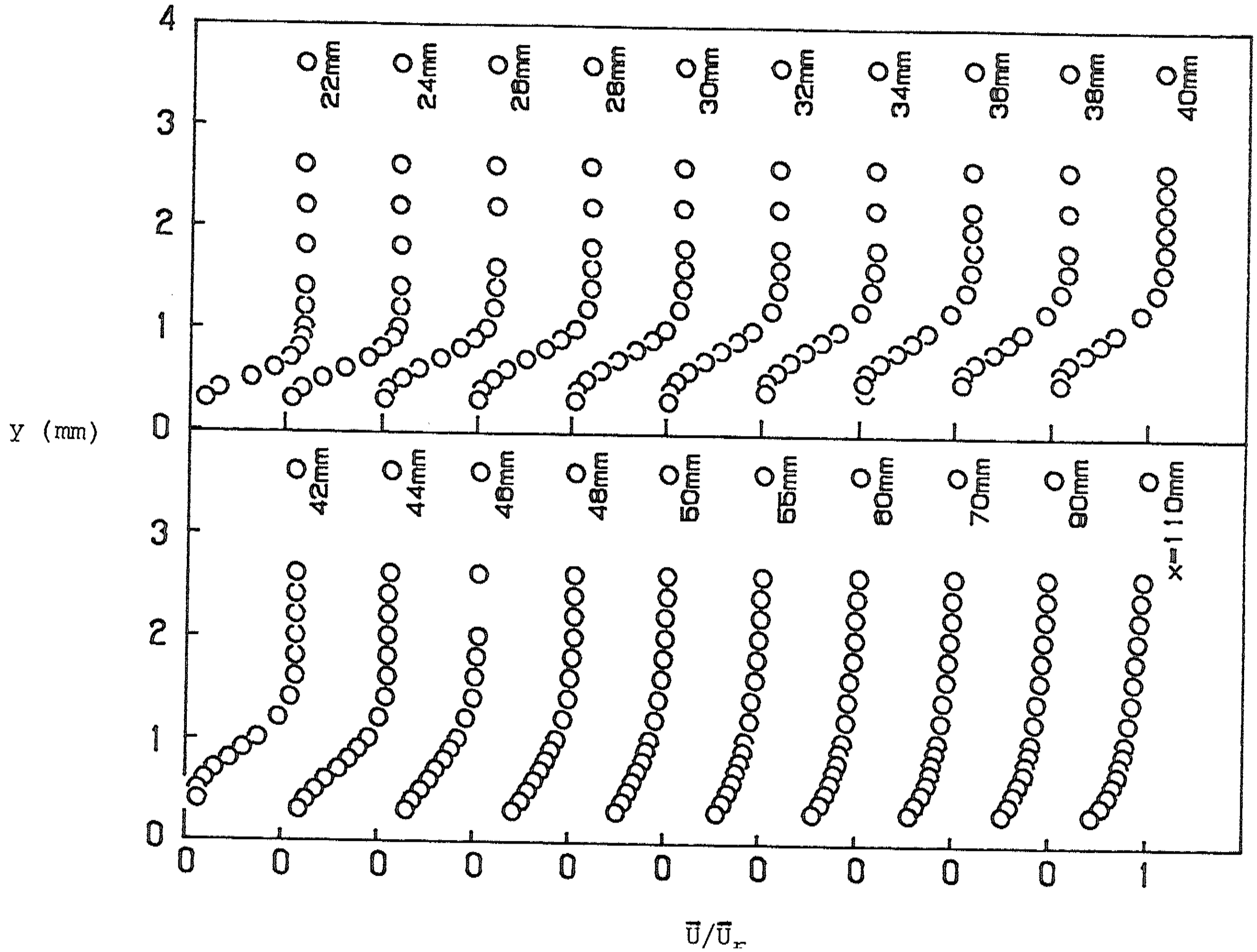
y (mm)
$\overline{U}/\overline{U}_r$
22mm
24mm
26mm
28mm
30mm
32mm
34mm
36mm
38mm
40mm
42mm
44mm
46mm
48mm
50mm
55mm
60mm
70mm
90mm
x=110mm

(b) 100-Grit.

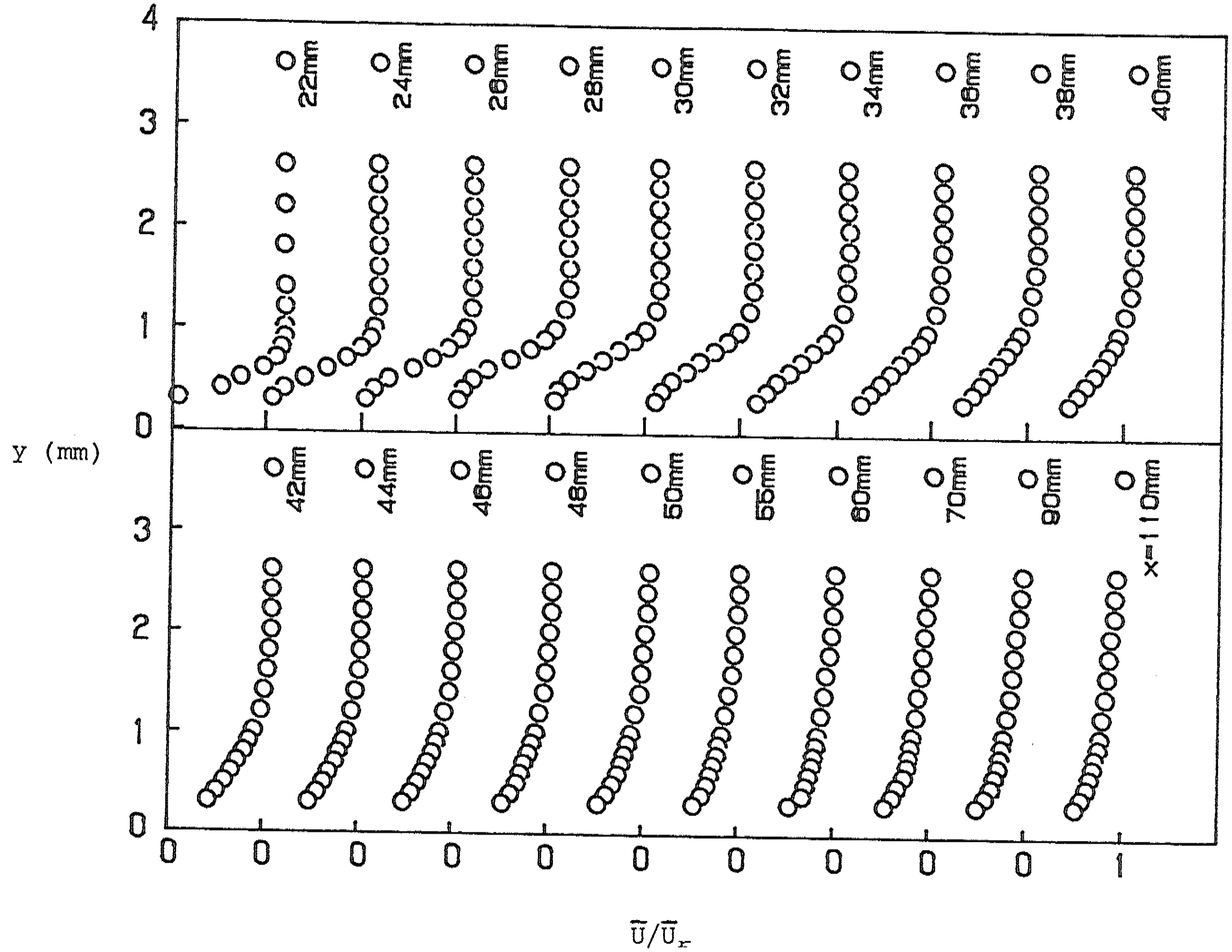

y (mm)
$\tilde{U}/\tilde{U}_r$
22mm
24mm
26mm
28mm
30mm
32mm
34mm
36mm
38mm
40mm
42mm
44mm
46mm
48mm
50mm
55mm
60mm
70mm
90mm
x=110mm

(c) 80-Grit.

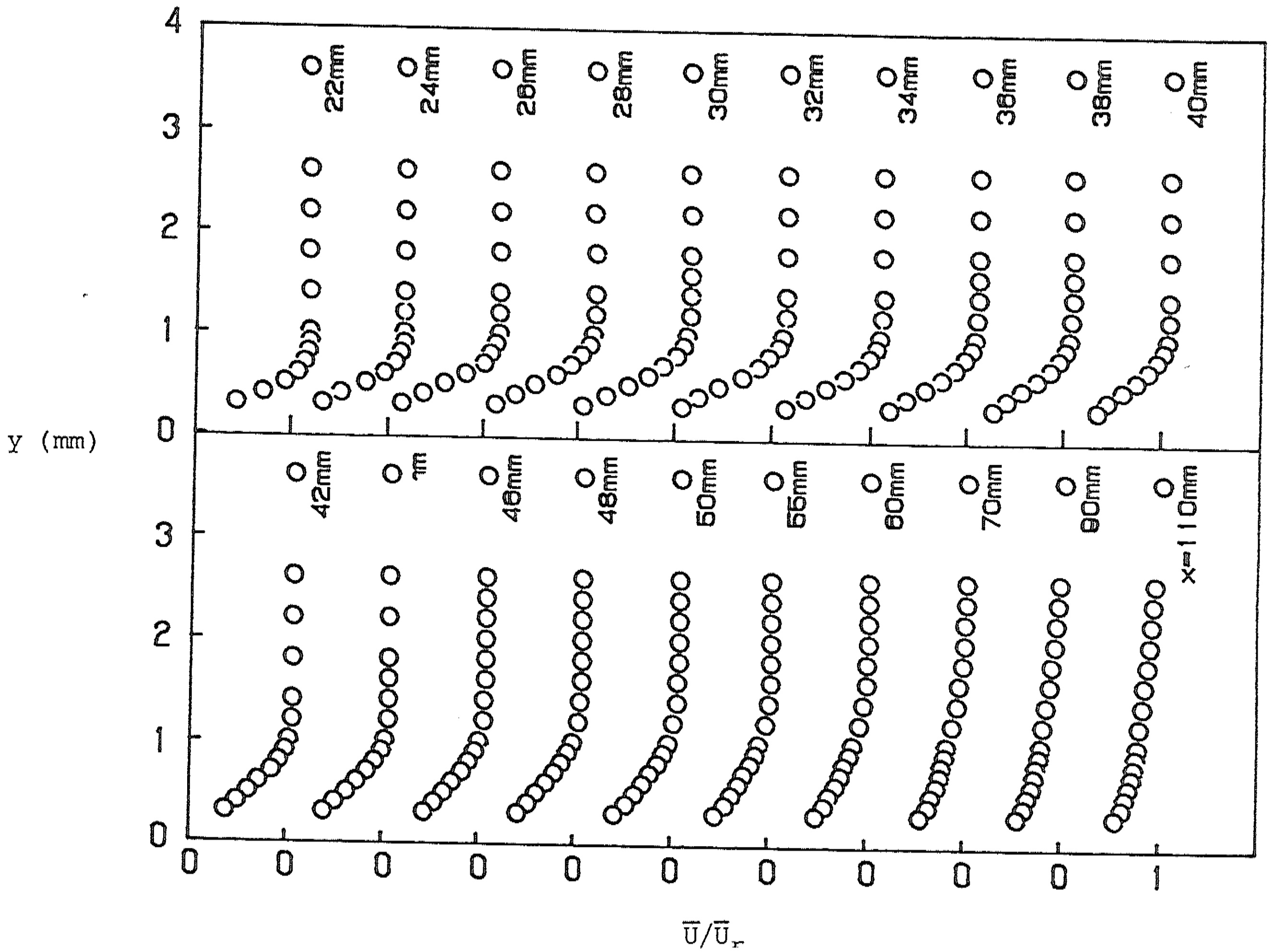

y (mm)
$\overline{U}/\overline{U}_r$
22mm
24mm
26mm
28mm
30mm
32mm
34mm
36mm
38mm
40mm
42mm
46mm
48mm
50mm
55mm
60mm
70mm
90mm
x=110mm

(d) 60-Grit.

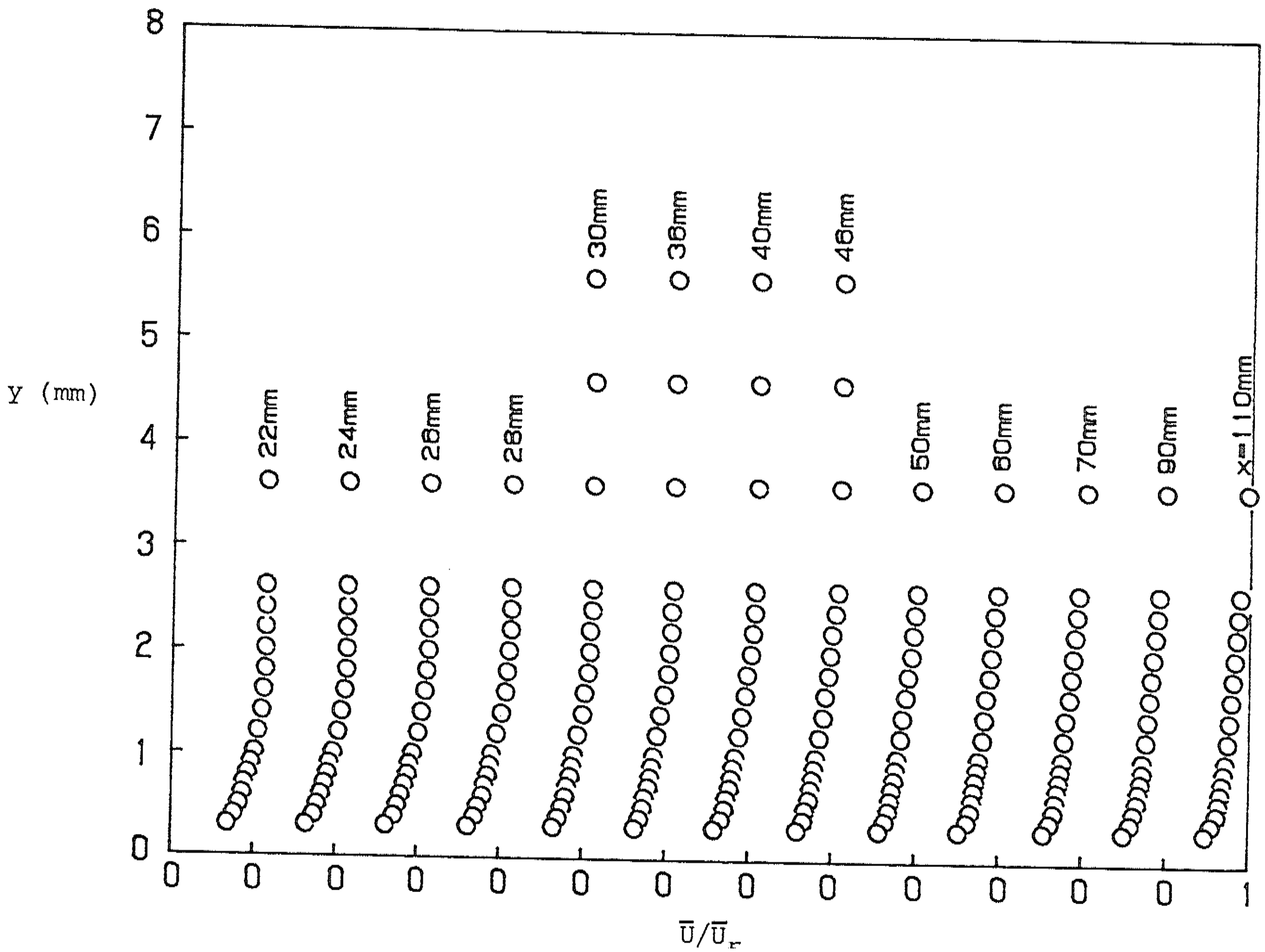

8
7
6
5
4
3
2
1
0
y (mm)
30mm
36mm
40mm
46mm
22mm
24mm
26mm
28mm
50mm
60mm
70mm
90mm
x=110mm
0
0
0
0
0
0
0
0
0
0
0
0
0
1
$\overline{U}/\overline{U}_r$

(e) 40-Grit.

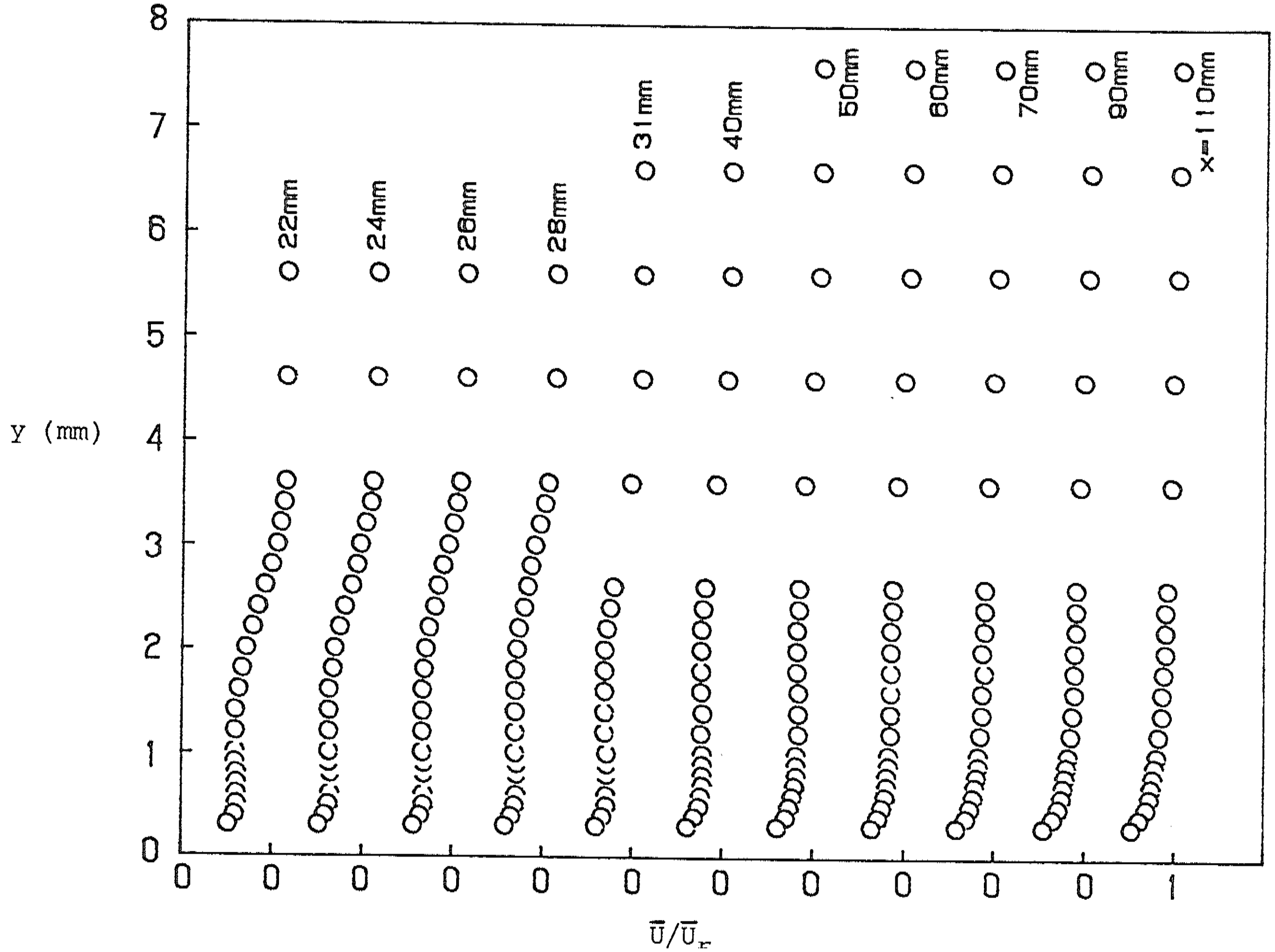
y (mm)
0
1
2
3
4
5
6
7
8
22mm
24mm
26mm
28mm
31mm
40mm
50mm
60mm
70mm
90mm
x=110mm
0 0 0 0 0 0 0 0 0 0 0 1
$\overline{U}/\overline{U}_r$

(f) 4-Grit.

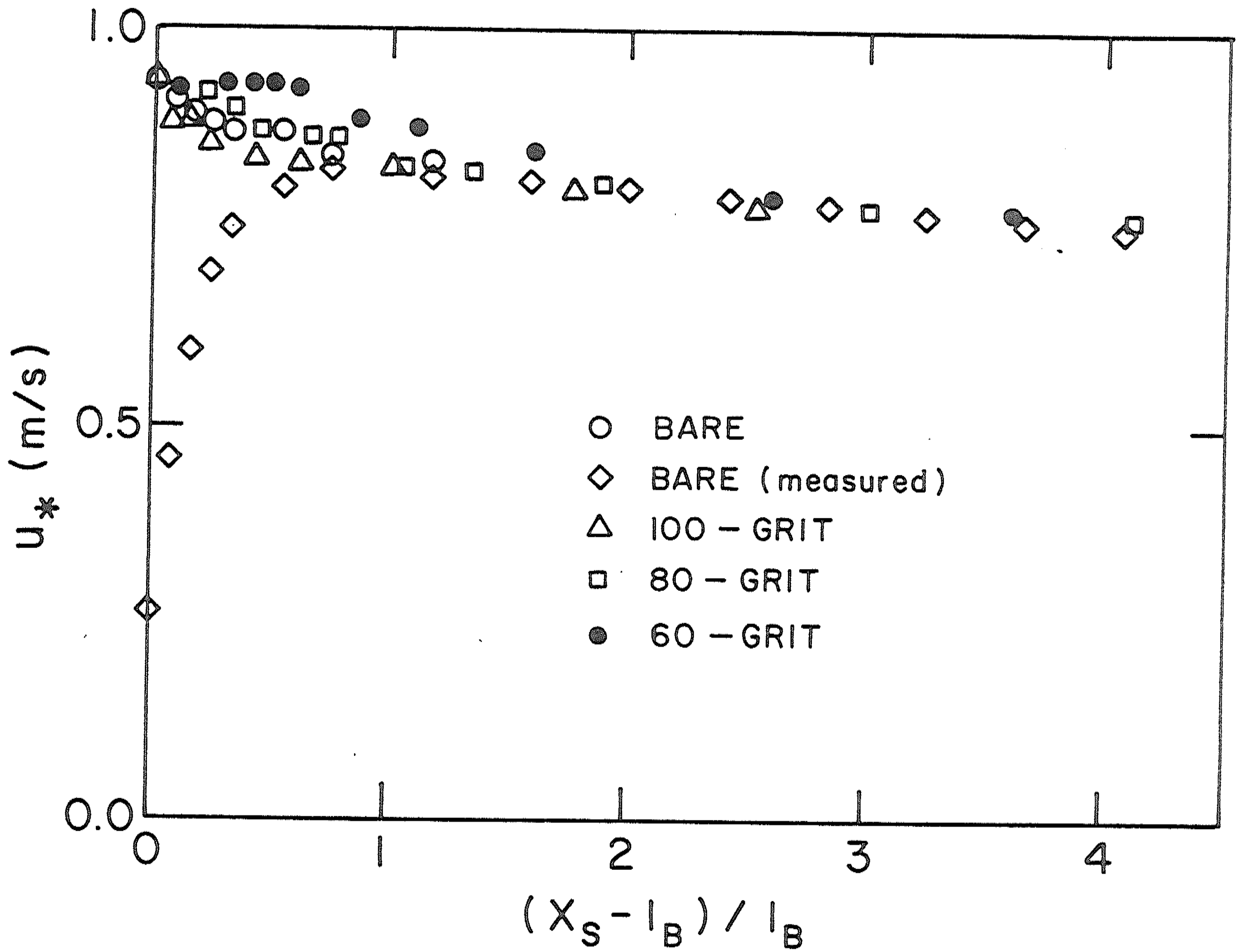

Figure 10: Estimation of Friction Velocity Downstream of Reattachment.

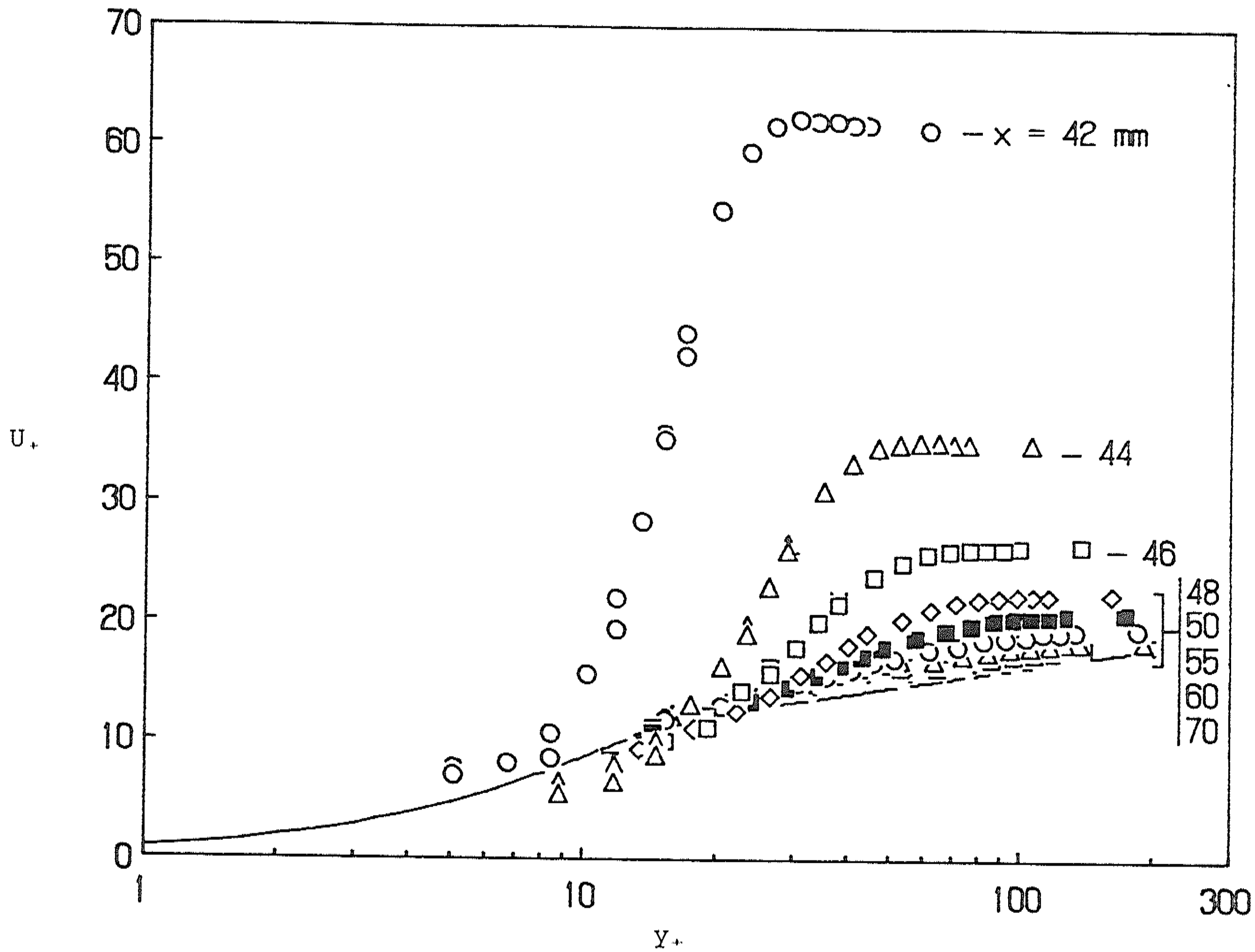

Figure 11: Normalized Mean Velocity Profiles

(a) Bare.

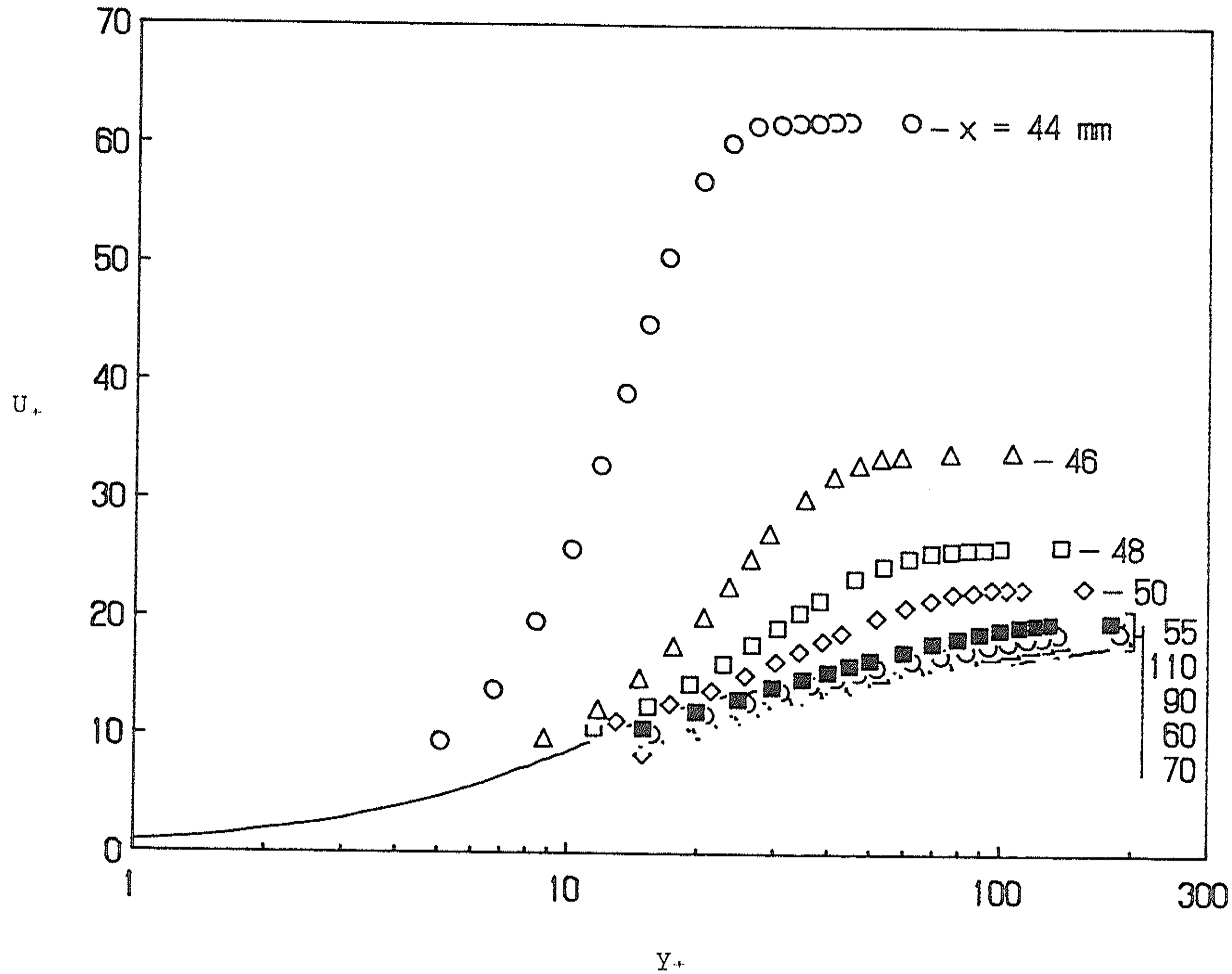

(b) 100-Grit.

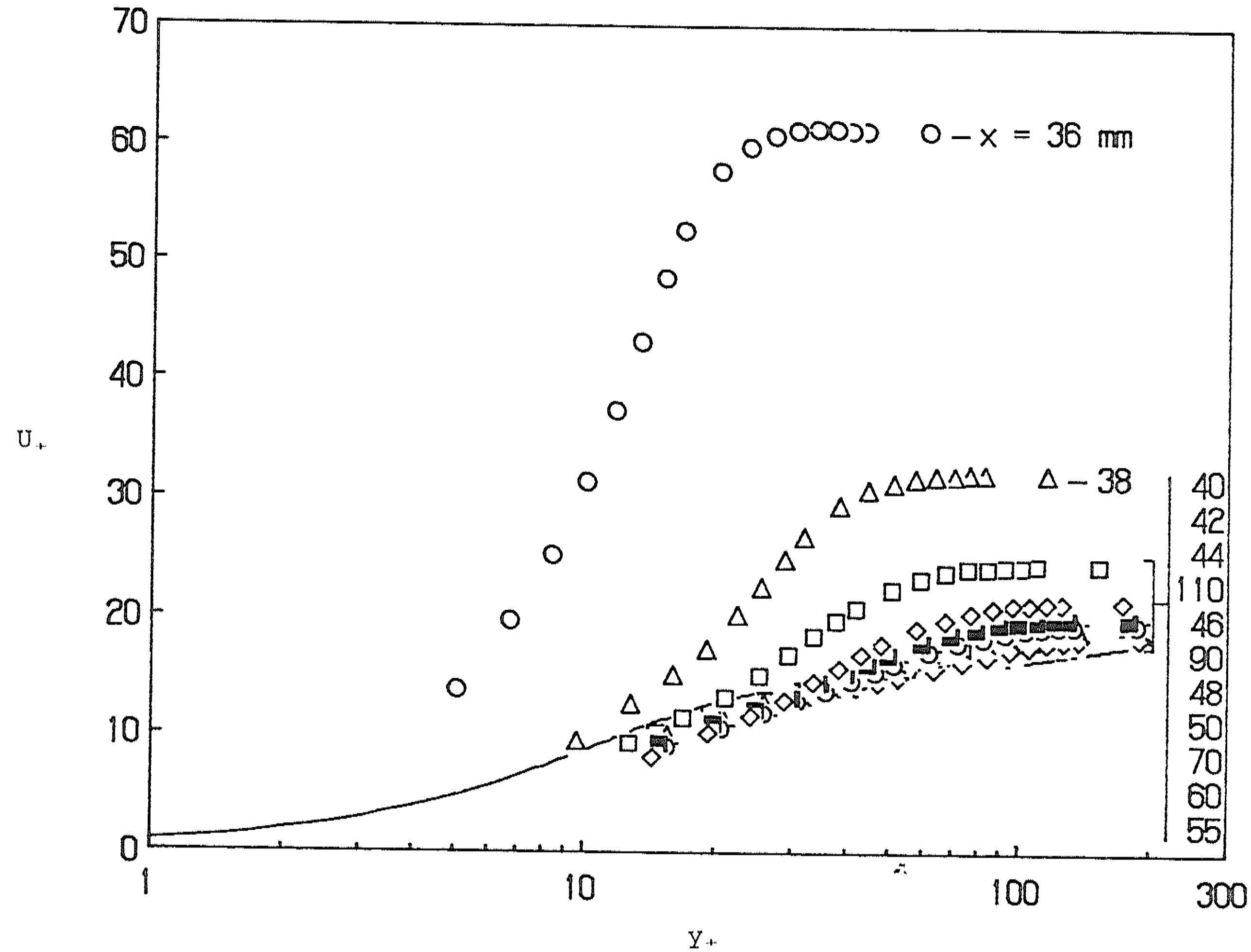

70
60
50
40
30
20
10
0
U+
1
10
100
300
Y+
O – x = 36 mm
Δ – 38
40
42
44
110
46
90
48
50
70
60
55

(c) 80-Grit.

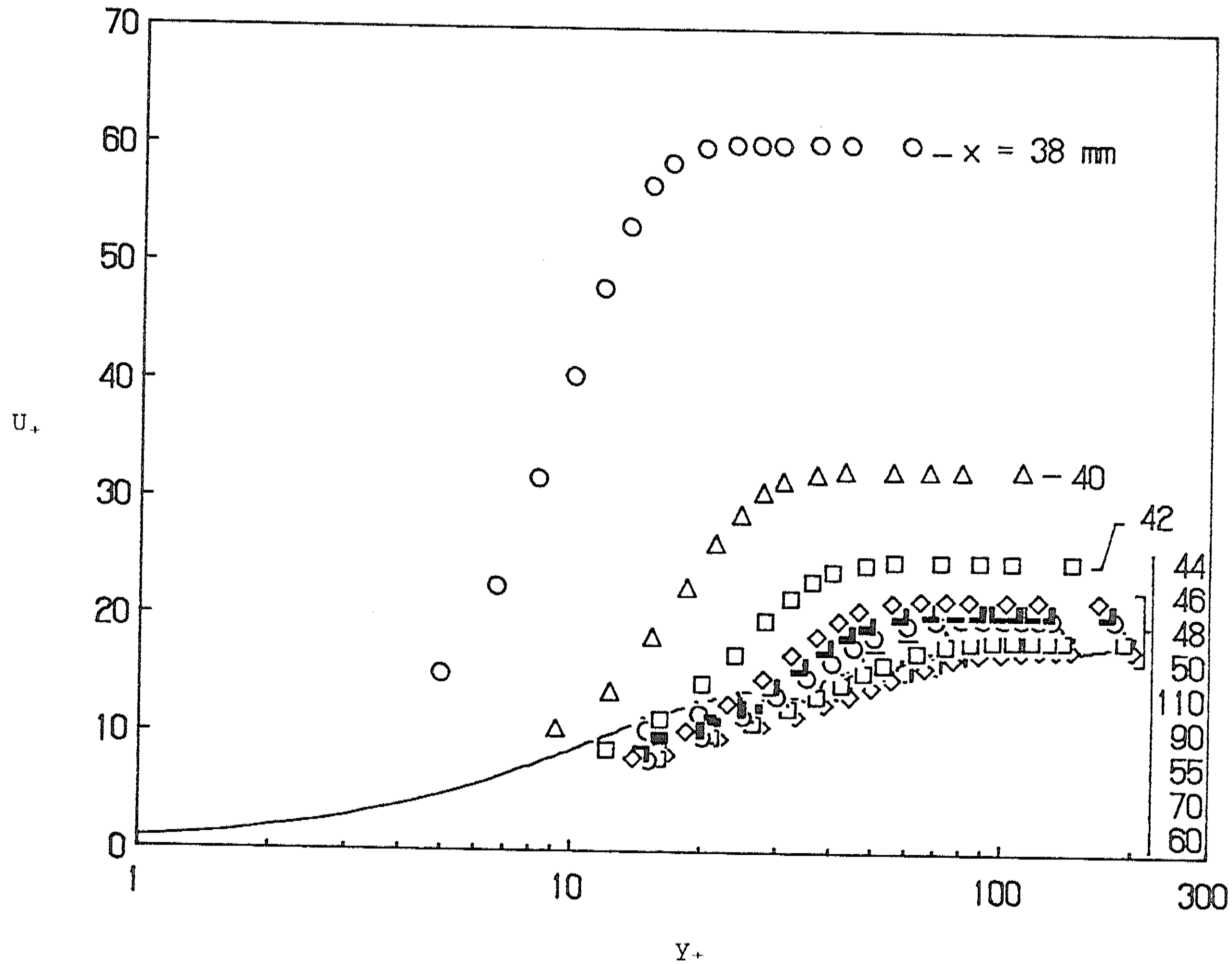

70
60
50
40
30
20
10
0
U+
1
10
100
300
Y+
O – x = 38 mm
Δ – 40
42
44
46
48
50
110
90
55
70
60

(d) 60-Grit.

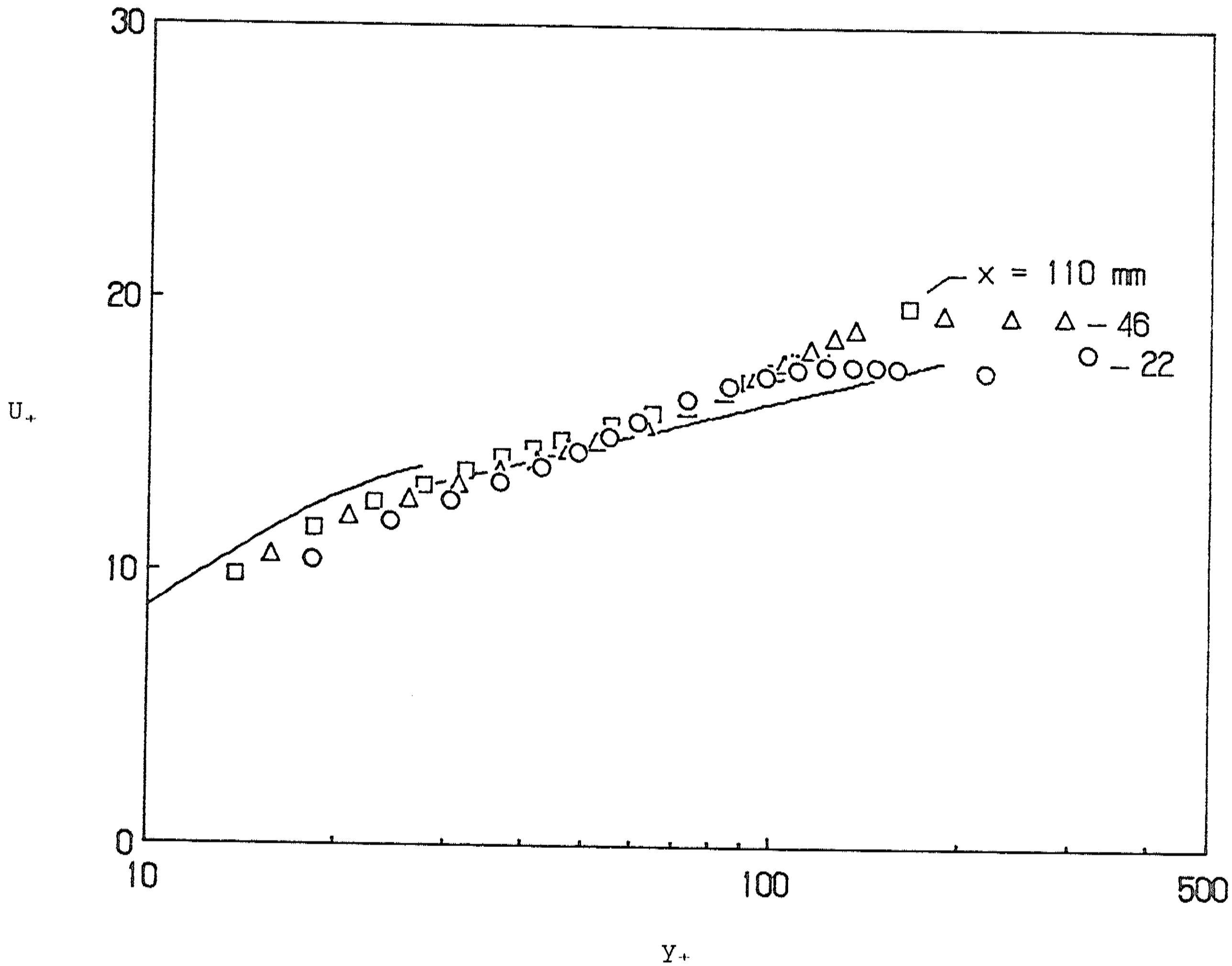

(e) 40-Grit.

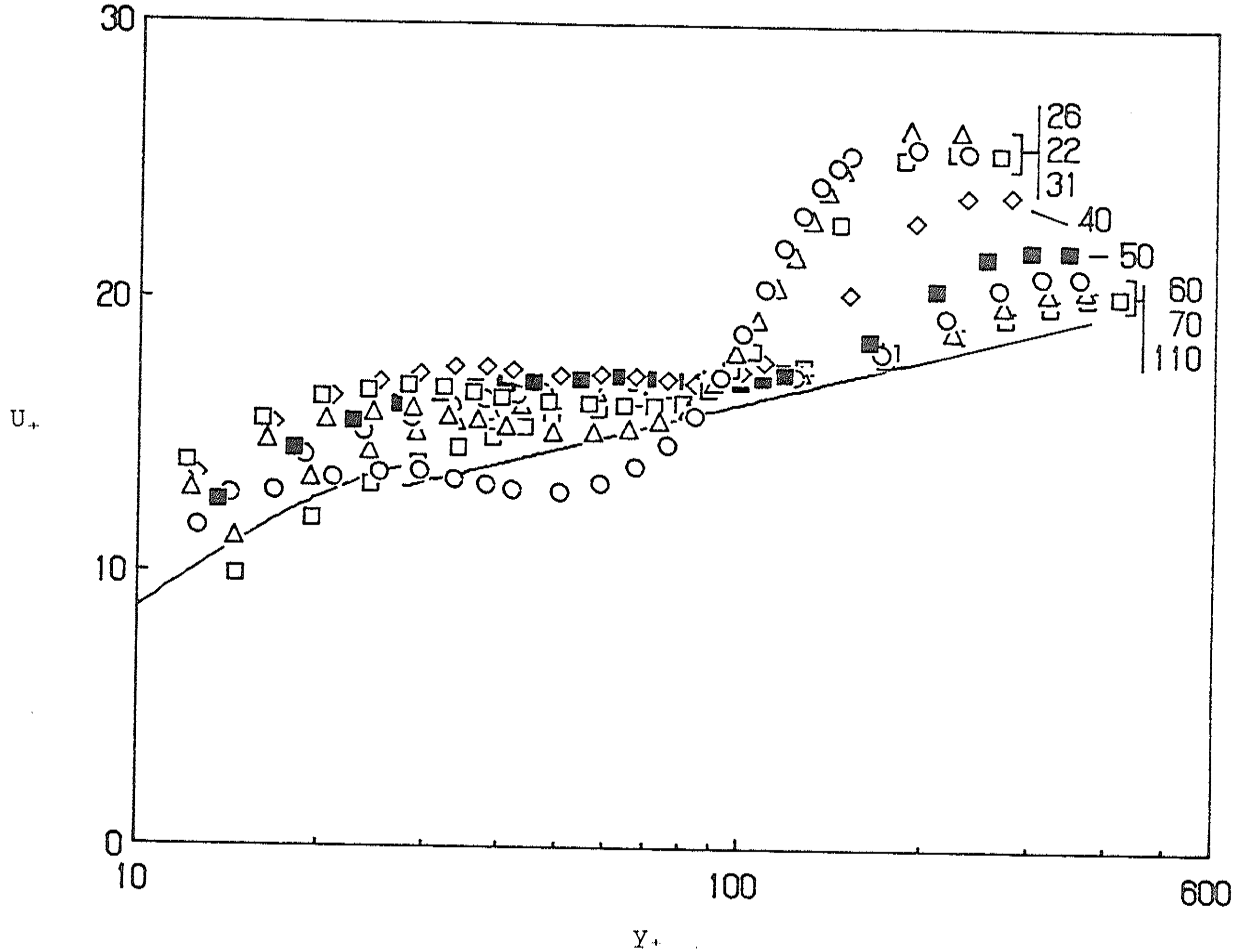

(f) 4-Grit.

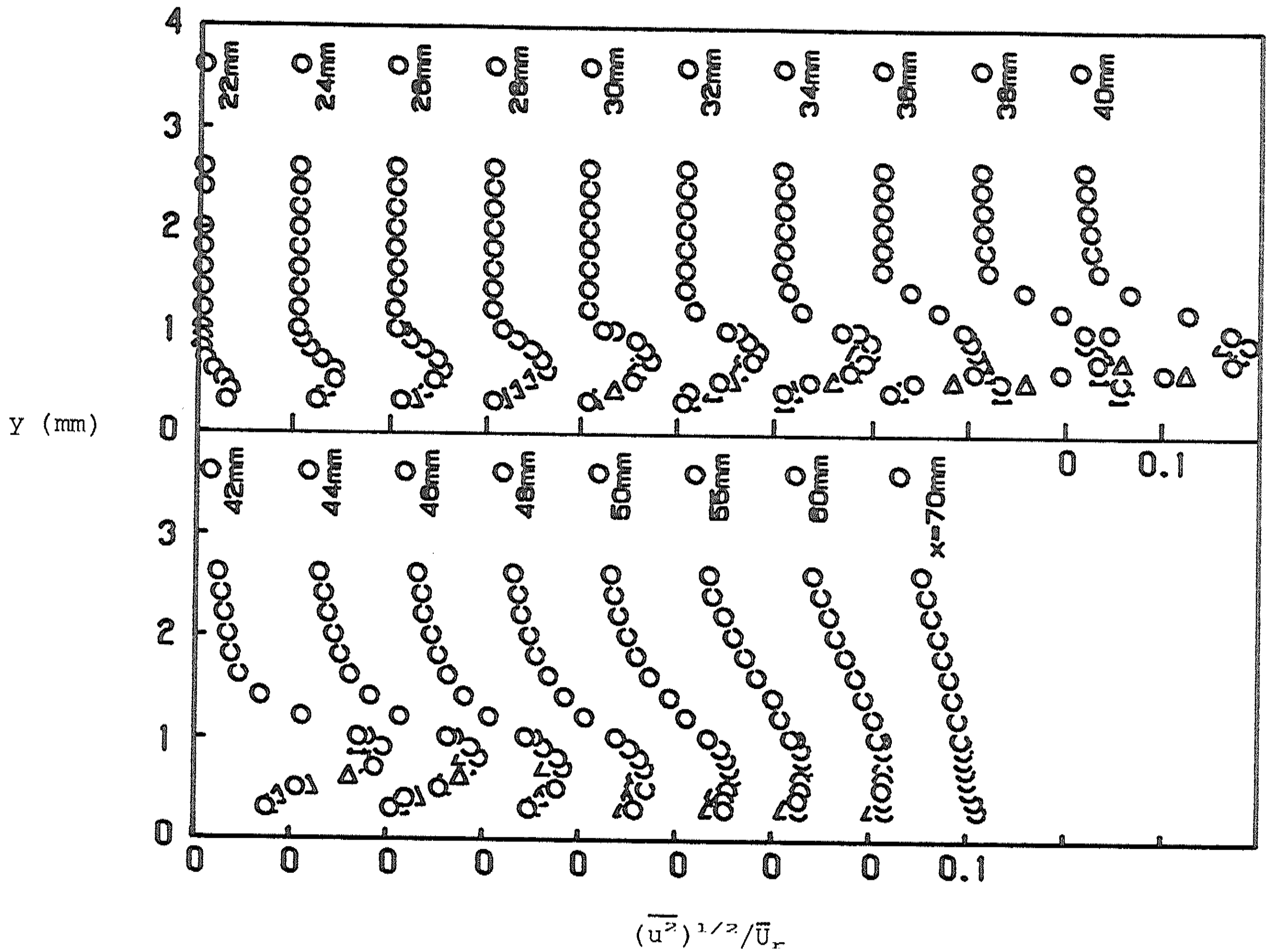

Figure 12: Turbulence Intensity Profiles

(a) Bare.

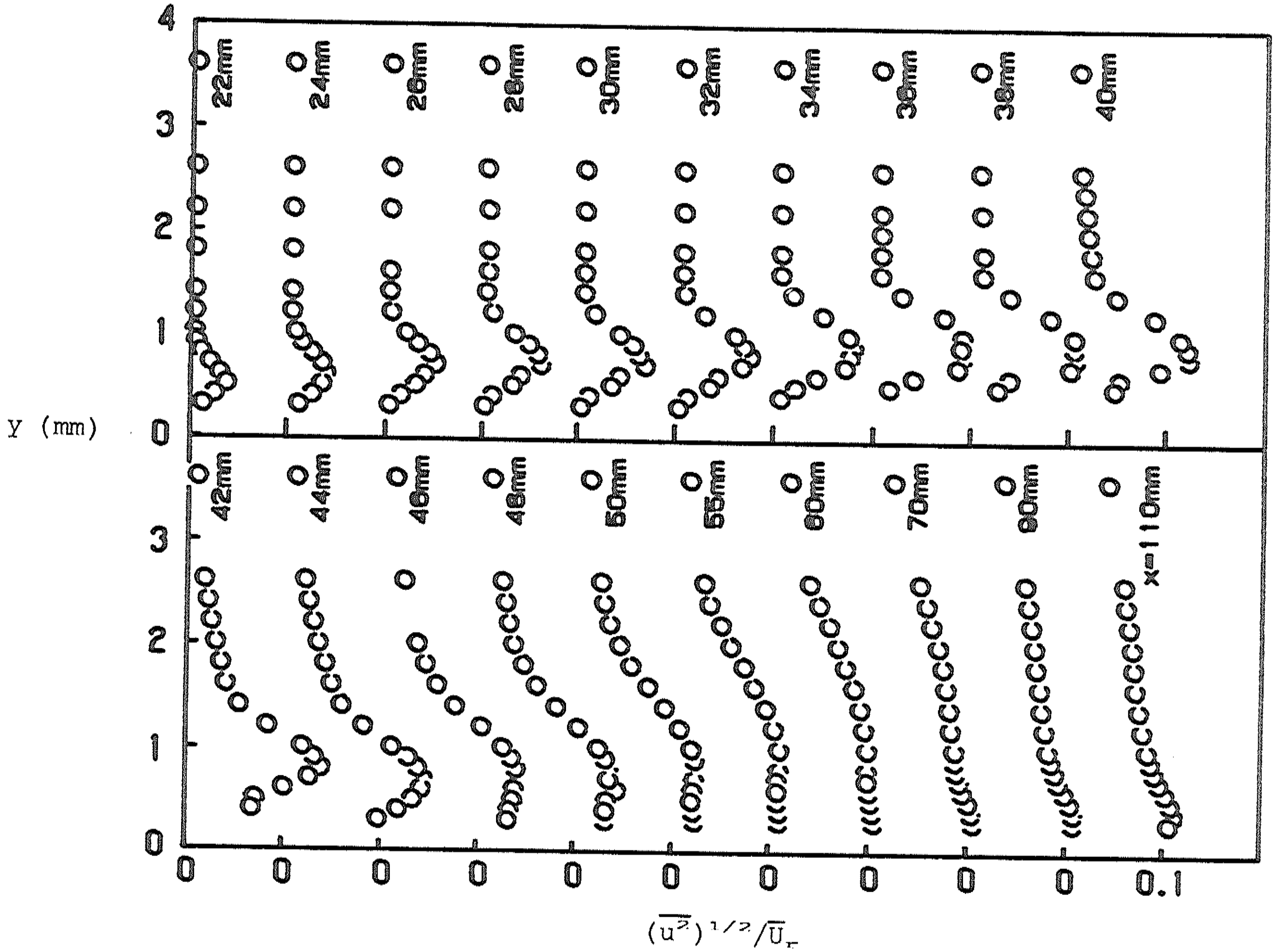
Y (mm)
22mm
24mm
26mm
28mm
30mm
32mm
34mm
36mm
38mm
40mm
42mm
44mm
46mm
48mm
50mm
55mm
60mm
70mm
90mm
x=110mm
0
1
2
3
4
0.1
$(\overline{u^2})^{1/2}/\overline{U}_r$

(b) 100-Grit.

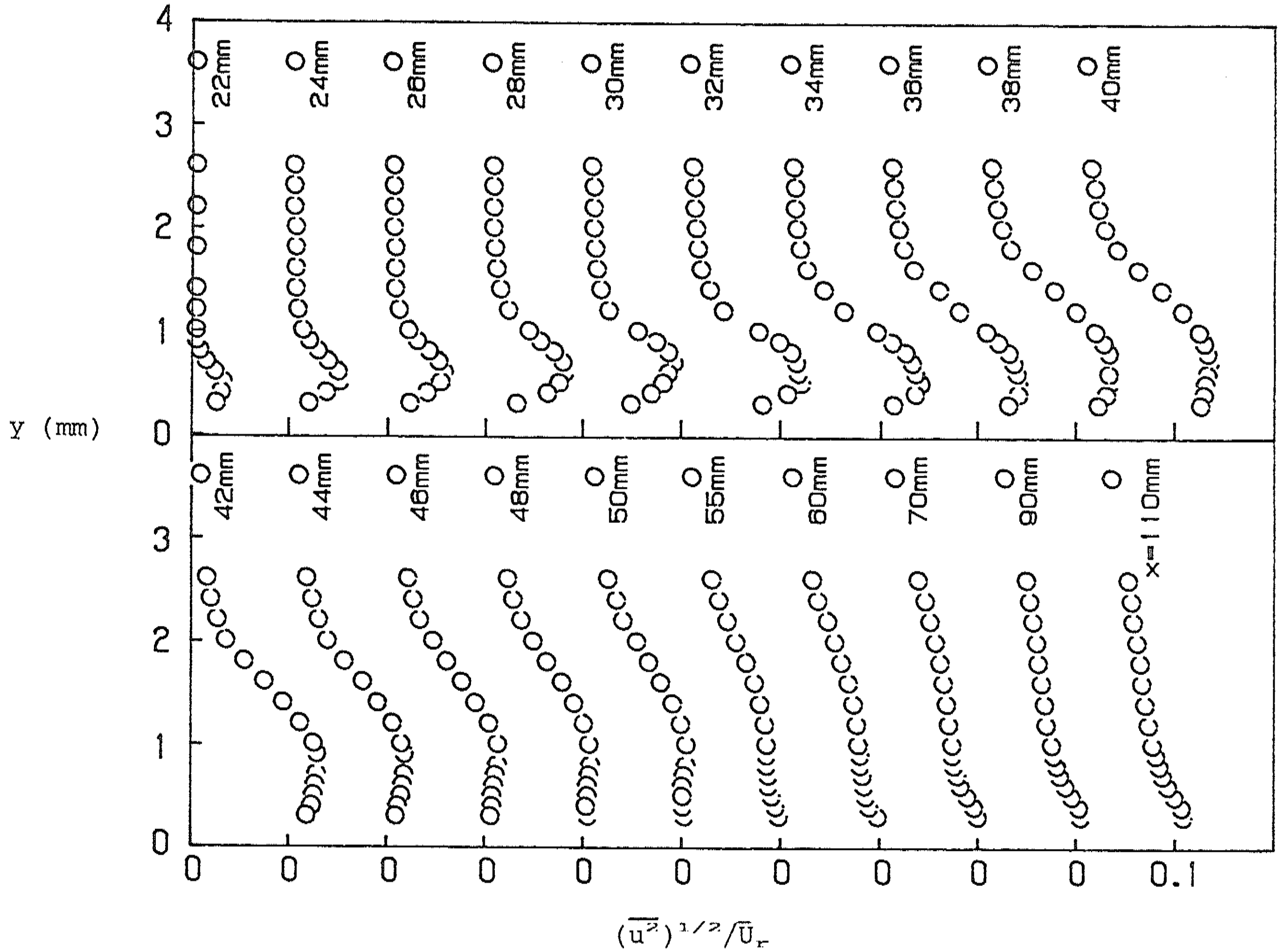

y (mm)
22mm
24mm
26mm
28mm
30mm
32mm
34mm
36mm
38mm
40mm
42mm
44mm
46mm
48mm
50mm
55mm
60mm
70mm
90mm
x=110mm
0
1
2
3
4
0.1
$(\overline{u^2})^{1/2}/\bar{U}_r$

(c) 80-Grit.

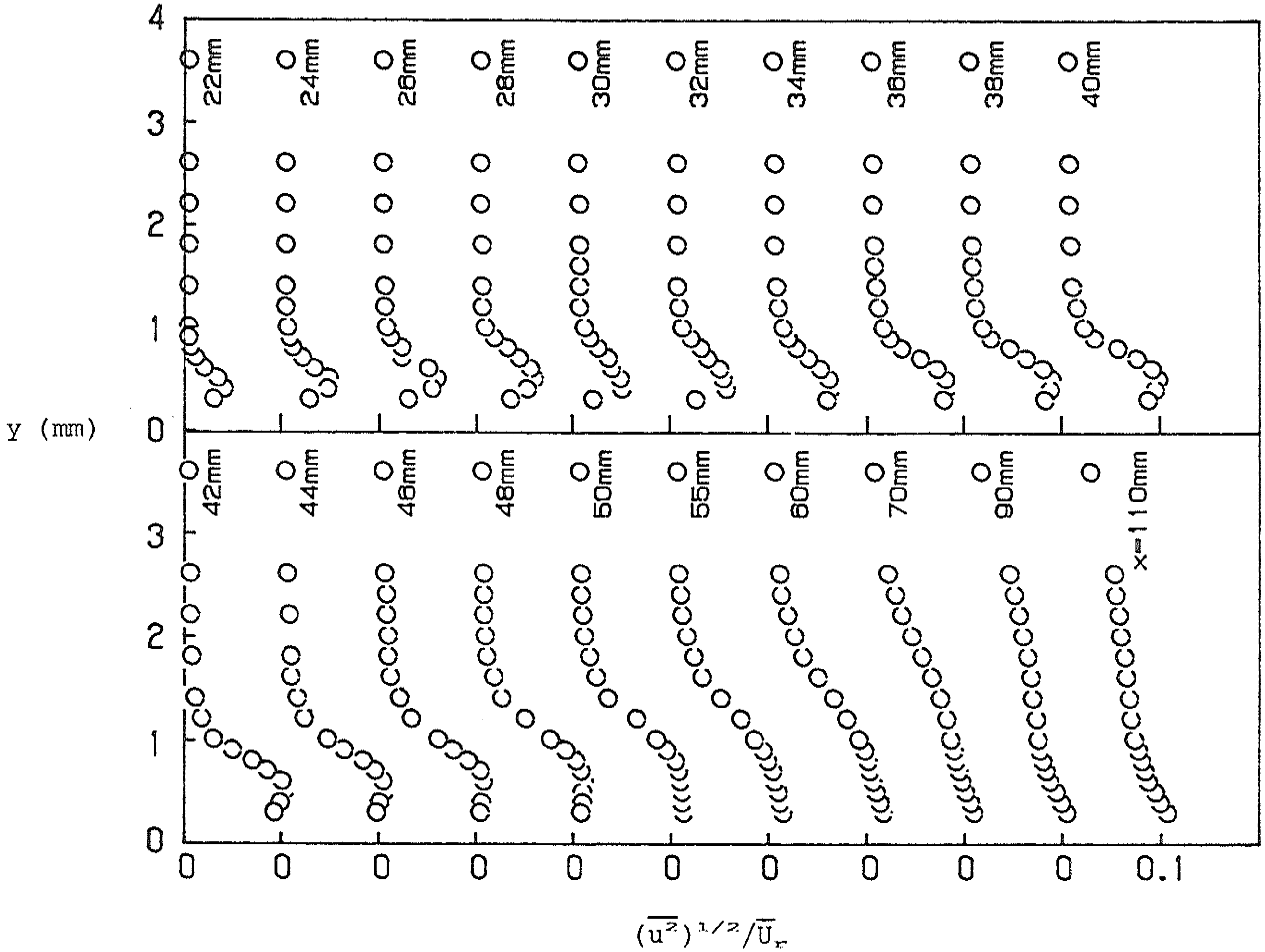
y (mm)
0
1
2
3
4
22mm
24mm
26mm
28mm
30mm
32mm
34mm
36mm
38mm
40mm
42mm
44mm
46mm
48mm
50mm
55mm
60mm
70mm
90mm
x=110mm
0
0.1
$(\overline{u^2})^{1/2}/\overline{U}_r$

(d) 60-Grit.

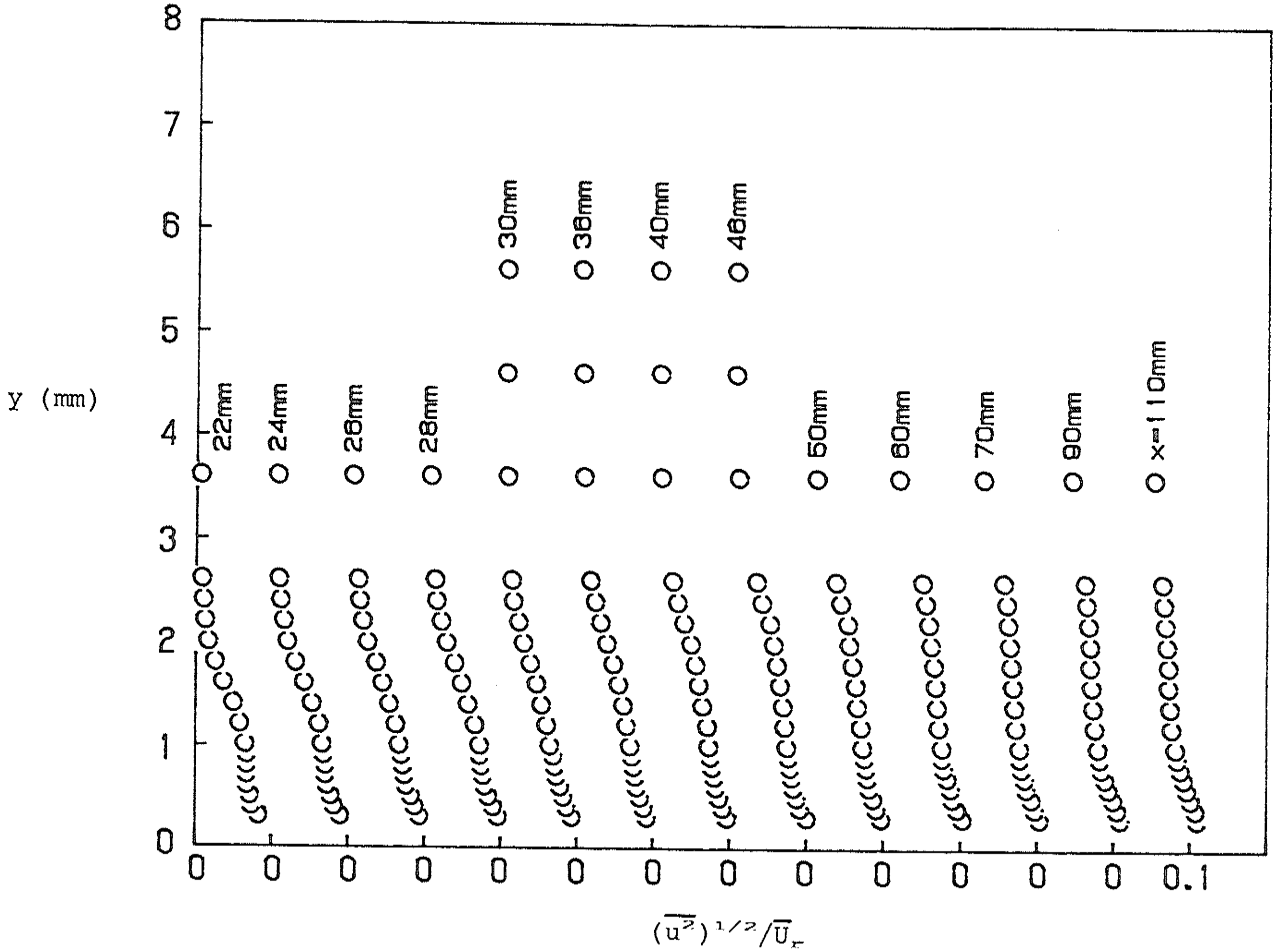

y (mm)
8
7
6
5
4
3
2
1
0
22mm
24mm
26mm
28mm
30mm
36mm
40mm
46mm
50mm
60mm
70mm
90mm
x=110mm
0 0 0 0 0 0 0 0 0 0 0 0 0 0.1
$(\overline{u^2})^{1/2}/\overline{U}_r$

(e) 40-Grit.

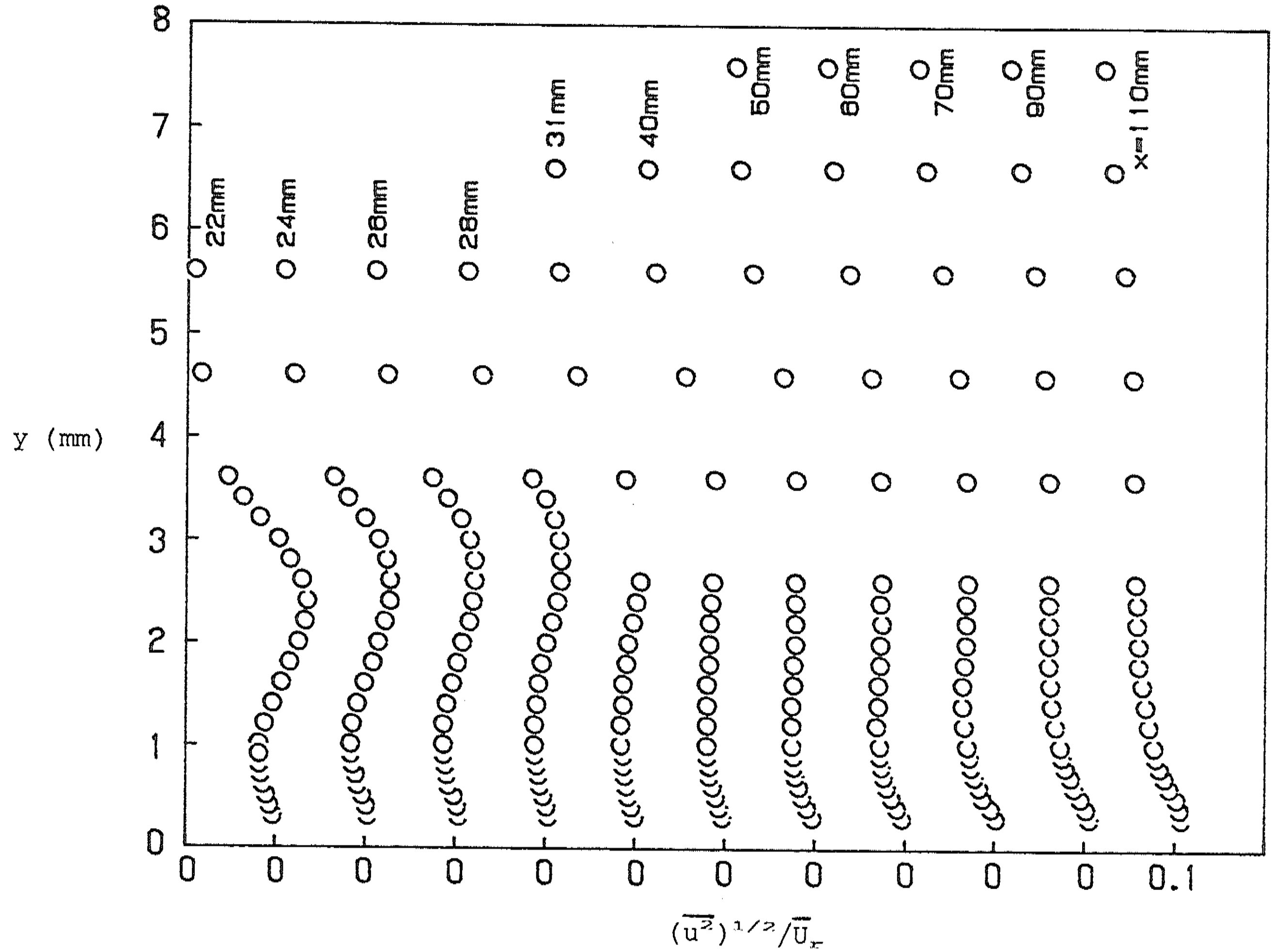

y (mm)
8
7
6
5
4
3
2
1
0
0
0
0
0
0
0
0
0
0
0
0
0.1
22mm
24mm
26mm
28mm
31mm
40mm
50mm
60mm
70mm
90mm
x=110mm
$(\overline{u^2})^{1/2}/\overline{U}_r$

(f) 4-Grit.

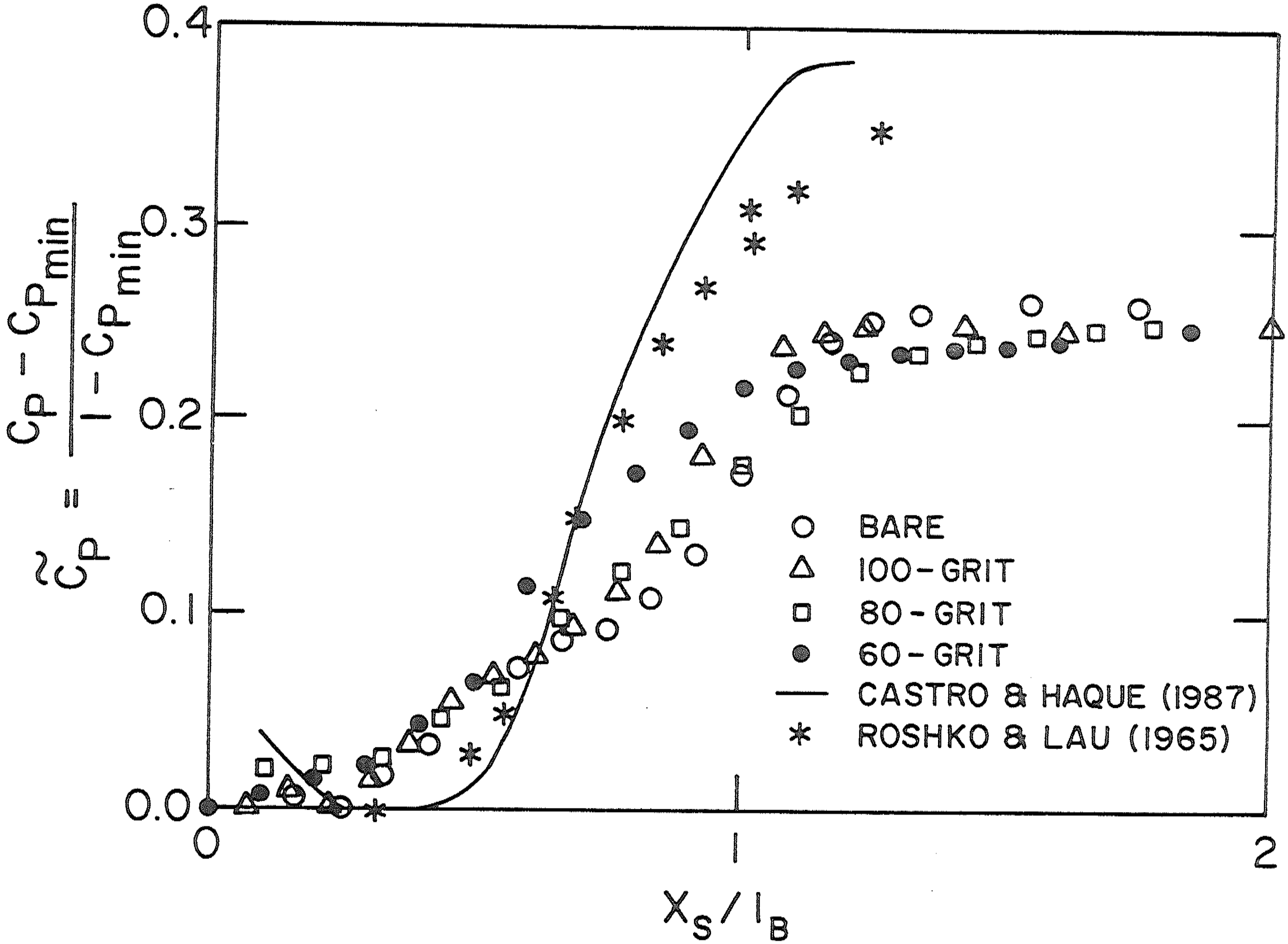

Figure 13: Reduced Pressure Coefficient Distribution.

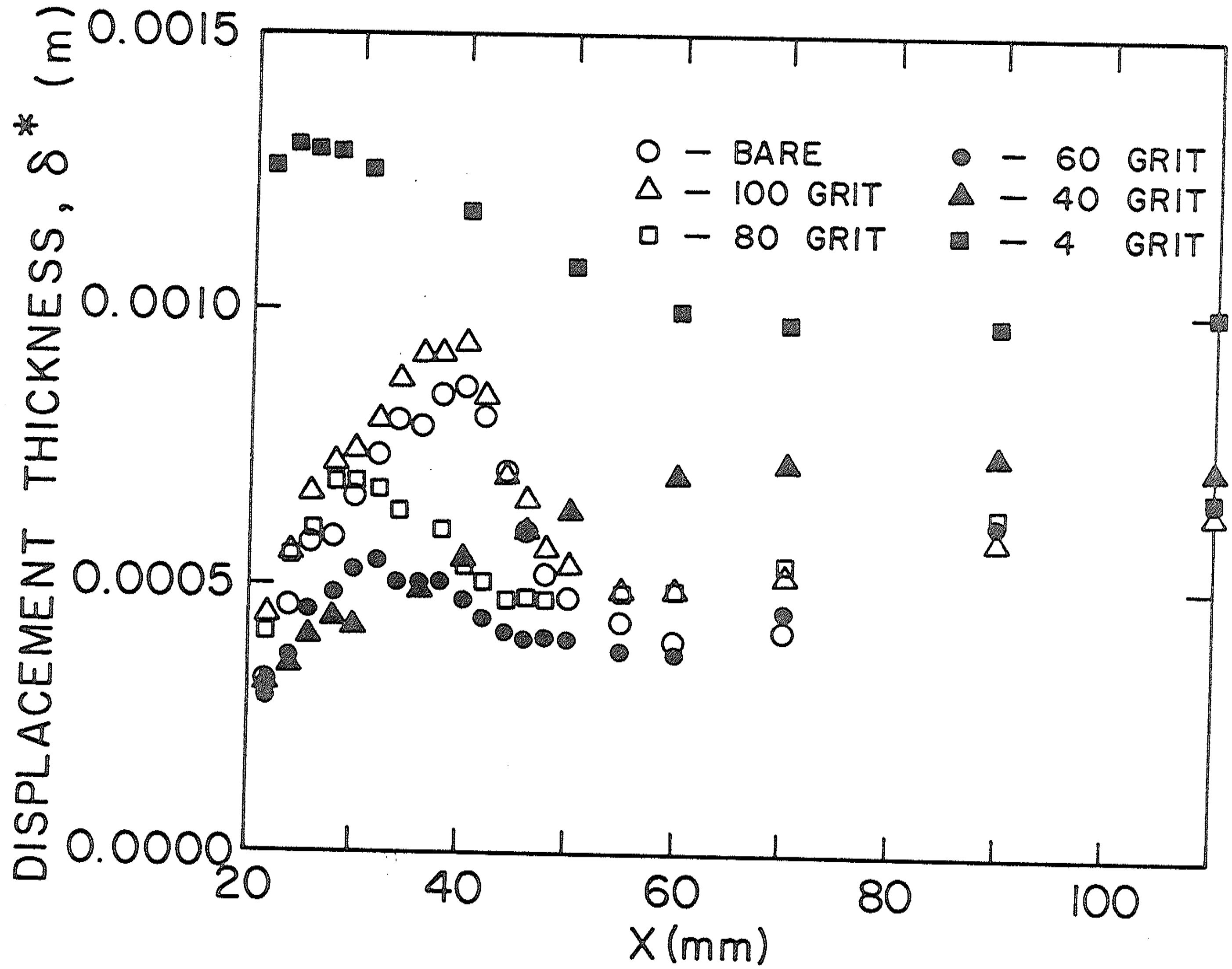

Figure 14: Boundary Layer Development

(a) Development of Displacement Thickness.

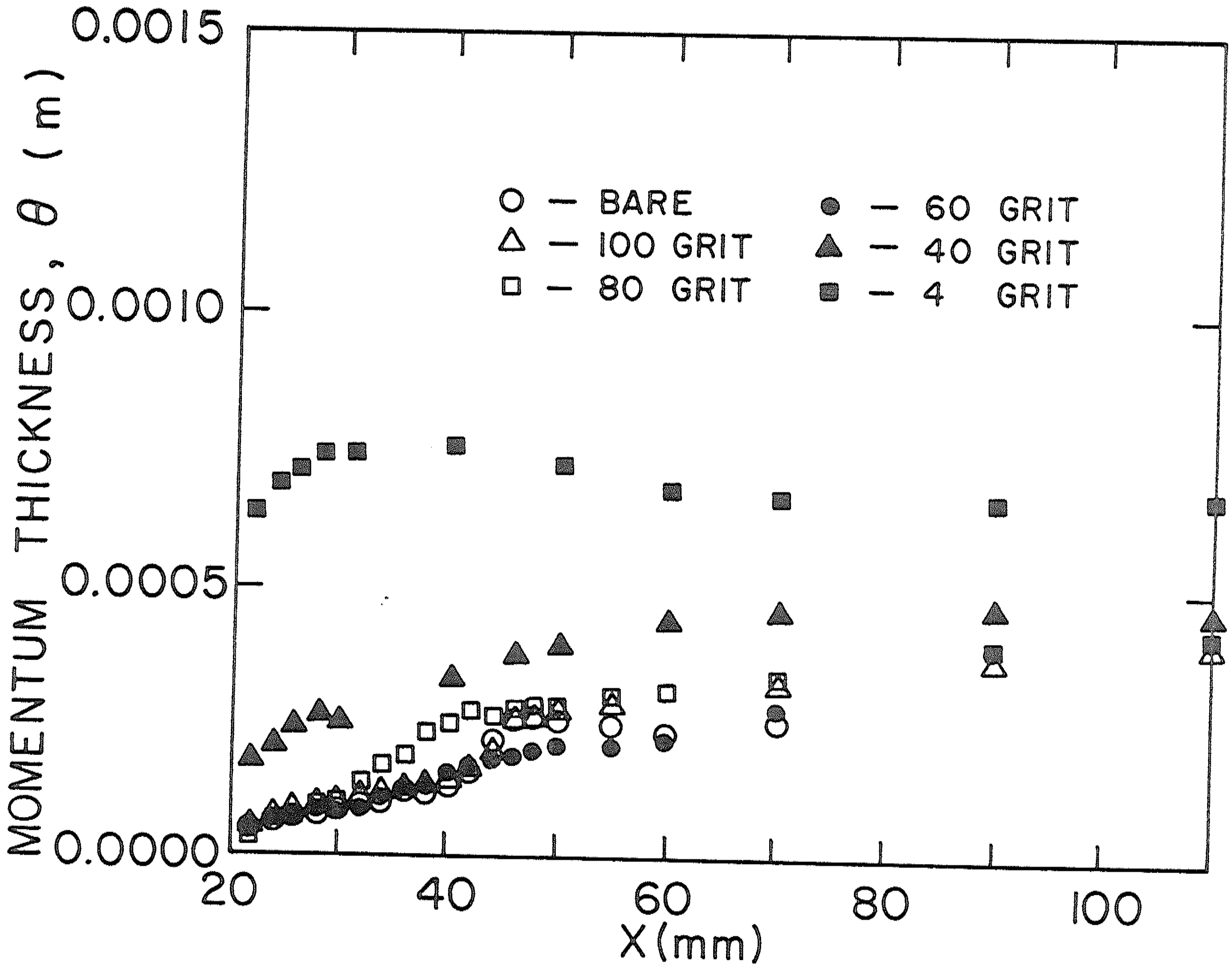

(b) Development of Momentum Thickness.

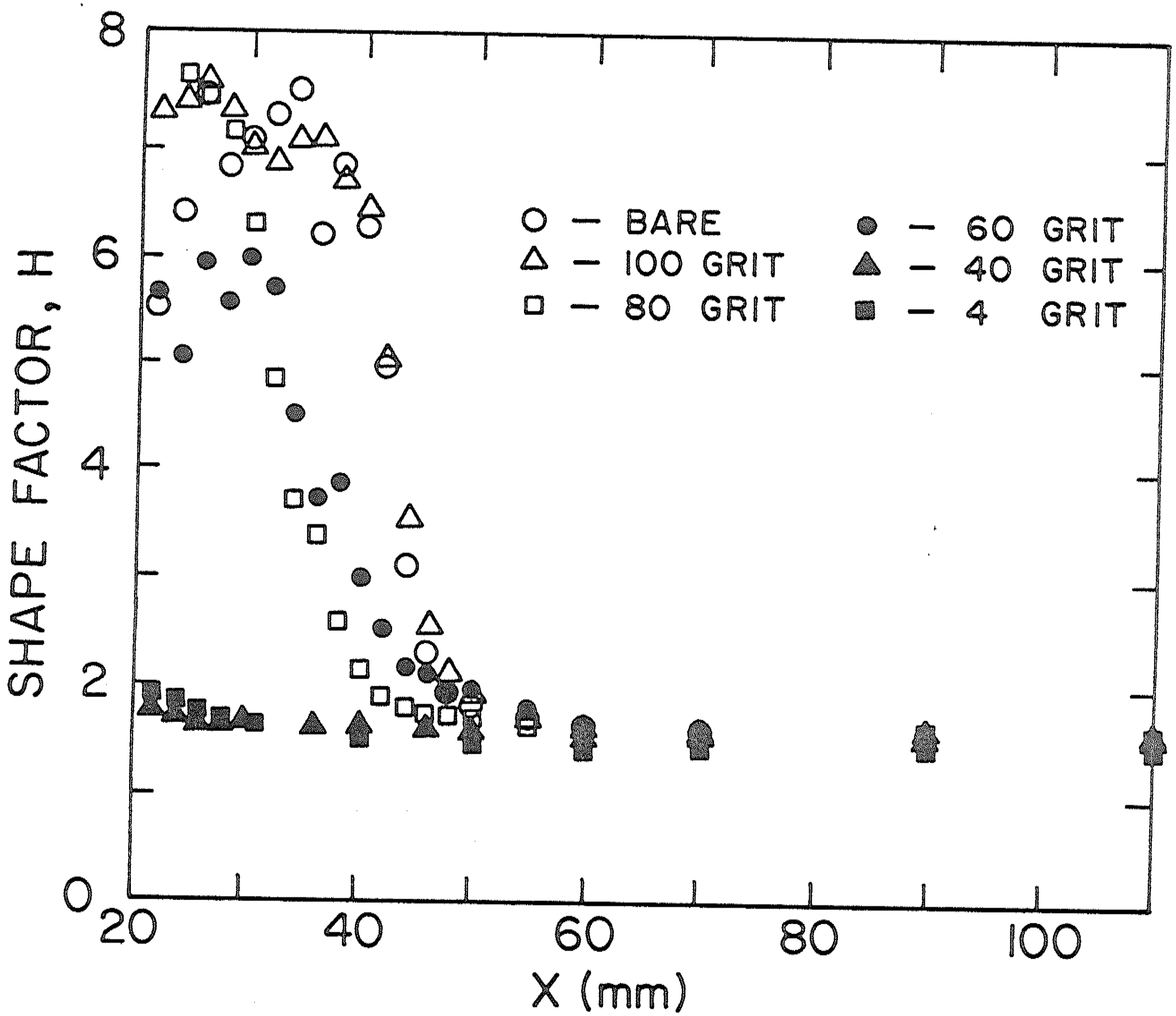

(c) Development of Shape Factor.

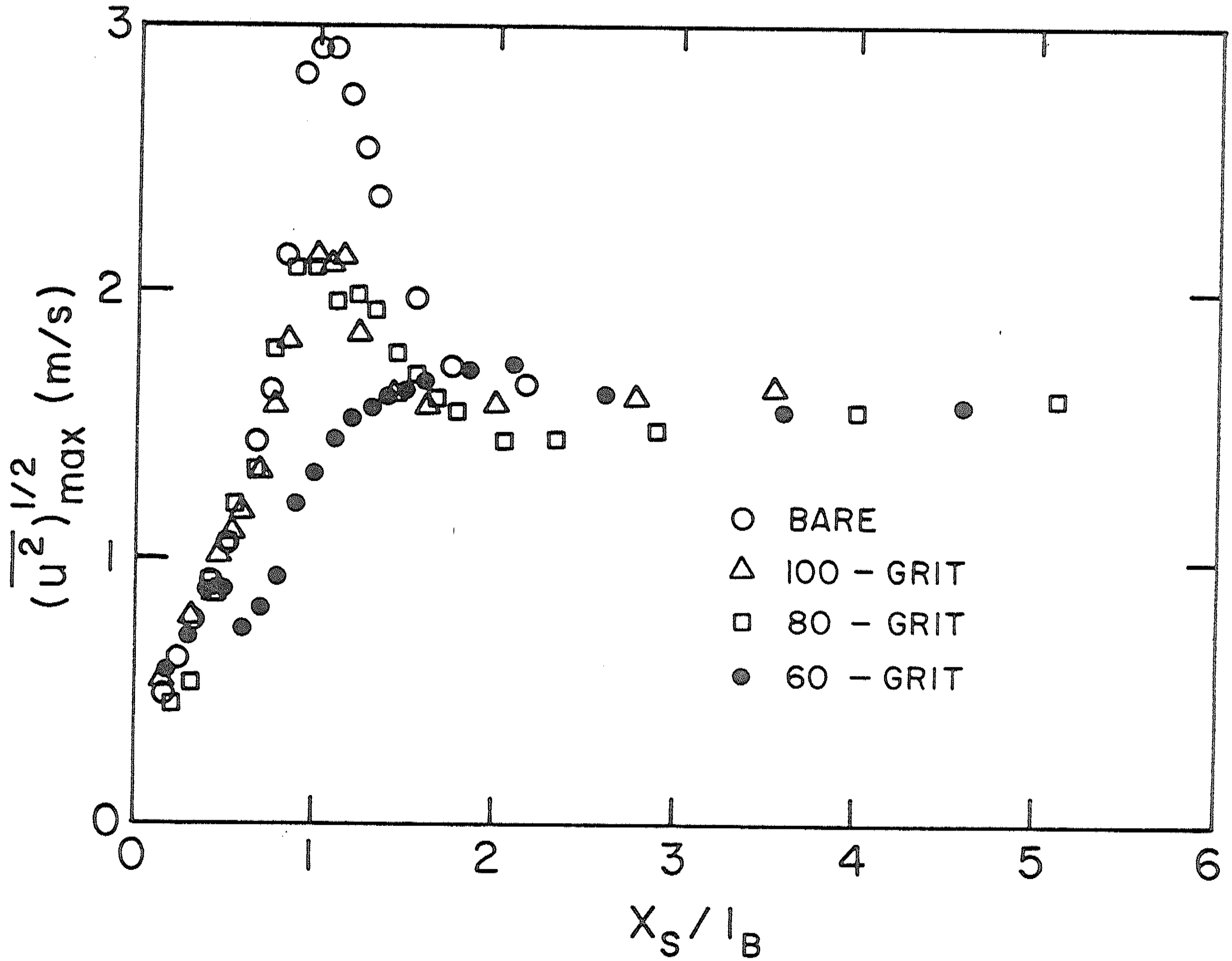

Figure 15: Distribution of RMS Values of Maximum Longitudinal Turbulence Velocity.

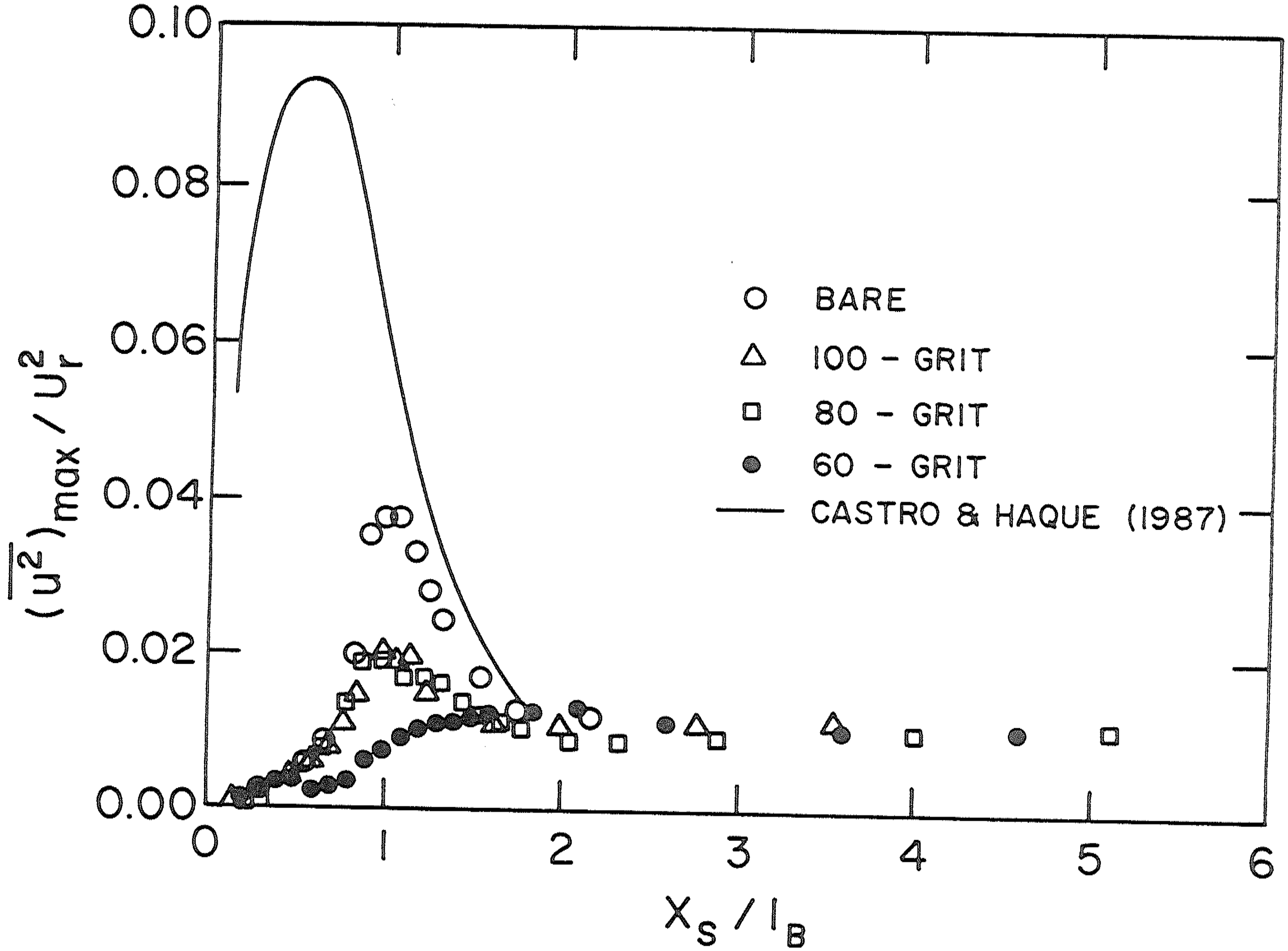

Figure 16: Distribution of Normalized Values of Turbulence.

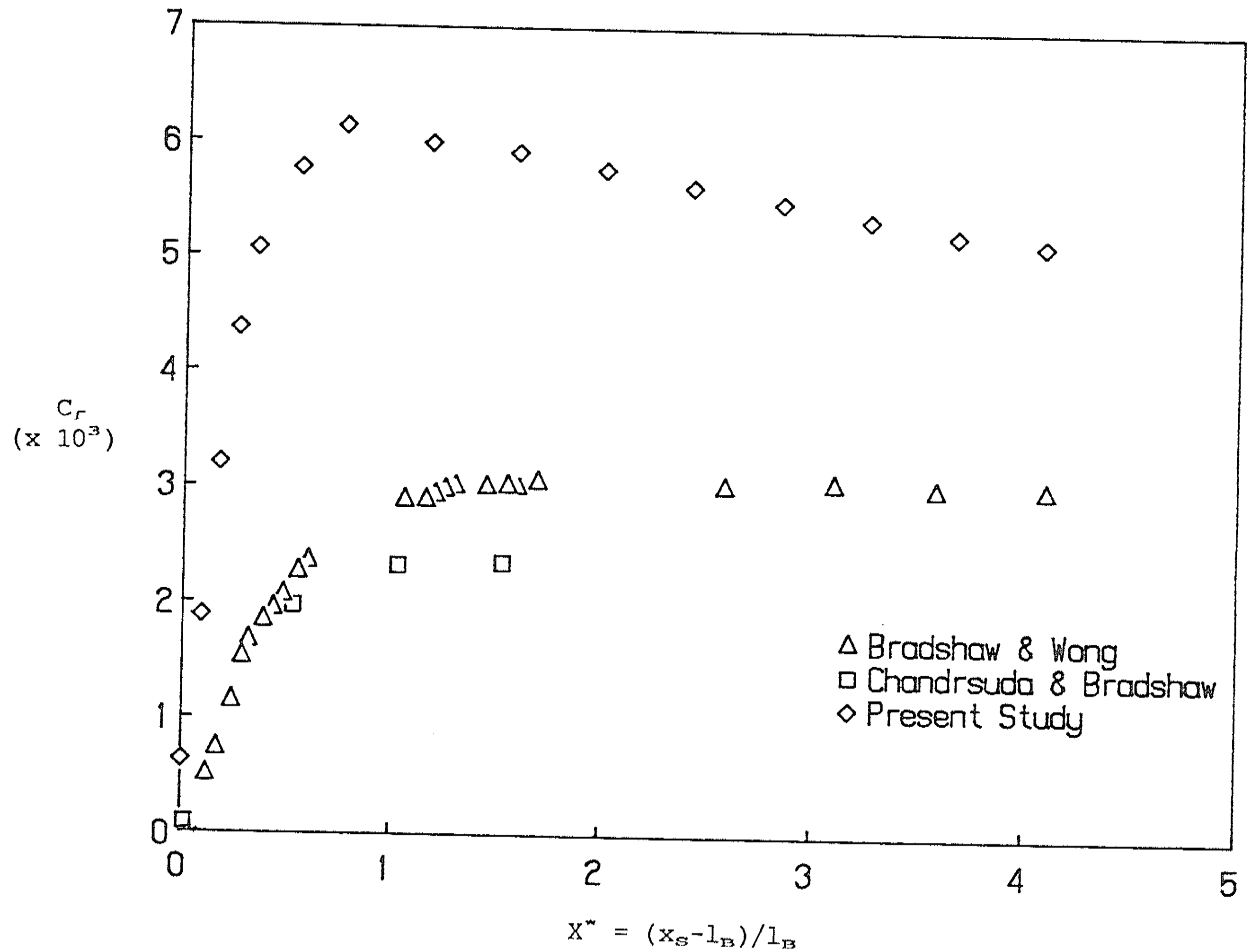

Figure 17: Distribution of Skin Friction Coefficient.

APPENDIX A:

DATA TABLES FOR PLOTS

TABLE A.1: PRESSURE COEFFICIENT DISTRIBUTION

All C_p-values are negative.

x	Bare	100-Grit	80-Grit	60-Grit	40-Grit	4-Grit
22	0.4350	0.4147	0.4339	0.4344	0.4118	0.3619
24	0.4450	0.4290	0.4294	0.4235	0.3641	0.3221
26	0.4190	0.4087	0.4012	0.3937	0.2854	0.2830
28	0.3950	0.3820	0.3778	0.3628	0.2453	0.2541
30	0.3520	0.3487	0.3265	0.2925	0.2183	0.2306
32	0.3400	0.3304	0.2918	0.2431	0.2017	0.2102
34	0.3190	0.3156	0.2571	0.2064	0.1865	0.1960
36	0.3120	0.2973	0.2119	0.1746	0.1736	0.1842
38	0.2900	0.2693	0.1719	0.1436	0.1622	0.1731
40	0.2560	0.2350	0.1402	0.1277	0.1543	0.1628
42	0.1970	0.1708	0.1244	0.1200	0.1466	0.1540
44	0.1370	0.1176	0.1161	0.1162	0.1389	0.1468
46	0.0980	0.0873	0.1101	0.1124	0.1327	0.1390
48	0.0803	0.0760	0.1048	0.1101	0.1265	0.1335
50	0.0742	0.0735	0.1014	0.1063	0.1211	0.1288
55	0.0657	0.0726	0.0938	0.0972	0.1095	
60	0.0680	0.0740	0.0878	0.0911	0.1005	0.1061
70	0.0684	0.0708	0.0786	0.0797	0.0866	0.0913
80		0.0649	0.0692	0.0721	0.0765	0.0811
90		0.0626	0.0632	0.0661	0.0695	0.0733
100		0.0587	0.0594	0.0607	0.0640	0.0683
110		0.0550	0.0564	0.0569	0.0601	0.0636
120		0.0523			0.0554	0.0605
130		0.0501			0.0524	0.0574
140		0.0479			0.0502	0.0551
150		0.0464			0.0479	0.0535
160		0.0449			0.0465	0.0512
170					0.0450	0.0496
180					0.0000	0.0481
190					0.0000	0.0473
200					0.0465	

TABLE A.2(a): MEAN VELOCITY PROFILES FOR BARE CASE

All velocities given in m/s.
Distance from surface (y-value) given in mm.

y	22 mm	24 mm	26 mm	28 mm	30 mm	32 mm	34 mm	36 mm	38 mm
				5 to 10 ms^{-1} Calibration					
0.3	5.97	3.28	1.67	0.83	0.50	0.47	0.41		
0.4	9.17	5.43	3.35	1.97	1.54	1.24	0.60	0.65	0.84
0.5		9.87	6.93	4.86	4.16	3.66	2.54	2.04	1.27
0.6				7.63	6.79	6.05	4.80	4.33	2.93
0.7					9.48	8.66	7.27	7.14	5.71
0.8							9.64	9.54	8.63
				10 to 20 ms^{-1} Calibration					
0.3	6.14	2.16	0.48	0.50	0.18	0.16			
0.4	9.26					0.28	0.22	0.44	
0.5	13.86	8.90	4.90		3.56	2.00	0.84	1.02	0.72
0.6	16.06	12.32	8.40	8.36			2.86	3.50	1.70
0.7	17.18	14.96	11.64	11.24	9.20	6.40	5.44	6.18	3.86
0.8	17.58	16.48	14.30	13.76	11.82	9.22	7.28	8.62	6.86
0.9	17.72	17.22	15.98	15.54	13.84	11.78	10.08	10.86	9.46
1.0	17.72	17.50	16.90	16.62	15.66	13.88	12.32	12.80	11.36
1.0	18.14	18.04	17.56	16.96	16.78	14.22	13.48	12.58	11.96
1.2	18.10	18.04	17.72	17.62	17.60	15.94	15.74	14.92	14.40
1.4	18.08	18.02	17.70	17.68	17.68	16.36	16.32	16.02	15.82
1.6	17.98	17.96	17.66	17.64	17.68	16.40	16.48	16.46	16.50
1.8	17.94	17.92	17.62	17.60	17.64	16.38	16.46	16.50	16.62
2.0	17.90	17.88	17.58	17.56	17.58	16.34	16.42	16.50	16.60
2.2		17.84	17.54	17.52	17.56	16.30	16.40	16.46	16.54
2.4	17.82	17.80	17.52	17.50	17.52	16.28	16.36	16.44	16.48
2.6	17.78	17.76	17.48	17.46	17.48	16.26	16.34	16.40	16.44
3.6	17.60	17.60	17.34	17.34	17.36	16.16	16.24	16.28	16.30

TABLE A.2(a): (cont'd)

Y	40 mm	42 mm	44 mm	46 mm	48 mm	50 mm	55 mm	60 mm	70 mm
				5 to 10 ms^{-1} Calibration					
0.3		2.00	2.88	4.97	6.72	8.34	9.55	9.94	9.79
0.4	1.37	2.11	3.53	5.92	7.70	9.09			
0.5	1.42	2.77	4.49	7.24	8.61				
0.6	2.50	4.09	5.92	8.51	9.73				
0.7	4.45	5.78	7.41	9.73					
0.8	7.11	7.51	8.96						
0.9	9.02	9.44							
				10 to 20 ms^{-1} Calibration					
0.3		1.86	2.44	4.28	6.42	8.08	9.42	9.86	9.98
0.4			2.88			8.98	10.32	10.72	10.74
0.5	1.16	2.24	3.98	6.68	8.70	10.06	11.30	11.64	11.70
0.6	1.90				9.56	10.92	11.92	12.22	12.28
0.7	3.96	5.10		9.36	10.86	11.70	12.48	12.78	12.80
0.8			8.68	10.70	11.62	12.36	12.94	13.26	13.24
0.9	8.78	9.30	10.48	11.96	12.60	12.92	13.34	13.56	13.56
1.0	10.66	11.16	11.84	12.84	13.26	13.46	13.64	13.82	13.76
1.0	11.26	11.66	12.16	13.02	13.12	13.34	13.64	13.36	13.22
1.2	13.96	14.42	14.14	14.26	14.12	14.04	14.20	13.78	13.68
1.4	15.76	15.74	15.24	15.00	14.72	14.54	14.50	14.10	14.04
1.6	16.54	16.30	15.80	15.40	15.10	14.92	14.86	14.36	14.22
1.8	16.70	16.46	15.98	15.58	15.32	15.16	15.08	14.60	14.44
2.0	16.68	16.44	16.02	15.66	15.42	15.32	15.20	14.76	14.66
2.2	16.62	16.42	16.02	15.70	15.48	15.40	15.36	14.88	14.78
2.4	16.58	16.36	15.98	15.70	15.50	15.46	15.42	14.98	14.88
2.6	16.52	16.36	15.98	15.74	15.54	15.50	15.48	15.04	14.94
3.6	16.36	16.24	15.96	15.80	15.64	15.60	15.60	15.18	15.22

TABLE A.2(b): MEAN VELOCITY PROFILES FOR 100-GRIT CASE

y	22 mm	24 mm	26 mm	28 mm	30 mm	32 mm	34 mm	36 mm	38 mm	40 mm
0.3	2.20	0.78	0.20	0.12	0.14	0.12				
0.4	4.32	2.28	0.86	0.50	0.46	0.34	0.20			
0.5	9.30	5.52	2.98	2.20	2.10	1.40	0.48	0.40	0.66	1.04
0.6	12.86	9.18	5.78	4.48	4.30	3.22	1.96	1.02	0.92	1.06
0.7	15.40	12.66	9.16	7.44	6.90	5.62	4.10	3.06	2.94	2.30
0.8	16.78	14.86	12.14	10.58	9.86	8.26	6.54	5.62	5.66	4.80
0.9	17.38	16.44	14.52	13.02	12.34	10.86	9.02	8.04	8.04	7.28
1.0	17.60	17.20	16.20	15.22	14.54	13.16	11.56	10.30	10.10	9.50
1.2	17.64	17.58	17.40	17.16	16.60	16.04	14.98	14.06	13.78	13.40
1.4	17.62	17.56	17.58	17.54	17.18	17.02	16.62	16.32	15.96	15.80
1.6			17.56	17.58	17.26	17.24	17.18	17.06	17.00	16.90
1.8	17.52	17.50		17.52	17.22	17.24	17.22	17.20	17.18	17.12
2.0								17.18		17.12
2.2	17.46	17.42	17.46	17.46	17.16	17.18	17.16	17.16	17.14	17.08
2.4										17.04
2.6	17.38	17.36	17.38	17.40	17.10	17.12	17.12	17.10	17.06	17.02
3.6	17.22	17.22	17.26	17.28	16.98	17.00	16.98	16.96	16.92	16.88

y	42 mm	44 mm	46 mm	48 mm	50 mm	55 mm	60 mm	70 mm	90 mm	110 mm
0.3		2.48	4.38	6.28	7.52	8.22	8.26	8.22	7.66	6.56
0.4	1.74	3.62	5.50	7.40	8.46	9.28	9.46	9.34	8.76	8.08
0.5	1.80	5.16	6.74	8.58	9.30	10.14	10.36	10.22	9.68	9.18
0.6	2.72	6.80	7.96	9.66	10.14	10.90	11.12	11.02	10.34	9.94
0.7	4.44	8.70	9.14	10.60	10.90	11.48	11.70	11.54	11.06	10.48
0.8	6.76	10.32	10.32	11.48	11.54	11.98	12.12	11.96	11.44	10.98
0.9	8.82	11.88	11.42	12.26	12.12	12.38	12.50	12.34	11.80	11.34
1.0	11.16	13.36	12.38	12.90	12.60	12.76	12.82	12.62	12.10	11.64
1.2	14.32	15.06	13.78	14.00	13.44	13.36	13.34	13.14	12.60	12.14
1.4	15.96	15.94	14.64	14.64	14.04	13.82	13.70	13.54	13.02	12.58
1.6	16.70	16.30	15.12	15.08	14.46	14.22	14.08	13.86	13.32	12.90
1.8	16.84	16.36	15.34	15.34	14.82	14.54	14.40	14.16	13.66	13.24
2.0	16.82	16.40	15.44	15.44	15.00	14.82	14.66	14.40	13.96	13.52
2.2	16.80	16.40		15.50	15.12	14.98	14.84	14.62	14.20	13.82
2.4	16.76	16.42		15.52	15.16	15.10	15.02	14.80	14.40	14.06
2.6	16.74	16.44	15.54	15.56	15.20	15.20	15.16	14.96	14.56	14.26
3.6	16.64	16.44	15.62	15.64	15.28	15.30	15.36	15.36	15.20	15.06

TABLE A.2(c): MEAN VELOCITY PROFILES FOR 80-GRIT CASE

Y	22 mm	24 mm	26 mm	28 mm	30 mm	32 mm	34 mm	36 mm	38 mm	40 mm
0.3	0.78	0.68	0.44	0.38	0.62	1.28	2.38	3.62	4.66	6.14
0.4	7.54	2.56	1.84	0.96	1.14	2.22	3.80	5.16	6.26	7.54
0.5	10.60	5.60	4.16	2.48	2.72	3.78	5.38	6.66	7.52	8.72
0.6	14.32	9.34	8.00	4.94	5.34	6.18	7.38	8.28	8.64	10.02
0.7	16.26	12.46	11.18	8.50	8.00	8.40	9.34	9.86	10.10	11.12
0.8	17.16	14.76	13.76	11.52	10.64	10.72	11.22	11.40	11.28	12.24
0.9	17.50	16.24	15.64	13.94	12.94	12.70	12.88	12.84	12.46	13.10
1.0	17.60	16.94	16.64	15.60	14.68	14.36	14.16	13.92	13.44	13.80
1.2	17.58	17.34	17.34	17.10	16.36	16.04	15.72	15.26	14.70	14.86
1.4	17.54	17.38	17.42	17.46	16.74	16.52	16.24	15.82	15.38	15.40
1.6		17.30	17.38	17.46	16.78	16.64	16.40	16.06	15.70	15.80
1.8	17.44	17.24	17.32	17.44	16.78	16.62	16.44	16.18	15.92	16.04
2.0		17.22	17.28	17.38	16.70	16.62	16.44	16.22	16.00	15.96
2.2	17.36	17.18	17.26	17.34	16.68	16.56	16.42	16.22	16.00	16.06
2.4		17.14	17.24	17.30	16.64	16.56	16.40	16.20	16.04	16.12
2.6	17.30	17.10	17.20	17.28	16.62	16.50	16.38	16.20	16.04	16.16
3.6	17.12	16.96	17.06	17.16	16.50	16.44	16.34	16.20	16.06	16.22

Y	42 mm	44 mm	46 mm	48 mm	50 mm	55 mm	60 mm	70 mm	90 mm	110 mm
0.3	6.14	7.20	7.18	7.98	8.06	8.04	7.94	7.94	7.46	7.76
0.4	7.60	8.54	8.52	9.34	9.44	9.24	10.08	9.32	8.80	8.76
0.5	8.78	9.46	9.60	10.24	10.34	10.06	10.70	10.16	9.72	9.60
0.6	9.78	10.26	10.44	10.90	11.06	10.64	11.16	11.10	10.32	10.20
0.7	10.92	11.36	11.16	11.44	11.64	11.10	11.56	11.52	10.78	10.64
0.8	11.86	11.90	11.82	12.16	12.20	11.60	11.92	11.86	11.16	10.98
0.9	12.72	12.56	12.44	12.66	12.70	11.98	12.24	12.16	11.46	11.26
1.0	13.40	13.12	12.98	13.12	13.12	12.38	12.52	12.40	11.74	11.54
1.2	14.44	13.94	13.80	13.82	13.80	13.00	13.00	12.82	12.20	11.96
1.4	15.02	14.48	14.40	14.36	14.36	13.46	13.44	13.22	12.60	12.34
1.6	15.46	14.88	14.80	14.76	14.76	13.86	13.82	13.58	12.94	12.66
1.8	15.74	15.20	15.12	15.10	15.12	14.24	14.18	13.94	13.26	13.02
2.0	15.92	15.38	15.34	15.34	15.36	14.54	14.48	14.22	13.56	13.28
2.2	16.00	15.46	15.48	15.48	15.56	14.76	14.70	14.48	13.86	13.58
2.4	16.06	15.54	15.56	15.58	15.62	14.92	14.86	14.72	14.12	13.82
2.6	16.10	15.56	15.60	15.64	15.70	15.02	14.98	14.88	14.36	14.08
3.6	16.16	15.60	15.66	15.72	15.80	15.18	15.20	15.28	15.12	15.02

TABLE A.2(d): MEAN VELOCITY PROFILES FOR 60-GRIT CASE

y	22 mm	24 mm	26 mm	28 mm	30 mm	32 mm	34 mm	36 mm	38 mm	40 mm
0.3	6.30	4.64	2.10	1.72	0.60	0.68	1.88	2.82	3.98	4.98
0.4	10.40	7.62	5.50	5.00	4.02	3.48	4.86	5.46	5.96	6.54
0.5	13.68	11.50	8.84	8.02	7.46	6.56	8.06	8.28	8.38	8.86
0.6	15.76	14.28	12.08	11.26	10.50	10.02	10.92	10.84	10.72	10.94
0.7	16.86	16.00	15.10	13.82	12.98	12.60	13.16	12.98	12.66	12.76
0.8	17.36	16.88	15.96	15.36	14.96	14.34	14.74	14.38	14.08	13.98
0.9	17.52	17.28	16.86	16.50	16.10	15.74	15.74	15.42	14.98	14.92
1.0	17.54	17.42	17.22	17.04	16.64	16.40	16.30	15.98	15.48	15.40
1.2		17.44	17.36	17.28	17.02	16.84	16.66	16.36	15.84	15.74
1.4	17.48	17.42	17.36	17.32	17.10	16.92	16.72	16.44	15.92	15.84
1.6					17.06			16.46	15.94	
1.8	17.40	17.32	17.28	17.24	17.02	16.86	16.68	16.44	15.94	15.86
2.2	17.32	17.26	17.22	17.18	16.98	16.82	16.66	16.44	15.96	15.88
2.6	17.24	17.20	17.16	17.12	16.92	16.80	16.66	16.44	15.98	15.88
3.6	17.08	17.06	17.02	17.00	16.84	16.72	16.60	16.44	15.98	15.92

y	42 mm	44 mm	46 mm	48 mm	50 mm	55 mm	60 mm	70 mm	90 mm	110 mm
0.3	5.48	5.78	6.48	6.22	6.32	6.70	7.16	8.30	8.16	8.22
0.4	7.22	7.56	7.98	7.80	8.08	8.24	8.48	9.48	9.24	9.32
0.5	9.16	9.28	9.50	9.16	9.40	9.28	9.40	10.18	9.88	9.86
0.6	10.72	10.90	10.96	10.60	10.66	10.34	10.22	10.76	10.48	10.40
0.7	12.64	12.46	12.32	11.88	11.74	11.20	11.02	11.26	10.88	10.78
0.8	13.82	13.62	13.54	12.96	12.84	12.12	11.68	11.68	11.24	11.06
0.9	14.78	14.62	14.46	13.98	13.78	12.92	12.38	12.16	11.54	11.34
1.0	15.30	15.20	15.08	14.72	14.44	13.56	12.98	12.52	11.82	11.60
1.2	15.72	15.70	15.70	15.56	15.28	14.42	13.88	13.24	12.26	12.02
1.4	15.82	15.84	15.88	15.86	15.76	14.94	14.56	13.86	12.72	12.44
1.6		15.88	15.94	15.96	15.88	15.16	14.92	14.34	13.14	12.78
1.8	15.86	15.88	15.94	15.98	15.92	15.26	15.12	14.68	13.50	13.06
2.0			15.94	16.00	15.94	15.30	15.22	14.94	13.86	13.40
2.2	15.86	15.88	15.94	16.02	15.94	15.32	15.28	15.08	14.14	13.70
2.4			15.94	16.02	15.94	15.32	15.30	15.20	14.44	13.98
2.6	15.86	15.88	15.94	16.02	15.94	15.34	15.32	15.28	14.70	14.22
3.6	15.88	15.90	15.94	16.04	15.96	15.34	15.34	15.36	15.32	15.16

TABLE A.2(e): MEAN VELOCITY PROFILES FOR 40-GRIT CASE

Y	22 mm	24 mm	26 mm	28 mm	30 mm	36 mm	40 mm
0.3	9.96	9.42	9.10	9.14	9.58	9.40	8.80
0.4	11.36	10.86	10.58	10.32	10.62	10.30	9.92
0.5	12.08	11.58	11.34	11.06	11.18	10.80	10.46
0.6	12.72	12.22	11.96	11.72	11.68	11.30	10.94
0.7	13.28	12.86	12.48	12.18	12.20	11.68	11.40
0.8	13.82	13.36	12.96	12.64	12.62	12.08	11.72
0.9	14.36	13.88	13.44	13.06	13.00	12.42	12.08
1.0	14.86	14.40	13.90	13.46	13.38	12.76	12.38
1.2	15.64	15.28	14.78	14.38	14.08	13.42	12.96
1.4	16.14	15.92	15.50	15.12	14.76	14.02	13.58
1.6	16.52	16.44	16.08	15.76	15.26	14.56	14.08
1.8	16.76	16.74	16.42	16.24	15.72	15.04	14.58
2.0	16.84	16.88	16.70	16.54	16.02	15.42	15.04
2.2	16.86	16.92	16.80	16.68	16.20	15.74	15.42
2.4	16.84	16.92	16.84	16.74	16.28	15.92	15.70
2.6	16.80	16.90	16.84	16.76	16.32	16.04	15.86
3.6	16.66	16.78	16.78	16.74	16.32	16.12	16.08
4.6					16.28	16.10	16.06
5.6					16.24	16.08	16.04

Y	46 mm	50 mm	60 mm	70 mm	90 mm	110 mm
0.3	8.66	8.52	7.88	8.06	7.26	7.12
0.4	9.82	9.50	9.12	9.16	8.50	8.38
0.5	10.34	10.12	9.80	9.76	9.16	9.06
0.6	10.80	10.52	10.20	10.16	9.68	9.52
0.7	11.22	10.90	10.56	10.48	10.02	9.92
0.8	11.54	11.20	10.90	10.80	10.38	10.26
0.9	11.84	11.52	11.18	11.06	10.62	10.50
1.0	12.12	11.78	11.42	11.28	10.84	10.72
1.2	12.64	12.26	11.90	11.72	11.22	11.12
1.4	13.18	12.76	12.34	12.10	11.62	11.44
1.6	13.64	13.22	12.74	12.46	11.94	11.76
1.8	14.14	13.66	13.14	12.82	12.26	12.04
2.0	14.56	14.08	13.50	13.16	12.56	12.32
2.2	14.94	14.42	13.82	13.46	12.86	12.58
2.4	15.32	14.80	14.18	13.84	13.14	12.86
2.6	15.58	15.06	14.50	14.14	13.42	13.12
3.6	16.02	15.60	15.42	15.26	14.66	14.30
4.6	16.00					
5.6	15.98					

TABLE A.2(f): MEAN VELOCITY PROFILES FOR 4-GRIT CASE

Y	22 mm	24 mm	26 mm	28 mm	31 mm	40 mm
0.3	7.72	7.66	8.40	8.56	8.90	9.00
0.4	8.62	8.74	9.54	9.74	9.92	10.22
0.5	8.96	9.30	10.04	10.30	10.40	10.92
0.6	9.06	9.54	10.20	10.54	10.58	11.28
0.7	9.10	9.66	10.32	10.72	10.70	11.48
0.8	8.90	9.52	10.12	10.58	10.64	11.64
0.9	8.78	9.36	10.04	10.48	10.54	11.64
1.0	8.66	9.26	9.90	10.36	10.40	11.58
1.2	8.62	9.16	9.76	10.24	10.32	11.46
1.4	8.82	9.22	9.78	10.22	10.28	11.48
1.6	9.22	9.40	9.84	10.24	10.24	11.44
1.8	9.78	9.72	10.06	10.30	10.26	11.36
2.0	10.48	10.20	10.34	10.48	10.32	11.28
2.2	11.46	10.98	10.96	10.96	10.66	11.30
2.4	12.52	11.86	11.72	11.60	11.14	11.56
2.6	13.62	12.80	12.46	12.20	11.58	11.82
2.8	14.60	13.68	13.24	12.86		
3.0	15.38	14.48	13.98	13.52		
3.2	16.08	15.32	14.82	14.34		
3.4	16.56	15.98	15.52	15.06		
3.6	16.84	16.42	16.06	15.66	14.50	13.46
4.6	17.02	17.00	16.96	16.78	16.04	15.24
5.6	16.92	16.90	16.92	16.86	16.18	15.86
6.6					16.14	15.88

TABLE 5(f): (cont'd)

Y	50 mm	60 mm	70 mm	90 mm	110 mm
0.3	9.04	9.60	8.58	8.16	7.62
0.4	10.40	10.68	10.22	9.60	9.22
0.5	11.12	11.32	11.02	10.50	10.16
0.6	11.60	11.70	11.52	11.08	10.78
0.7	11.86	12.02	11.84	11.46	11.22
0.8	12.06	12.22	12.12	11.80	11.52
0.9	12.12	12.34	12.30	12.04	11.80
1.0	12.18	12.40	12.44	12.24	12.02
1.2	12.28	12.60	12.68	12.54	12.36
1.4	12.36	12.74	12.88	12.80	12.66
1.6	12.32	12.78	12.98	13.00	12.90
1.8	12.26	12.74	13.04	13.14	13.08
2.0	12.18	12.72	13.02	13.24	13.22
2.2	12.24	12.76	13.08	13.34	13.32
2.4	12.36	12.86	13.16	13.44	13.46
2.6	12.44	12.92	13.26	13.52	13.60
3.6	13.36	13.56	13.70	13.96	14.08
4.6	14.70	14.52	14.46	14.48	14.54
5.6	15.56	15.34	15.18	15.00	14.98
6.6	15.74	15.66	15.56	15.40	15.34
7.6	15.74	15.68	15.64	15.58	15.56
8.6				15.60	15.62

TABLE A.3(a): TURBULENCE INTENSITY PROFILES FOR BARE CASE

All turbulence intensities, $(\overline{u^2})^{1/2}$, normalized by $\overline{U}_r$.
All distances from surface (y-values) in mm.

y	22 mm	24 mm	26 mm	28 mm	30 mm	32 mm	34 mm	36 mm	38 mm
					5 to 10 ms^{-1} Calibration				
0.3	0.0265	0.0246	0.0233	0.0165	0.0121	0.0123	0.0086		
0.4	0.0292	0.0329	0.0338	0.0294	0.0319	0.0347	0.0176	0.0267	0.0326
0.5		0.0362	0.0459	0.0433	0.0478	0.0531	0.0589	0.0834	0.0570
0.6				0.0509	0.0551	0.0597	0.0771	0.1163	0.1323
0.7					0.0553	0.0615	0.0836	0.1146	0.1574
0.8							0.0815	0.1045	0.1376
					10 to 20 ms^{-1} Calibration				
0.3	0.0299	0.0232	0.0104	0.0073	0.0053	0.0031			
0.4	0.0325					0.0102	0.0069	0.0174	
0.5	0.0257	0.0420	0.0443	0.0000	0.0512	0.0411	0.0347	0.0410	
0.6	0.0151	0.0421	0.0527	0.0613	0.0000	0.0000	0.0760	0.1040	0.0311
0.7	0.0069	0.0268	0.0476	0.0561	0.0699	0.0767	0.0907	0.1095	0.0924
0.8	0.0041	0.0152	0.0337	0.0459	0.0631	0.0804	0.0961	0.1048	0.1313
0.9	0.0037	0.0068	0.0213	0.0306	0.0551	0.0712	0.0960	0.1004	0.1313
1.0	0.0038	0.0039	0.0096	0.0163	0.0334	0.0600	0.0851	0.0944	0.1180
1.0	0.0039	0.0039	0.0047	0.0151	0.0215	0.0479	0.0677	0.0923	0.1179
1.2	0.0039	0.0041	0.0043	0.0045	0.0051	0.0157	0.0255	0.0669	0.1428
1.4	0.0038	0.0041	0.0045	0.0047	0.0050	0.0049	0.0125	0.0376	0.0936
1.6	0.0038	0.0040	0.0044	0.0048	0.0052	0.0051	0.0058	0.0088	0.0551
1.8	0.0038	0.0040	0.0043	0.0047	0.0050	0.0053	0.0065	0.0084	0.0180
2.0	0.0038	0.0039	0.0043	0.0047	0.0051	0.0052	0.0066	0.0087	0.0143
2.2		0.0040	0.0042	0.0046	0.0049	0.0050	0.0062	0.0085	0.0125
2.4	0.0037	0.0039	0.0041	0.0046	0.0049	0.0051	0.0062	0.0082	0.0116
2.6	0.0037	0.0039	0.0040	0.0045	0.0048	0.0050	0.0060	0.0079	0.0112
3.6	0.0037	0.0037	0.0038	0.0044	0.0047	0.0047	0.0055	0.0066	0.0104

TABLE A.3(a): (cont'd)

y	40 mm	42 mm	44 mm	46 mm	48 mm	50 mm	55 mm	60 mm	70 mm
					5 to 10 ms^{-1} Calibration				
0.3		0.0763	0.1131	0.1485	0.1470	0.1348	0.1129	0.1013	0.0988
0.4	0.0534	0.0864	0.1310	0.1586	0.1500	0.1359			
0.5	0.0585	0.1188	0.1553	0.1671	0.1542				
0.6	0.1230	0.1595	0.1753	0.1698	0.1555				
0.7	0.1700	0.1812	0.1820	0.1641					
0.8	0.1770	0.1850	0.1782						
0.9	0.1605	0.1685							
					10 to 20 ms^{-1} Calibration				
0.3		0.0747	0.1029	0.1470	0.1576	0.1496	0.1268	0.1151	0.1107
0.4			0.1195			0.1500	0.1260	0.1136	0.1065
0.5	0.0545	0.1049	0.1529	0.1757	0.1685	0.1538	0.1287	0.1127	0.1024
0.6	0.0995				0.1690	0.1576	0.1297	0.1135	0.0997
0.7	0.1715	0.1862		0.1833	0.1673	0.1559	0.1323	0.1139	0.0979
0.8			0.1947	0.1770	0.1626	0.1525	0.1309	0.1139	0.0968
0.9	0.1883	0.1951	0.1858	0.1622	0.1513	0.1470	0.1287	0.1136	0.0960
1.0	0.1711	0.1778	0.1685	0.1513	0.1399	0.1348	0.1249	0.1127	0.0955
1.0	0.1690	0.1698	0.1622	0.1428	0.1382	0.1331	0.1193	0.1075	0.0925
1.2	0.1235	0.1100	0.1120	0.1049	0.1058	0.1095	0.1076	0.1027	0.0892
1.4	0.0643	0.0669	0.0807	0.0793	0.0853	0.0929	0.0992	0.0929	0.0847
1.6	0.0307	0.0452	0.0596	0.0616	0.0679	0.0731	0.0819	0.0840	0.0807
1.8	0.0242	0.0368	0.0496	0.0511	0.0528	0.0588	0.0711	0.0737	0.0748
2.0	0.0222	0.0330	0.0435	0.0440	0.0467	0.0489	0.0589	0.0641	0.0687
2.2	0.0194	0.0292	0.0367	0.0369	0.0375	0.0395	0.0480	0.0564	0.0625
2.4	0.0174	0.0259	0.0324	0.0340	0.0340	0.0338	0.0360	0.0485	0.0564
2.6	0.0153	0.0228	0.0281	0.0296	0.0300	0.0308	0.0330	0.0404	0.0521
3.6	0.0098	0.0137	0.0157	0.0159	0.0169	0.0168	0.0180	0.0201	0.0276

TABLE A.3(b): TURBULENCE INTENSITY PROFILES FOR 100-GRIT CASE

Y	22 mm	24 mm	26 mm	28 mm	30 mm	32 mm	34 mm	36 mm	38 mm	40 mm
0.3	0.0129	0.0097	0.0032	0.0020	0.0023	0.0016				
0.4	0.0243	0.0234	0.0152	0.0110	0.0109	0.0099	0.0051			
0.5	0.0355	0.0344	0.0314	0.0313	0.0327	0.0319	0.0206	0.0148	0.0256	0.0453
0.6	0.0286	0.0386	0.0401	0.0404	0.0421	0.0412	0.0417	0.0404	0.0385	0.0497
0.7	0.0188	0.0339	0.0525	0.0595	0.0676	0.0651	0.0701	0.0849	0.0999	0.0912
0.8	0.0101	0.0244	0.0456	0.0563	0.0609	0.0735	0.0753	0.0889	0.1056	0.1215
0.9	0.0052	0.0144	0.0323	0.0489	0.0548	0.0679	0.0789	0.0885	0.1037	0.1192
1.0	0.0037	0.0071	0.0200	0.0328	0.0412	0.0581	0.0735	0.0892	0.1031	0.1117
1.2	0.0037	0.0038	0.0049	0.0096	0.0152	0.0269	0.0487	0.0715	0.0791	0.0857
1.4	0.0037	0.0038	0.0040	0.0043	0.0044	0.0074	0.0172	0.0274	0.0384	0.0469
1.6			0.0041	0.0046	0.0047	0.0047	0.0050	0.0075	0.0110	0.0233
1.8	0.0037	0.0037		0.0045	0.0047	0.0050	0.0057	0.0067	0.0106	0.0207
2.0								0.0072		0.0181
2.2	0.0036	0.0038	0.0039	0.0044	0.0045	0.0051	0.0057	0.0070	0.0091	0.0153
2.4										0.0131
2.6	0.0035	0.0037	0.0038	0.0043	0.0045	0.0048	0.0054	0.0063	0.0077	0.0111
3.6	0.0035	0.0036	0.0037	0.0039	0.0042	0.0046	0.0048	0.0053	0.0058	0.0069

Y	42 mm	44 mm	46 mm	48 mm	50 mm	55 mm	60 mm	70 mm	90 mm	110 mm
0.3		0.0973	0.1310	0.1316	0.1217	0.1089	0.1047	0.1051	0.1072	0.1055
0.4	0.0681	0.1176	0.1327	0.1304	0.1205	0.1084	0.1039	0.1029	0.1067	0.1095
0.5	0.0712	0.1331	0.1357	0.1321	0.1193	0.1068	0.1020	0.0995	0.1028	0.1064
0.6	0.0999	0.1420	0.1382	0.1424	0.1211	0.1061	0.0993	0.0945	0.0983	0.1016
0.7	0.1263	0.1437	0.1403	0.1348	0.1227	0.1073	0.0980	0.0912	0.0911	0.0955
0.8	0.1382	0.1382	0.1399	0.1348	0.1236	0.1080	0.0980	0.0885	0.0872	0.0899
0.9	0.1315	0.1268	0.1344	0.1304	0.1224	0.1084	0.0981	0.0869	0.0837	0.0857
1.0	0.1183	0.1108	0.1263	0.1243	0.1187	0.1079	0.0976	0.0855	0.0812	0.0821
1.2	0.0825	0.0816	0.1031	0.1040	0.1071	0.1037	0.0952	0.0833	0.0775	0.0773
1.4	0.0533	0.0591	0.0761	0.0809	0.0911	0.0953	0.0912	0.0807	0.0743	0.0743
1.6	0.0399	0.0485	0.0565	0.0612	0.0733	0.0833	0.0840	0.0777	0.0723	0.0715
1.8	0.0350	0.0416	0.0456	0.0463	0.0563	0.0719	0.0759	0.0740	0.0695	0.0693
2.0	0.0298	0.0344	0.0368	0.0369	0.0440	0.0580	0.0667	0.0693	0.0668	0.0668
2.2	0.0243	0.0288		0.0314	0.0352	0.0477	0.0579	0.0628	0.0631	0.0635
2.4	0.0208	0.0246		0.0269	0.0301	0.0367	0.0487	0.0569	0.0595	0.0607
2.6	0.0166	0.0205	0.0231	0.0235	0.0252	0.0307	0.0375	0.0507	0.0565	0.0580
3.6	0.0085	0.0102	0.0114	0.0116	0.0131	0.0149	0.0171	0.0232	0.0345	0.0417

TABLE A.3(c): TURBULENCE INTENSITY PROFILES FOR 80-GRIT CASE

y	22 mm	24 mm	26 mm	28 mm	30 mm	32 mm	34 mm	36 mm	38 mm	40 mm
0.3	0.0240	0.0190	0.0226	0.0302	0.0468	0.0785	0.1115	0.1289	0.1212	0.1241
0.4	0.0300	0.0365	0.0389	0.0616	0.0665	0.1045	0.1348	0.1399	0.1289	0.1280
0.5	0.0307	0.0496	0.0543	0.0749	0.0792	0.1192	0.1395	0.1399	0.1313	0.1291
0.6	0.0228	0.0476	0.0575	0.0800	0.0852	0.1155	0.1340	0.1378	0.1310	0.1317
0.7	0.0133	0.0377	0.0523	0.0784	0.0888	0.1143	0.1308	0.1352	0.1310	0.1327
0.8	0.0067	0.0282	0.0420	0.0696	0.0839	0.1083	0.1235	0.1293	0.1302	0.1313
0.9	0.0043	0.0190	0.0287	0.0555	0.0719	0.0961	0.1109	0.1193	0.1261	0.1280
1.0	0.0039	0.0117	0.0202	0.0424	0.0528	0.0763	0.0952	0.1067	0.1176	0.1219
1.2	0.0039	0.0064	0.0099	0.0226	0.0233	0.0405	0.0617	0.0792	0.0976	0.1047
1.4	0.0039	0.0056	0.0074	0.0136	0.0158	0.0251	0.0407	0.0581	0.0761	0.0848
1.6		0.0051	0.0068	0.0101	0.0120	0.0166	0.0236	0.0333	0.0532	0.0601
1.8	0.0037	0.0047	0.0061	0.0085	0.0106	0.0137	0.0171	0.0228	0.0316	0.0404
2.0		0.0046	0.0056	0.0076	0.0094	0.0119	0.0146	0.0169	0.0223	0.0277
2.2	0.0036	0.0043	0.0053	0.0070	0.0085	0.0107	0.0125	0.0142	0.0171	0.0205
2.4		0.0042	0.0050	0.0065	0.0078	0.0097	0.0114	0.0122	0.0144	0.0165
2.6	0.0035	0.0041	0.0049	0.0062	0.0071	0.0086	0.0103	0.0110	0.0117	0.0138
3.6	0.0034	0.0037	0.0040	0.0047	0.0052	0.0059	0.0067	0.0070	0.0075	0.0080

y	42 mm	44 mm	46 mm	48 mm	50 mm	55 mm	60 mm	70 mm	90 mm	110 mm
0.3	0.1175	0.1084	0.1047	0.1027	0.1016	0.0960	0.0963	0.0989	0.1037	0.1068
0.4	0.1223	0.1108	0.1061	0.1025	0.1008	0.0925	0.0880	0.0945	0.1013	0.1044
0.5	0.1240	0.1131	0.1071	0.1031	0.1001	0.0892	0.0844	0.0887	0.0944	0.0989
0.6	0.1259	0.1151	0.1088	0.1040	0.1007	0.0868	0.0819	0.0805	0.0877	0.0917
0.7	0.1284	0.1175	0.1108	0.1053	0.1020	0.0855	0.0805	0.0769	0.0832	0.0860
0.8	0.1293	0.1189	0.1129	0.1071	0.1031	0.0853	0.0796	0.0747	0.0791	0.0821
0.9	0.1280	0.1176	0.1131	0.1075	0.1035	0.0852	0.0788	0.0732	0.0759	0.0787
1.0	0.1241	0.1145	0.1113	0.1060	0.1028	0.0845	0.0776	0.0717	0.0733	0.0757
1.2	0.1095	0.1049	0.1037	0.1005	0.0981	0.0820	0.0757	0.0696	0.0695	0.0719
1.4	0.0933	0.0901	0.0903	0.0891	0.0889	0.0780	0.0725	0.0675	0.0664	0.0685
1.6	0.0737	0.0737	0.0757	0.0772	0.0780	0.0725	0.0680	0.0644	0.0637	0.0657
1.8	0.0527	0.0547	0.0612	0.0628	0.0663	0.0640	0.0609	0.0599	0.0609	0.0632
2.0	0.0342	0.0384	0.0463	0.0487	0.0527	0.0539	0.0528	0.0549	0.0580	0.0603
2.2	0.0257	0.0296	0.0335	0.0366	0.0405	0.0451	0.0457	0.0499	0.0549	0.0577
2.4	0.0197	0.0222	0.0257	0.0280	0.0325	0.0355	0.0369	0.0441	0.0520	0.0552
2.6	0.0162	0.0177	0.0200	0.0218	0.0246	0.0285	0.0305	0.0374	0.0487	0.0525
3.6	0.0087	0.0088	0.0090	0.0092	0.0097	0.0093	0.0101	0.0140	0.0250	0.0338

TABLE A.3(d): TURBULENCE INTENSITY PROFILES FOR 60-GRIT CASE

y	22 mm	24 mm	26 mm	28 mm	30 mm	32 mm	34 mm	36 mm	38 mm	40 mm
0.3	0.0286	0.0284	0.0296	0.0343	0.0184	0.0236	0.0581	0.0776	0.0817	0.0865
0.4	0.0394	0.0469	0.0537	0.0516	0.0488	0.0547	0.0623	0.0800	0.0859	0.0928
0.5	0.0323	0.0476	0.0589	0.0592	0.0463	0.0525	0.0599	0.0792	0.0883	0.0965
0.6	0.0194	0.0331	0.0504	0.0551	0.0386	0.0481	0.0519	0.0700	0.0793	0.0904
0.7	0.0102	0.0204	0.0229	0.0439	0.0341	0.0367	0.0405	0.0537	0.0624	0.0735
0.8	0.0060	0.0100	0.0225	0.0307	0.0242	0.0288	0.0271	0.0349	0.0441	0.0556
0.9	0.0041	0.0061	0.0103	0.0174	0.0159	0.0182	0.0187	0.0228	0.0251	0.0308
1.0	0.0041	0.0046	0.0061	0.0081	0.0095	0.0102	0.0143	0.0163	0.0180	0.0214
1.2		0.0041	0.0044	0.0047	0.0057	0.0070	0.0080	0.0096	0.0096	0.0134
1.4	0.0039	0.0041	0.0045	0.0046	0.0051	0.0059	0.0072	0.0083	0.0083	0.0089
1.6					0.0050			0.0073	0.0071	
1.8	0.0040	0.0041	0.0042	0.0044	0.0048	0.0052	0.0058	0.0063	0.0063	0.0066
2.2	0.0039	0.0039	0.0041	0.0042	0.0046	0.0048	0.0050	0.0053	0.0052	0.0053
2.6	0.0038	0.0039	0.0039	0.0041	0.0043	0.0044	0.0045	0.0046	0.0046	0.0047
3.6	0.0037	0.0037	0.0038	0.0039	0.0040	0.0039	0.0040	0.0039	0.0038	0.0039

y	42 mm	44 mm	46 mm	48 mm	50 mm	55 mm	60 mm	70 mm	90 mm	110 mm
0.3	0.0909	0.0959	0.1041	0.1077	0.1119	0.1140	0.1155	0.1084	0.1043	0.1055
0.4	0.0975	0.1007	0.1048	0.1080	0.1107	0.1100	0.1121	0.1044	0.0991	0.0987
0.5	0.1019	0.1048	0.1076	0.1091	0.1100	0.1080	0.1085	0.0999	0.0933	0.0932
0.6	0.1008	0.1040	0.1073	0.1095	0.1093	0.1049	0.1053	0.0961	0.0867	0.0863
0.7	0.0849	0.0955	0.1031	0.1076	0.1077	0.1028	0.1025	0.0925	0.0827	0.0821
0.8	0.0689	0.0828	0.0916	0.1025	0.1032	0.0991	0.1001	0.0897	0.0792	0.0785
0.9	0.0484	0.0636	0.0764	0.0907	0.0940	0.0929	0.0957	0.0871	0.0763	0.0752
1.0	0.0293	0.0464	0.0601	0.0757	0.0845	0.0845	0.0908	0.0851	0.0743	0.0729
1.2	0.0173	0.0228	0.0319	0.0495	0.0632	0.0699	0.0796	0.0805	0.0716	0.0693
1.4	0.0098	0.0151	0.0202	0.0260	0.0341	0.0492	0.0652	0.0741	0.0692	0.0665
1.6		0.0093	0.0107	0.0177	0.0230	0.0316	0.0493	0.0649	0.0665	0.0641
1.8	0.0073	0.0081	0.0089	0.0104	0.0161	0.0225	0.0350	0.0544	0.0631	0.0615
2.0			0.0078	0.0087	0.0102	0.0157	0.0255	0.0444	0.0593	0.0593
2.2	0.0058	0.0063	0.0070	0.0076	0.0089	0.0105	0.0195	0.0341	0.0557	0.0569
2.4			0.0062	0.0068	0.0074	0.0087	0.0117	0.0270	0.0503	0.0541
2.6	0.0050	0.0052	0.0056	0.0061	0.0067	0.0075	0.0098	0.0204	0.0445	0.0512
3.6	0.0040	0.0042	0.0043	0.0046	0.0047	0.0048	0.0055	0.0071	0.0158	0.0283

TABLE A.3(e): TURBULENCE INTENSITY PROFILES FOR 40-GRIT CASE

Y	22 mm	24 mm	26 mm	28 mm	30 mm	36 mm	40 mm
0.3	0.0807	0.0888	0.0929	0.0943	0.0908	0.0909	0.0947
0.4	0.0733	0.0803	0.0853	0.0883	0.0847	0.0855	0.0887
0.5	0.0692	0.0755	0.0799	0.0829	0.0804	0.0816	0.0845
0.6	0.0669	0.0720	0.0753	0.0781	0.0763	0.0776	0.0807
0.7	0.0663	0.0697	0.0724	0.0755	0.0725	0.0752	0.0772
0.8	0.0659	0.0689	0.0705	0.0733	0.0696	0.0727	0.0749
0.9	0.0653	0.0677	0.0687	0.0719	0.0668	0.0707	0.0727
1.0	0.0636	0.0656	0.0665	0.0703	0.0641	0.0687	0.0709
1.2	0.0567	0.0600	0.0604	0.0633	0.0587	0.0644	0.0684
1.4	0.0476	0.0511	0.0528	0.0556	0.0521	0.0589	0.0635
1.6	0.0355	0.0397	0.0440	0.0477	0.0457	0.0533	0.0588
1.8	0.0242	0.0288	0.0343	0.0372	0.0361	0.0467	0.0539
2.0	0.0161	0.0195	0.0236	0.0269	0.0273	0.0382	0.0471
2.2	0.0113	0.0139	0.0168	0.0193	0.0204	0.0290	0.0386
2.4	0.0092	0.0106	0.0124	0.0147	0.0153	0.0220	0.0295
2.6	0.0075	0.0085	0.0099	0.0110	0.0119	0.0161	0.0225
3.6	0.0045	0.0045	0.0048	0.0052	0.0055	0.0065	0.0076
4.6					0.0039	0.0042	0.0046
5.6					0.0035	0.0036	0.0037

Y	46 mm	50 mm	60 mm	70 mm	90 mm	110 mm
0.3	0.0980	0.0951	0.1004	0.1024	0.1061	0.1077
0.4	0.0908	0.0889	0.0943	0.0960	0.1032	0.1048
0.5	0.0859	0.0843	0.0883	0.0900	0.0976	0.1001
0.6	0.0820	0.0804	0.0843	0.0849	0.0916	0.0948
0.7	0.0785	0.0772	0.0807	0.0813	0.0873	0.0895
0.8	0.0763	0.0749	0.0775	0.0784	0.0829	0.0852
0.9	0.0748	0.0724	0.0747	0.0761	0.0799	0.0820
1.0	0.0731	0.0711	0.0732	0.0743	0.0776	0.0792
1.2	0.0703	0.0685	0.0703	0.0712	0.0743	0.0757
1.4	0.0673	0.0653	0.0676	0.0691	0.0717	0.0732
1.6	0.0641	0.0621	0.0652	0.0672	0.0697	0.0711
1.8	0.0600	0.0585	0.0625	0.0647	0.0681	0.0696
2.0	0.0551	0.0544	0.0599	0.0629	0.0664	0.0679
2.2	0.0495	0.0504	0.0567	0.0608	0.0651	0.0665
2.4	0.0399	0.0425	0.0523	0.0569	0.0627	0.0645
2.6	0.0329	0.0356	0.0475	0.0528	0.0604	0.0627
3.6	0.0094	0.0106	0.0172	0.0260	0.0440	0.0513
4.6	0.0052					
5.6	0.0039					

TABLE A.3(f): TURBULENCE INTENSITY PROFILES FOR 4-GRIT CASE

y	22 mm	24 mm	26 mm	28 mm	31 mm	40 mm
0.3	0.0951	0.1013	0.1036	0.1031	0.0983	0.0961
0.4	0.0917	0.0999	0.1011	0.1013	0.0953	0.0920
0.5	0.0879	0.0953	0.0964	0.0976	0.0915	0.0879
0.6	0.0845	0.0904	0.0923	0.0937	0.0884	0.0845
0.7	0.0829	0.0877	0.0893	0.0909	0.0863	0.0821
0.8	0.0812	0.0847	0.0876	0.0895	0.0851	0.0807
0.9	0.0809	0.0832	0.0860	0.0876	0.0845	0.0793
1.0	0.0815	0.0828	0.0856	0.0869	0.0835	0.0789
1.2	0.0861	0.0851	0.0864	0.0869	0.0833	0.0789
1.4	0.0953	0.0901	0.0897	0.0887	0.0845	0.0801
1.6	0.1056	0.0979	0.0947	0.0921	0.0861	0.0801
1.8	0.1153	0.1060	0.1011	0.0957	0.0885	0.0807
2.0	0.1245	0.1133	0.1068	0.1012	0.0915	0.0808
2.2	0.1313	0.1208	0.1132	0.1065	0.0960	0.0820
2.4	0.1328	0.1255	0.1183	0.1112	0.1003	0.0836
2.6	0.1273	0.1261	0.1205	0.1148	0.1032	0.0853
2.8	0.1156	0.1216	0.1196	0.1161		
3.0	0.1015	0.1132	0.1149	0.1145		
3.2	0.0807	0.0984	0.1044	0.1084		
3.4	0.0616	0.0793	0.0895	0.0983		
3.6	0.0459	0.0629	0.0729	0.0843	0.0868	0.0859
4.6	0.0147	0.0184	0.0221	0.0269	0.0324	0.0536
5.6	0.0069	0.0081	0.0093	0.0109	0.0124	0.0195
6.6					0.0064	0.0092

TABLE A.3(f): (cont'd)

y	50 mm	60 mm	70 mm	90 mm	110 mm
0.3	0.0956	0.0960	0.1004	0.1045	0.1067
0.4	0.0908	0.0893	0.0945	0.1012	0.1048
0.5	0.0853	0.0835	0.0868	0.0943	0.0996
0.6	0.0805	0.0787	0.0813	0.0877	0.0925
0.7	0.0775	0.0749	0.0771	0.0832	0.0868
0.8	0.0751	0.0727	0.0732	0.0777	0.0821
0.9	0.0743	0.0707	0.0712	0.0744	0.0781
1.0	0.0736	0.0703	0.0691	0.0715	0.0751
1.2	0.0732	0.0683	0.0659	0.0667	0.0704
1.4	0.0741	0.0687	0.0640	0.0625	0.0661
1.6	0.0747	0.0691	0.0639	0.0603	0.0631
1.8	0.0755	0.0709	0.0649	0.0593	0.0597
2.0	0.0765	0.0719	0.0672	0.0591	0.0581
2.2	0.0765	0.0723	0.0673	0.0589	0.0575
2.4	0.0769	0.0721	0.0675	0.0587	0.0568
2.6	0.0771	0.0724	0.0683	0.0591	0.0556
3.6	0.0767	0.0708	0.0667	0.0587	0.0540
4.6	0.0615	0.0603	0.0584	0.0539	0.0509
5.6	0.0291	0.0356	0.0397	0.0428	0.0427
6.6	0.0124	0.0158	0.0199	0.0258	0.0295
7.6	0.0071	0.0083	0.0100	0.0139	0.0172
8.6				0.0078	0.0097

TABLE A.4: FRICTION VELOCITY VERSUS NORMALIZED DISTANCE FROM REATTACHMENT

Bare (measured)		Bare		100-Grit		80-Grit		60-Grit	
$\frac{x_s-l_B}{l_B}$	u_*	$\frac{x_s-l_B}{l_B}$	u_*	$\frac{x_s-l_B}{l_B}$	u_*	$\frac{x_s-l_B}{l_B}$	u_*	$\frac{x_s-l_B}{l_B}$	u_*
0.0000	0.2650	0.0000	0.9426	0.0000	0.9484	0.0000	0.9367	0.0000	0.9367
0.0833	0.4600	0.0833	0.9190	0.0769	0.8895	0.1111	0.9190	0.1000	0.9308
0.1667	0.6000	0.1667	0.9013	0.1538	0.8895	0.2222	0.9249	0.2000	0.9308
0.2500	0.7000	0.2500	0.8895	0.2308	0.8601	0.3333	0.9072	0.3000	0.9367
0.3333	0.7550	0.3333	0.8778	0.4231	0.8424	0.4444	0.8778	0.4000	0.9367
0.5417	0.8050	0.5417	0.8778	0.6154	0.8365	0.5556	0.8719	0.5000	0.9367
0.7500	0.8300	0.7500	0.8483	1.0000	0.8306	0.6667	0.8719	0.6000	0.9308
1.1667	0.8200	1.1667	0.8424	1.7690	0.8012	0.7778	0.8719	0.8500	0.8954
1.5833	0.8150			2.5380	0.7835	1.0556	0.8306	1.1000	0.8836
2.0000	0.8050					1.3333	0.8247	1.6000	0.8542
2.4167	0.7950					1.8889	0.8130	2.6000	0.7953
2.8333	0.7850					3.0000	0.7835	3.6000	0.7776
3.2500	0.7750					4.1111	0.7717		
3.6667	0.7650								
4.0833	0.7600								

TABLE A.5(a): NORMALIZED MEAN VELOCITY PROFILES FOR BARE CASE

x = 42 mm		x = 44 mm		x = 46 mm		x = 48 mm	
y_+	U_+	y_+	U_+	y_+	U_+	y_+	U_+
5.051	7.547	8.767	6.261	11.440	8.283	13.340	9.600
6.734	7.962	11.690	7.674	15.250	9.867	17.790	11.000
8.418	10.450	14.610	9.761	19.060	12.070	22.240	12.300
10.100	15.430	17.530	12.870	22.870	14.180	26.680	13.900
11.790	21.810	20.460	16.110	26.680	16.220	13.340	9.171
13.470	28.340	23.380	19.480	11.440	7.133	22.240	12.430
15.150	35.620	8.767	5.304	19.060	11.130	26.680	13.660
5.051	7.019	11.690	6.261	26.680	15.600	31.130	15.510
8.418	8.453	14.610	8.652	30.500	17.830	35.580	16.600
11.790	19.250	23.380	18.870	34.310	19.930	40.030	18.000
15.150	35.090	26.300	22.780	38.120	21.400	44.470	18.940
16.840	42.110	29.220	25.740	38.120	21.700	44.470	18.740
16.840	44.000	29.220	26.430	45.740	23.770	53.370	20.170
20.200	54.420	35.070	30.740	53.370	25.000	62.260	21.030
23.570	59.400	40.910	33.130	60.990	25.670	71.160	21.570
26.940	61.510	46.760	34.350	68.610	25.970	80.050	21.890
30.300	62.110	52.600	34.740	76.240	26.100	88.950	22.030
33.670	62.040	58.450	34.830	83.860	26.170	97.840	22.110
37.040	61.960	64.290	34.830	91.490	26.170	106.700	22.140
40.410	61.740	70.140	34.740	99.110	26.230	115.600	22.200
43.770	61.740	75.980	34.740	137.200	26.330	160.100	22.340
60.610	61.280	105.200	34.700				

TABLE A.5(a): (cont'd)

x = 50 mm		x = 55 mm		x = 60 mm		x = 70 mm	
y_+	U_+	y_+	U_+	y_+	U_+	y_+	U_+
14.390	11.050	15.340	11.860	15.820	11.980	16.060	11.620
19.190	12.040	15.340	11.700	15.820	11.880	16.060	11.850
14.390	10.700	20.460	12.820	21.090	12.920	21.410	12.750
19.190	11.890	25.570	14.040	26.370	14.020	26.760	13.890
23.980	13.320	30.690	14.810	31.640	14.720	32.110	14.580
28.780	14.460	35.800	15.500	36.910	15.400	37.460	15.190
33.580	15.500	40.910	16.070	42.190	15.980	42.820	15.720
38.370	16.370	46.030	16.570	47.460	16.340	48.170	16.100
43.170	17.110	51.140	16.940	52.730	16.650	53.520	16.330
47.970	17.830	51.140	16.940	52.730	16.100	53.520	15.690
47.970	17.670	61.370	17.640	63.280	16.600	64.220	16.240
57.560	18.600	71.600	18.010	73.820	16.990	74.930	16.670
67.150	19.260	81.830	18.460	84.370	17.300	85.630	16.880
76.750	19.760	92.060	18.730	94.920	17.590	96.340	17.140
86.340	20.080	102.300	18.880	105.500	17.780	107.000	17.400
95.930	20.290	112.500	19.080	116.000	17.930	117.700	17.550
105.500	20.400	122.700	19.160	126.600	18.050	128.400	17.660
115.100	20.480	133.000	19.230	137.100	18.120	139.200	17.740
124.700	20.530	184.100	19.380	189.800	18.290	192.700	18.070
172.700	20.660						

TABLE A.5(b): NORMALIZED MEAN VELOCITY PROFILES FOR 100-GRIT CASE

x = 44 mm		x = 46 mm		x = 48 mm		x = 50 mm		x = 55 mm	
y_+	U_+	y_+	U_+	y_+	U_+	y_+	U_+	y_+	U_+
5.051	9.358	8.767	9.522	11.440	10.470	12.870	11.140	14.870	10.540
6.734	13.660	11.690	11.960	15.250	12.330	17.150	12.530	19.820	11.900
8.418	19.470	14.610	14.650	19.060	14.300	21.440	13.780	24.780	13.000
10.100	25.660	17.530	17.300	22.870	16.100	25.730	15.020	29.730	13.970
11.790	32.830	20.460	19.870	26.680	17.670	30.020	16.150	34.690	14.720
13.470	38.940	23.380	22.430	30.500	19.130	34.310	17.100	39.640	15.360
15.150	44.830	26.300	24.830	34.310	20.430	38.600	17.960	44.600	15.870
16.840	50.420	29.220	26.910	38.120	21.500	42.880	18.670	49.560	16.360
20.200	56.830	35.070	29.960	45.740	23.330	51.460	19.910	59.470	17.130
23.570	60.150	40.910	31.830	53.370	24.400	60.040	20.800	69.380	17.720
26.940	61.510	46.760	32.870	60.990	25.130	68.610	21.420	79.290	18.230
30.300	61.740	52.600	33.350	68.610	25.570	77.190	21.960	89.200	18.640
33.670	61.890	58.450	33.570	76.240	25.730	85.770	22.220	99.110	19.000
37.040	61.890	75.980	33.780	83.860	25.830	94.350	22.400	109.000	19.210
40.410	61.960	105.200	33.960	91.490	25.870	102.900	22.460	118.900	19.360
43.770	62.040			99.110	25.930	111.500	22.520	128.800	19.490
60.610	62.040			137.200	26.070	154.400	22.640	178.400	19.620

x = 60 mm		x = 70 mm		x = 90 mm		x = 110 mm	
y_+	U_+	y_+	U_+	y_+	U_+	y_+	U_+
15.530	10.130	15.820	9.904	15.270	9.561	14.930	8.373
20.710	11.610	21.090	11.250	20.360	10.930	19.910	10.310
25.890	12.710	26.370	12.310	25.450	12.080	24.890	11.720
31.070	13.640	31.640	13.280	30.540	12.910	29.870	12.690
36.250	14.360	36.910	13.900	35.630	13.800	34.840	13.380
41.420	14.870	42.190	14.410	40.720	14.280	39.820	14.010
46.600	15.340	47.460	14.870	45.810	14.730	44.800	14.470
51.780	15.730	52.730	15.200	50.900	15.100	49.780	14.860
62.130	16.370	63.280	15.830	61.080	15.730	59.730	15.490
72.490	16.810	73.820	16.310	71.260	16.250	69.690	16.060
82.850	17.280	84.370	16.700	81.440	16.630	79.640	16.460
93.200	17.670	94.920	17.060	91.620	17.050	89.600	16.900
103.600	17.990	105.500	17.350	101.800	17.420	99.560	17.260
113.900	18.210	116.000	17.610	112.000	17.720	109.500	17.640
124.300	18.430	126.600	17.830	122.200	17.970	119.500	17.950
134.600	18.600	137.100	18.020	132.300	18.170	129.400	18.200
186.400	18.850	189.800	18.510	183.200	18.970	179.200	19.220

TABLE A.5(c): NORMALIZED MEAN VELOCITY PROFILES FOR 80-GRIT CASE

x = 36 mm		x = 38 mm		x = 40 mm		x = 42 mm		x = 44 mm	
y_+	U_+	y_+	U_+	y_+	U_+	y_+	U_+	y_+	U_+
5.028	13.660	9.583	9.228	12.620	9.233	14.420	8.079	14.900	9.172
6.705	19.470	12.780	12.400	16.820	11.340	19.230	10.000	19.860	10.880
8.381	25.130	15.970	14.890	21.030	13.110	24.040	11.550	24.830	12.050
10.060	31.250	19.170	17.110	25.240	15.070	28.840	12.870	29.790	13.070
11.730	37.210	22.360	20.000	29.440	16.720	33.650	14.370	34.760	14.470
13.410	43.020	25.550	22.340	33.650	18.410	38.460	15.610	39.720	15.160
15.090	48.450	28.750	24.670	37.860	19.700	43.260	16.740	44.690	16.000
16.760	52.530	31.940	26.610	42.060	20.750	48.070	17.630	49.650	16.710
20.110	57.580	38.330	29.110	50.470	22.350	57.690	19.000	59.580	17.760
23.470	59.700	44.720	30.460	58.890	23.160	67.300	19.760	69.510	18.450
26.820	60.600	51.110	31.090	67.300	23.760	76.910	20.340	79.440	18.960
30.170	61.060	57.500	31.520	75.710	24.120	86.530	20.710	89.370	19.360
33.520	61.210	63.880	31.680	84.120	24.000	96.140	20.950	99.300	19.590
36.880	61.210	70.270	31.680	92.540	24.150	105.800	21.050	109.200	19.690
40.230	61.130	76.660	31.760	100.900	24.240	115.400	21.130	119.200	19.800
43.580	61.130	83.050	31.760	109.400	24.300	125.000	21.180	129.100	19.820
60.340	61.130	115.000	31.800	151.400	24.390	173.100	21.260	178.700	19.870

x = 46 mm		x = 48 mm		x = 50 mm		x = 55 mm	
y_+	U_+	y_+	U_+	y_+	U_+	y_+	U_+
15.370	8.864	15.560	9.732	15.750	9.711	15.760	9.680
20.490	10.520	20.750	11.390	21.000	11.370	21.010	11.120
25.620	11.850	25.930	12.490	26.250	12.460	26.270	12.110
30.740	12.890	31.120	13.290	31.500	13.330	31.520	12.810
35.860	13.780	36.310	13.950	36.750	14.020	36.780	13.360
40.990	14.590	41.490	14.830	42.000	14.700	42.030	13.970
46.110	15.360	46.680	15.440	47.250	15.300	47.280	14.420
51.230	16.020	51.870	16.000	52.500	15.810	52.540	14.900
61.480	17.040	62.240	16.850	63.000	16.630	63.040	15.650
71.730	17.780	72.610	17.510	73.500	17.300	73.550	16.210
81.970	18.270	82.990	18.000	84.000	17.780	84.060	16.690
92.220	18.670	93.360	18.410	94.500	18.220	94.570	17.140
102.500	18.940	103.700	18.710	105.000	18.510	105.100	17.510
112.700	19.110	114.100	18.880	115.500	18.750	115.600	17.770
123.000	19.210	124.500	19.000	126.000	18.820	126.100	17.960
133.200	19.260	134.900	19.070	136.500	18.920	136.600	18.080
184.400	19.330	186.700	19.170	189.000	19.040	189.100	18.280

TABLE A.5(c): (cont'd)

x = 60 mm		x = 70 mm		x = 90 mm		x = 110 mm	
y_+	U_+	y_+	U_+	y_+	U_+	y_+	U_+
15.650	9.628	15.430	9.766	14.870	9.521	14.640	10.060
20.870	12.220	20.570	11.460	19.820	11.230	19.520	11.350
26.080	12.970	25.710	12.500	24.780	12.410	24.410	12.440
31.300	13.530	30.850	13.650	29.730	13.170	29.290	13.220
36.510	14.020	36.000	14.170	34.690	13.760	34.170	13.790
41.730	14.450	41.140	14.590	39.650	14.240	39.050	14.230
46.950	14.840	46.280	14.960	44.600	14.630	43.930	14.590
52.160	15.180	51.420	15.250	49.560	14.980	48.810	14.950
62.600	15.760	61.710	15.770	59.470	15.570	58.570	15.500
73.030	16.300	71.990	16.260	69.380	16.080	68.340	15.990
83.460	16.760	82.280	16.700	79.290	16.520	78.100	16.410
93.890	17.190	92.560	17.150	89.200	16.920	87.860	16.870
104.300	17.560	102.800	17.490	99.110	17.310	97.620	17.210
114.800	17.820	113.100	17.810	109.000	17.690	107.400	17.600
125.200	18.020	123.400	18.110	118.900	18.020	117.100	17.910
135.600	18.160	133.700	18.300	128.800	18.330	126.900	18.250
187.800	18.430	185.100	18.790	178.400	19.300	175.700	19.460

TABLE A.5(d): NORMALIZED MEAN VELOCITY PROFILES FOR 60-GRIT CASE

x = 38 mm		x = 40 mm		x = 42 mm		x = 44 mm	
y_+	U_+	y_+	U_+	y_+	U_+	y_+	U_+
4.969	15.020	9.188	10.160	12.000	8.563	13.880	7.811
6.625	22.490	12.250	13.350	16.000	11.280	18.500	10.220
8.281	31.620	15.310	18.080	20.000	14.310	23.130	12.540
9.938	40.450	18.380	22.330	24.000	16.750	27.750	14.730
11.590	47.770	21.440	26.040	28.000	19.750	32.380	16.840
13.250	53.130	24.500	28.530	32.000	21.590	37.000	18.410
14.910	56.530	27.560	30.450	36.000	23.090	41.630	19.760
16.560	58.420	30.630	31.430	40.000	23.910	46.250	20.540
19.880	59.770	36.750	32.120	48.000	24.560	55.500	21.220
23.190	60.080	42.880	32.330	56.000	24.720	64.750	21.410
26.500	60.150	55.130	32.370	72.000	24.780	74.000	21.460
29.810	60.150	67.380	32.410	88.000	24.780	83.250	21.460
36.440	60.230	79.630	32.410	104.000	24.780	101.800	21.460
43.060	60.300	110.300	32.490	144.000	24.810	120.300	21.460
59.620	60.300					166.500	21.490

x = 46 mm		x = 48 mm		x = 50 mm		x = 55 mm	
y_+	U_+	y_+	U_+	y_+	U_+	y_+	U_+
14.530	8.361	15.000	7.775	15.190	7.802	15.840	7.929
19.380	10.300	20.000	9.750	20.250	9.975	21.130	9.751
24.220	12.260	25.000	11.450	25.310	11.600	26.410	10.980
29.060	14.140	30.000	13.250	30.380	13.160	31.690	12.240
33.910	15.900	35.000	14.850	35.440	14.490	36.970	13.250
38.750	17.470	40.000	16.200	40.500	15.850	42.250	14.340
43.590	18.660	45.000	17.470	45.560	17.010	47.530	15.290
48.440	19.460	50.000	18.400	50.630	17.830	52.810	16.050
58.130	20.260	60.000	19.450	60.750	18.860	63.380	17.070
67.810	20.490	70.000	19.820	70.880	19.460	73.940	17.680
77.500	20.570	80.000	19.950	81.000	19.600	84.500	17.940
87.190	20.570	90.000	19.970	91.130	19.650	95.060	18.060
96.880	20.570	100.000	20.000	101.300	19.680	105.600	18.110
106.600	20.570	110.000	20.020	111.400	19.680	116.200	18.130
116.300	20.570	120.000	20.020	121.500	19.680	126.800	18.130
125.900	20.570	130.000	20.020	131.600	19.680	137.300	18.150
174.400	20.570	180.000	20.050	182.300	19.700	190.100	18.150

TABLE A.5(d): (cont'd)

x = 60 mm		x = 70 mm		x = 90 mm		x = 110 mm	
y_+	U_+	y_+	U_+	y_+	U_+	y_+	U_+
16.570	8.103	16.020	9.717	14.910	10.260	14.580	10.570
22.090	9.597	21.360	11.100	19.880	11.620	19.440	11.990
27.610	10.640	26.690	11.920	24.850	12.420	24.300	12.680
33.140	11.570	32.030	12.600	29.820	13.180	29.160	13.370
38.660	12.470	37.370	13.180	34.790	13.680	34.020	13.860
44.180	13.220	42.710	13.670	39.760	14.130	38.880	14.220
49.700	14.010	48.050	14.240	44.740	14.510	43.740	14.580
55.220	14.690	53.390	14.660	49.710	14.860	48.600	14.920
66.270	15.710	64.070	15.500	59.650	15.420	58.320	15.460
77.310	16.480	74.740	16.230	69.590	15.990	68.040	16.000
88.360	16.890	85.420	16.790	79.530	16.520	77.760	16.440
99.400	17.110	96.100	17.190	89.470	16.970	87.480	16.800
110.400	17.220	106.800	17.490	99.410	17.430	97.200	17.230
121.500	17.290	117.500	17.650	109.400	17.780	106.900	17.620
132.500	17.320	128.100	17.790	119.300	18.160	116.600	17.980
143.600	17.340	138.800	17.890	129.200	18.480	126.400	18.290
198.800	17.360	192.200	17.980	178.900	19.260	175.000	19.500

TABLE A.5(e): NORMALIZED MEAN VELOCITY PROFILES FOR 40-GRIT CASE

x = 22 mm		x = 24 mm		x = 26 mm		x = 28 mm		x = 30 mm	
y_+	U_+	y_+	U_+	y_+	U_+	y_+	U_+	y_+	U_+
18.220	10.370	18.110	9.871	17.660	9.777	17.440	9.946	16.990	10.700
24.290	11.830	24.140	11.380	23.550	11.370	23.250	11.230	22.650	11.860
30.370	12.580	30.180	12.130	29.440	12.180	29.060	12.030	28.320	12.490
36.440	13.250	36.220	12.810	35.320	12.850	34.880	12.750	33.980	13.040
42.510	13.830	42.250	13.480	41.210	13.410	40.690	13.250	39.640	13.630
48.590	14.390	48.290	14.000	47.100	13.920	46.500	13.750	45.310	14.090
54.660	14.960	54.320	14.540	52.990	14.440	52.310	14.210	50.970	14.520
60.730	15.480	60.360	15.090	58.870	14.930	58.130	14.650	56.640	14.940
72.880	16.290	72.430	16.010	70.650	15.880	69.750	15.650	67.960	15.720
85.030	16.810	84.500	16.680	82.420	16.650	81.380	16.450	79.290	16.480
97.170	17.200	96.580	17.230	94.200	17.280	93.000	17.150	90.620	17.040
109.300	17.450	108.600	17.540	106.000	17.640	104.600	17.670	101.900	17.560
121.500	17.540	120.700	17.690	117.700	17.940	116.300	18.000	113.300	17.890
133.600	17.560	132.800	17.730	129.500	18.050	127.900	18.150	124.600	18.090
145.800	17.540	144.900	17.730	141.300	18.090	139.500	18.220	135.900	18.180
157.900	17.500	156.900	17.710	153.100	18.090	151.100	18.240	147.300	18.230
218.600	17.350	217.300	17.580	211.900	18.030	209.300	18.220	203.900	18.230
								260.500	18.180
								317.200	18.140

TABLE A.5(e): (cont'd)

x = 36 mm		x = 40 mm		x = 46 mm		x = 50 mm	
y_+	U_+	y_+	U_+	y_+	U_+	y_+	U_+
16.430	10.850	15.980	10.450	15.650	10.500	15.200	10.630
21.910	11.890	21.310	11.780	20.870	11.910	20.270	11.860
27.390	12.470	26.640	12.420	26.080	12.540	25.340	12.630
32.870	13.050	31.970	12.990	31.300	13.100	30.410	13.130
38.340	13.490	37.300	13.530	36.510	13.600	35.470	13.600
43.820	13.950	42.630	13.910	41.730	13.990	40.540	13.980
49.300	14.340	47.950	14.340	46.950	14.360	45.610	14.380
54.780	14.730	53.280	14.700	52.160	14.700	50.680	14.700
65.730	15.500	63.940	15.380	62.600	15.330	60.810	15.300
76.690	16.190	74.600	16.120	73.030	15.980	70.950	15.930
87.640	16.810	85.250	16.710	83.460	16.540	81.080	16.500
98.600	17.370	95.910	17.310	93.890	17.150	91.220	17.050
109.600	17.810	106.600	17.850	104.300	17.650	101.400	17.570
120.500	18.180	117.200	18.300	114.800	18.120	111.500	18.000
131.500	18.380	127.900	18.640	125.200	18.580	121.600	18.470
142.400	18.520	138.500	18.830	135.600	18.890	131.800	18.800
197.200	18.610	191.800	19.090	187.800	19.430	182.400	19.470
252.000	18.590	245.100	19.060	240.000	19.400		
306.700	18.570	298.400	19.040	292.100	19.380		

TABLE A.5(e): (cont'd)

x = 60 mm		x = 70 mm		x = 90 mm		x = 110 mm	
y_+	U_+	y_+	U_+	y_+	U_+	y_+	U_+
14.760	10.130	14.420	10.610	13.970	9.859	13.750	9.826
19.670	11.730	19.230	12.050	18.630	11.540	18.330	11.570
24.590	12.600	24.030	12.840	23.290	12.440	22.920	12.500
29.510	13.120	28.840	13.370	27.950	13.150	27.500	13.140
34.430	13.580	33.650	13.790	32.600	13.610	32.080	13.690
39.350	14.020	38.450	14.210	37.260	14.100	36.670	14.160
44.270	14.380	43.260	14.550	41.920	14.420	41.250	14.490
49.180	14.690	48.060	14.840	46.580	14.720	45.830	14.790
59.020	15.300	57.680	15.420	55.890	15.240	55.000	15.350
68.860	15.870	67.290	15.920	65.210	15.780	64.160	15.790
78.690	16.380	76.900	16.400	74.520	16.210	73.330	16.230
88.530	16.900	86.520	16.870	83.840	16.650	82.500	16.620
98.370	17.360	96.130	17.320	93.160	17.060	91.660	17.000
108.200	17.770	105.700	17.710	102.500	17.460	100.800	17.360
118.000	18.240	115.400	18.210	111.800	17.840	110.000	17.750
127.900	18.650	125.000	18.610	121.100	18.220	119.200	18.110
177.100	19.830	173.000	20.080	167.700	19.910	165.000	19.740

TABLE A.5(f): NORMALIZED MEAN VELOCITY PROFILES FOR 4-GRIT CASE

x = 22 mm		x = 24 mm		x = 26 mm		x = 28 mm	
y_+	U_+	y_+	U_+	y_+	U_+	y_+	U_+
12.540	11.600	12.210	11.820	12.210	12.960	12.210	13.210
16.730	12.950	16.280	13.490	16.280	14.720	16.280	15.030
20.910	13.460	20.350	14.350	20.350	15.490	20.350	15.900
25.090	13.610	24.420	14.720	24.420	15.740	24.420	16.270
29.270	13.670	28.490	14.910	28.490	15.930	28.490	16.540
33.450	13.370	32.560	14.690	32.560	15.620	32.560	16.330
37.630	13.190	36.630	14.440	36.630	15.490	36.630	16.170
41.820	13.010	40.700	14.290	40.700	15.280	40.700	15.990
50.180	12.950	48.840	14.140	48.840	15.060	48.840	15.800
58.540	13.250	56.980	14.230	56.980	15.090	56.980	15.770
66.900	13.850	65.130	14.510	65.130	15.190	65.130	15.800
75.270	14.690	73.270	15.000	73.270	15.520	73.270	15.900
83.630	15.740	81.410	15.740	81.410	15.960	81.410	16.170
91.990	17.210	89.550	16.940	89.550	16.910	89.550	16.910
100.400	18.810	97.690	18.300	97.690	18.090	97.690	17.900
108.700	20.460	105.800	19.750	105.800	19.230	105.800	18.830
117.100	21.930	114.000	21.110	114.000	20.430	114.000	19.850
125.400	23.100	122.100	22.350	122.100	21.570	122.100	20.860
133.800	24.160	130.300	23.640	130.300	22.870	130.300	22.130
142.200	24.880	138.400	24.660	138.400	23.950	138.400	23.240
150.500	25.300	146.500	25.340	146.500	24.780	146.500	24.170
192.400	25.570	187.200	26.230	187.200	26.170	187.200	25.900
234.200	25.420	227.900	26.080	227.900	26.110	227.900	26.020

TABLE A.5(f): (cont'd)

x = 30 mm		x = 40 mm		x = 50 mm		x = 60 mm	
y_+	U_+	y_+	U_+	y_+	U_+	y_+	U_+
11.990	13.990	12.540	13.520	13.540	12.580	14.100	12.830
15.980	15.590	16.730	15.350	18.060	14.470	18.800	14.270
19.980	16.350	20.910	16.400	22.570	15.470	23.500	15.130
23.980	16.630	25.090	16.940	27.090	16.140	28.200	15.640
27.970	16.820	29.270	17.250	31.600	16.500	32.900	16.070
31.970	16.720	33.450	17.490	36.120	16.780	37.600	16.330
35.970	16.570	37.630	17.490	40.630	16.860	42.300	16.490
39.960	16.350	41.820	17.400	45.140	16.950	47.000	16.570
47.950	16.220	50.180	17.210	54.170	17.090	56.400	16.840
55.950	16.160	58.540	17.250	63.200	17.200	65.800	17.030
63.940	16.100	66.900	17.180	72.230	17.140	75.200	17.080
71.930	16.130	75.270	17.060	81.260	17.060	84.600	17.030
79.920	16.220	83.630	16.940	90.290	16.950	93.990	17.000
87.920	16.760	91.990	16.970	99.320	17.030	103.400	17.050
95.910	17.510	100.400	17.370	108.300	17.200	112.800	17.190
103.900	18.200	108.700	17.760	117.400	17.310	122.200	17.270
143.900	22.790	150.500	20.220	162.500	18.590	169.200	18.120
183.800	25.210	192.400	22.890	207.700	20.450	216.200	19.410
223.800	25.430	234.200	23.820	252.800	21.650	263.200	20.500
263.800	25.370	276.000	23.850	298.000	21.900	310.200	20.930
				343.100	21.900	357.200	20.960

TABLE A.5(f): (cont'd)

x = 70 mm		x = 90 mm		x = 110 mm	
y_+	U_+	y_+	U_+	y_+	U_+
14.430	11.200	14.650	10.490	14.540	9.874
19.240	13.350	19.540	12.350	19.390	11.950
24.050	14.390	24.420	13.500	24.240	13.170
28.860	15.040	29.310	14.250	29.080	13.970
33.670	15.460	34.190	14.740	33.930	14.540
38.480	15.830	39.080	15.170	38.780	14.930
43.290	16.060	43.960	15.480	43.630	15.290
48.100	16.240	48.840	15.740	48.470	15.580
57.720	16.560	58.610	16.130	58.170	16.020
67.340	16.820	68.380	16.460	67.860	16.410
76.960	16.950	78.150	16.720	77.560	16.720
86.590	17.030	87.920	16.900	87.250	16.950
96.210	17.000	97.690	17.030	96.950	17.130
105.800	17.080	107.500	17.160	106.600	17.260
115.400	17.180	117.200	17.280	116.300	17.440
125.100	17.320	127.000	17.390	126.000	17.620
173.200	17.890	175.800	17.950	174.500	18.250
221.300	18.880	224.700	18.620	223.000	18.840
269.400	19.820	273.500	19.290	271.500	19.410
317.500	20.320	322.400	19.800	319.900	19.880
365.600	20.420	371.200	20.040	368.400	20.160
		420.100	20.060	416.900	20.240

TABLE A.6: REDUCED PRESSURE DISTRIBUTION

Bare		100-Grit		80-Grit		60-Grit	
x_S/l_B	$-C_P$	x_S/l_B	$-C_P$	x_S/l_B	$-C_P$	x_S/l_B	$-C_P$
0.0000	-0.02699	0.0000	-0.02932	0.0000	0.00000	0.0000	0.000000
0.0833	-0.000692	0.0769	0.001260	0.1111	0.02197	0.1000	0.008362
0.1667	0.00692	0.1538	0.01001	0.2222	0.02449	0.2000	0.01679
0.2500	0.00000	0.2308	0.00000	0.3333	0.02755	0.3000	0.02426
0.3333	0.01799	0.3077	0.01421	0.4444	0.04674	0.4000	0.04469
0.4167	0.03460	0.3846	0.03289	0.5556	0.06266	0.5000	0.06587
0.5000	0.06436	0.4615	0.05619	0.6667	0.09756	0.6000	0.1141
0.5833	0.07266	0.5385	0.06900	0.7778	0.12120	0.7000	0.1479
0.6667	0.08720	0.6154	0.07936	0.8889	0.1448	0.8000	0.1731
0.7500	0.09204	0.6923	0.09216	1.000	0.1755	0.9000	0.1949
0.8333	0.1073	0.7692	0.1118	1.111	0.2027	1.000	0.2161
0.9167	0.1308	0.8462	0.1358	1.222	0.2243	1.100	0.2270
1.000	0.1716	0.9231	0.1807	1.333	0.2351	1.200	0.2323
1.083	0.2131	1.000	0.2179	1.444	0.2407	1.300	0.2349
1.167	0.2401	1.077	0.2391	1.556	0.2448	1.400	0.2375
1.250	0.2524	1.154	0.2470	1.667	0.2484	1.500	0.2391
1.333	0.2566	1.231	0.2488	1.778	0.2507	1.600	0.2417
1.542	0.2625	1.423	0.2494	2.056	0.2559	1.850	0.2479
1.750	0.2609	1.615	0.2484	2.333	0.2599	2.100	0.2521
2.167	0.2606	2.000	0.2507	2.889	0.2662	2.600	0.2599
		2.385	0.2548	3.444	0.2726	3.100	0.2651
		2.769	0.2564	4.000	0.2767	3.600	0.2692
		3.154	0.2591	4.556	0.2793	4.100	0.2729
		3.538	0.2617	5.111	0.2813	4.600	0.2756
		3.923	0.2636				
		4.308	0.2652				
		4.692	0.2667				
		5.077	0.2677				
		5.462	0.2688				

TABLE A.7(a): DISPLACEMENT AND MOMENTUM THICKNESSES AND SHAPE FACTOR DISTRIBUTION FOR BARE CASE

x mm	Displacement Thickness ($m \times 10^4$)	Momentum Thickness ($m \times 10^4$)	Shape Factor
22	3.22	0.58	5.514
24	4.64	0.72	6.416
26	5.83	0.78	7.481
28	5.91	0.86	6.842
30	6.63	0.94	7.089
32	7.43	1.02	7.292
34	8.03	1.06	7.546
36	7.95	1.28	6.209
38	8.53	1.25	6.849
40	8.64	1.37	6.284
42	8.13	1.64	4.954
44	7.15	2.26	3.161
46	6.02	2.57	2.338
48	5.24	2.63	1.988
50	4.80	2.60	1.848
55	4.37	2.50	1.753
60	4.04	2.38	1.696
70	4.21	2.57	1.638

TABLE A.7(b): DISPLACEMENT AND MOMENTUM THICKNESSES AND SHAPE FACTOR DISTRIBUTION FOR 100-GRIT CASE

x mm	Displacement Thickness (m x 10^4)	Momentum Thickness (m x 10^4)	Shape Factor
22	4.49	0.61	7.353
24	5.60	0.75	7.446
26	6.71	0.88	7.612
28	7.27	0.99	7.377
30	7.44	1.06	7.022
32	8.03	1.17	6.878
34	8.76	1.23	7.092
36	9.23	1.30	7.115
38	9.27	1.38	6.706
40	9.44	1.46	6.462
42	8.50	1.68	5.059
44	7.03	1.97	3.566
46	6.58	2.55	2.581
48	5.67	2.60	2.178
50	5.37	2.74	1.959
55	4.95	2.86	1.734
60	4.96	3.00	1.654
70	5.20	3.26	1.596
90	5.85	3.68	1.589
110	6.35	4.00	1.586

TABLE A.7(c): DISPLACEMENT AND MOMENTUM THICKNESSES AND SHAPE FACTOR DISTRIBUTION FOR 80-GRIT CASE

x mm	Displacement Thickness ($m \times 10^4$)	Momentum Thickness ($m \times 10^4$)	Shape Factor
22	4.16	0.35	11.985
24	5.53	0.72	7.640
26	6.02	0.81	7.458
28	6.92	0.97	7.149
30	6.93	1.10	6.308
32	6.78	1.41	4.814
34	6.37	1.72	3.711
36	6.31	1.87	3.370
38	6.01	2.33	2.585
40	5.36	2.50	2.143
42	5.14	2.72	1.890
44	4.76	2.63	1.811
46	4.79	2.74	1.749
48	4.76	2.77	1.722
50	4.78	2.81	1.701
55	4.90	3.00	1.631
60	4.98	3.06	1.627
70	5.43	3.39	1.604
90	6.34	3.99	1.590
110	6.66	4.20	1.587

TABLE A.7(d): DISPLACEMENT AND MOMENTUM THICKNESSES AND SHAPE FACTOR DISTRIBUTION FOR 60-GRIT CASE

x mm	Displacement Thickness ($m \times 10^4$)	Momentum Thickness ($m \times 10^4$)	Shape Factor
22	3.04	0.54	5.639
24	3.75	0.75	5.037
26	4.60	0.77	5.968
28	4.94	0.89	5.579
30	5.35	0.89	6.020
32	5.55	0.97	5.724
34	5.15	1.13	4.540
36	5.11	1.36	3.749
38	5.16	1.33	3.889
40	4.80	1.59	3.015
42	4.44	1.75	2.541
44	4.09	1.85	2.208
46	3.95	1.87	2.114
48	4.09	2.05	1.990
50	4.08	2.10	1.947
55	3.86	2.14	1.808
60	3.82	2.26	1.694
70	4.57	2.77	1.647
90	6.25	3.91	1.600
110	6.69	4.21	1.589

TABLE A.7(e): DISPLACEMENT AND MOMENTUM THICKNESSES AND SHAPE FACTOR DISTRIBUTION FOR 40-GRIT CASE

x mm	Displacement Thickness ($m \times 10^4$)	Momentum Thickness ($m \times 10^4$)	Shape Factor
22	3.24	1.83	1.771
24	3.57	2.07	1.718
26	4.06	2.42	1.678
28	4.36	2.63	1.657
30	4.23	2.50	1.694
36	4.94	3.00	1.644
40	5.53	3.38	1.633
46	6.08	3.76	1.616
50	6.36	3.96	1.608
60	7.00	4.37	1.601
70	7.29	4.55	1.602
90	7.43	4.65	1.599
110	7.28	4.56	1.598

TABLE A.7(f): DISPLACEMENT AND MOMENTUM THICKNESSES AND SHAPE FACTOR DISTRIBUTIONS FOR 4-GRIT CASE

x mm	Displacement Thickness (m x 10^4)	Momentum Thickness (m x 10^4)	Shape Factor
22	12.74	6.46	1.971
24	13.16	6.98	1.887
26	13.01	7.26	1.791
28	12.99	7.50	1.732
31	12.72	7.56	1.682
40	11.96	7.69	1.554
50	10.91	7.32	1.490
60	10.11	6.93	1.459
70	9.93	6.77	1.468
90	9.88	6.68	1.480
110	10.16	6.79	1.496

TABLE A.8: MAXIMUM TURBULENCE INTENSITY DISTRIBUTION

All turbulence intensities given in ms^{-1}.

Bare		100-Grit		80-Grit		60-Grit	
$\frac{x_s}{l_B}$	$(\overline{u^2})^{1/2}$	$\frac{x_s}{l_B}$	$(\overline{u^2})^{1/2}$	$\frac{x_s}{l_B}$	$(\overline{u^2})^{1/2}$	$\frac{x_s}{l_B}$	$(\overline{u^2})^{1/2}$
0.1667	0.4875	0.1539	0.5325	0.2222	0.4605	0.2000	0.5910
0.2500	0.6315	0.2308	0.5790	0.3333	0.4605	0.3000	0.7140
0.3333	0.7905	0.3077	0.7875	0.4444	0.5355	0.4000	0.8835
0.4167	0.9195	0.3846	0.8925	0.5556	0.8625	0.5000	0.8880
0.5000	1.0485	0.4615	1.0140	0.6667	1.2000	0.6000	0.7320
0.5833	1.2060	0.5385	1.1025	0.7778	1.3320	0.7000	0.8205
0.6667	1.4415	0.6154	1.1835	0.8889	1.7780	0.8000	0.9345
0.7500	1.6425	0.6923	1.3380	1.0000	2.0925	0.9000	1.2000
0.8333	2.1420	0.7692	1.5840	1.1111	2.0985	1.0000	1.3245
0.9167	2.8245	0.8462	1.8225	1.2222	1.9695	1.1000	1.4475
1.0000	2.9265	0.9231	2.0730	1.3333	1.9905	1.2000	1.5285
1.0833	2.9205	1.0000	2.1555	1.4444	1.9395	1.3000	1.5720
1.1667	2.7495	1.0769	2.1045	1.5556	1.7835	1.4000	1.6140
1.2500	2.5350	1.1538	2.1360	1.6667	1.6965	1.5000	1.6425
1.3333	2.3640	1.2308	1.8540	1.7778	1.6125	1.6000	1.6785
1.5417	1.9845	1.4231	1.6335	2.0556	1.5525	1.8500	1.7100
1.7500	1.7265	1.6154	1.5705	2.3333	1.4400	2.1000	1.7325
2.1667	1.6605	2.0000	1.5765	2.8889	1.4445	2.6000	1.6260
		2.7692	1.6080	4.0000	1.4835	3.6000	1.5645
		3.5385	1.6425	5.1111	1.6020	4.6000	1.5825

TABLE A.9: TURBULENCE DATA NORMALIZED BY $\bar{U}_r^2$

Bare		100-Grit		80-Grit		60-Grit	
$\frac{x_s}{l_B}$	$\frac{\overline{u^2}}{U_r^2}$	$\frac{x_s}{l_B}$	$\frac{\overline{u^2}}{U_r^2}$	$\frac{x_s}{l_B}$	$\frac{\overline{u^2}}{U_r^2}$	$\frac{x_s}{l_B}$	$\frac{\overline{u^2}}{U_r^2}$
0.1667	0.001056	0.1538	0.001260	0.2222	0.000943	0.2000	0.001552
0.2500	0.001772	0.2308	0.001490	0.3333	0.001274	0.3000	0.002266
0.3333	0.002777	0.3077	0.002756	0.3333	0.002460	0.4000	0.003469
0.4167	0.003758	0.3846	0.003540	0.4444	0.003306	0.5000	0.003505
0.5000	0.004886	0.4615	0.004570	0.5556	0.006400	0.6000	0.002381
0.5833	0.006464	0.5385	0.005402	0.6667	0.007885	0.7000	0.002992
0.6667	0.009235	0.6154	0.006225	0.7778	0.014210	0.8000	0.003881
0.7500	0.011990	0.6923	0.007957	0.8889	0.019460	0.9000	0.006400
0.8333	0.020390	0.7692	0.011150	1.0000	0.019570	1.0000	0.007797
0.9167	0.035460	0.8462	0.014760	1.1111	0.017240	1.1000	0.009312
1.0000	0.038060	0.9231	0.019100	1.2222	0.017610	1.2000	0.010380
1.0833	0.037910	1.0000	0.020650	1.3333	0.016720	1.3000	0.010980
1.1667	0.033600	1.0769	0.019680	1.4444	0.014140	1.4000	0.011580
1.2500	0.028560	1.1538	0.020280	1.5556	0.012790	1.5000	0.011990
1.3333	0.024840	1.2308	0.015280	1.6667	0.011560	1.6000	0.012520
1.5417	0.017500	1.4231	0.011860	1.7778	0.010710	1.8500	0.013000
1.7500	0.013250	1.6154	0.010960	2.0556	0.009216	2.1000	0.013340
2.1667	0.012250	2.0000	0.011050	2.3333	0.009274	2.6000	0.011750
		2.7692	0.011490	2.8889	0.009781	3.6000	0.010880
		3.5385	0.011990	4.0000	0.010750	4.6000	0.011130
				5.1111	0.011410		

Castro & Haque

$\frac{x_s}{l_B}$	$\frac{\overline{u^2}}{U_r^{\,2}}$
0.1290	0.053300
0.2310	0.058800
0.3530	0.088600
0.4550	0.093300
0.5730	0.093300
0.6750	0.091800
0.7880	0.085100
0.8980	0.072900
0.9610	0.063100
1.0120	0.056500
1.1250	0.045900
1.2390	0.040400
1.3490	0.040000

TABLE A.10: SKIN FRICTION COEFFICIENT DISTRIBUTION

(Skin friction coefficient multiplied by 1000.)

Present Study		Bradshaw & Wong		Chandrsuda & Bradshaw	
X^*	C_f	X^*	C_f	X^*	C_f
0.000	0.624	0.119	0.500	0.017	0.083
0.083	1.881	0.167	0.735	0.525	1.976
0.167	3.200	0.238	1.132	1.024	2.321
0.250	4.356	0.286	1.515	1.532	2.345
0.333	5.067	0.310	1.662		
0.542	5.760	0.381	1.838		
0.750	6.124	0.429	1.941		
1.167	5.977	0.476	2.059		
1.583	5.904	0.548	2.265		
2.000	5.760	0.595	2.353		
2.417	5.618	1.059	2.882		
2.833	5.478	1.157	2.882		
3.250	5.339	1.206	2.926		
3.667	5.202	1.255	2.971		
4.083	5.134	1.304	3.000		
		1.451	3.000		
		1.549	3.015		
		1.598	3.000		
		1.696	3.044		
		2.579	3.015		
		3.093	3.044		
		3.583	3.000		
		4.098	3.000		